ENERGY SPECTRUM MEASURED BY THE TELESCOPE ARRAY SURFACE DETECTOR

BY DMITRI IVANOV

A dissertation submitted to the
Graduate School—New Brunswick
Rutgers, The State University of New Jersey
in partial fulfillment of the requirements
for the degree of
Doctor of Philosophy
Graduate Program in Physics and Astronomy
Written under the direction of
Professor Amitabh Lath
and approved by

New Brunswick, New Jersey
October, 2012

© 2012

Dmitri Ivanov

ALL RIGHTS RESERVED

ABSTRACT OF THE DISSERTATION

Energy Spectrum Measured by the Telescope Array Surface Detector

by Dmitri Ivanov

Dissertation Director: Professor Amitabh Lath

Two conflicting measurements of the ultra high energy cosmic ray (UHECR) flux have been reported by the Akeno Giant Air Shower Array (AGASA) and the High Resolution Fly's Eye (HiRes) experiments. HiRes observes a $\sim 5\sigma$ suppression at $E = 10^{19.75}$ eV, which is in agreement with the prediction of Greisen-Zatsepin-Kuz'min (GZK) theory. AGASA, in contrast, sees the flux extended well beyond $E = 10^{20}$ eV with no visible break, suggesting that the flux is limited only by the rate at which the sources can produce the UHECR and not by interaction of energetic particles with the cosmic microwave background, thus challenging the relativistic invariance principle. In response to this discrepancy, a new experiment named the Telescope Array (TA) has been deployed, which combines the detection elements used separately by HiRes and AGASA.

We describe the TA surface detector (SD) analysis using a technique new to the field, which consists of a detailed Monte-Carlo (MC) simulation of the SD response to the natural cosmic rays, validating the MC by comparing its distributions with the data, and calculation of the SD aperture from the MC.

We will also describe our reconstruction procedure, based solely upon the data, and its application to both data and the MC. Finally, we will describe the energy spectrum resulting from this analysis, which is found to be in excellent agreement with the HiRes result, and as such, is the first confirmation of the GZK effect by a ground array of scintillation counters.

Preface

Since the early the 20^{th} century, astrophysical observations constitute an important experimental arena for shaping modern theories of space-time, matter, and interactions. Ranging from the studies of the stellar evolution, which require a delicate interplay among fields such as classical electromagnetism, quantum mechanics, and Newtonian gravity, to the studies of large scale behavior of the universe, which have lead to a break through in understanding of the space-time geometry, the astrophysics field has always remained dynamic and rich of undiscovered and unexplained phenomena. This remains true in the 21^{st} century.

The discovery of cosmic rays with energies exceeding 10^{18} eV in the 1960s, referred to as the *ultra high energy cosmic rays*, resulted in one of the most profound theoretical and experimental challenges of the century. The sources of the observed primary particles are yet to be discovered, and to date, no satisfactory theoretical models exist which explain their origin and acceleration. At the same time, certain models of ultra high energy cosmic ray propagation through the intergalactic medium are finding long awaited experimental support, and over the past decade, the cosmic ray field has been gaining momentum as new large and accurate experiments begin to report their results.

This dissertation is an experimental contribution to the cosmic ray field resulting from the measurements provided by the Telescope Array Experiment. The paper will focus on the detection of cosmic rays in $E > 10^{18}$eV energy range by the Telescope Array surface detector. The details of the detector, measurements, and their implications will be described.

Chapter 1 is an introduction to the cosmic ray field, with a strong emphasis on the ultra high energy domain ($E > 10^{18}$ eV). Presently known theory and commonly used techniques of measuring the extensive air-showers induced by the ultra high energy cosmic rays in the atmosphere will be discussed.

Chapter 2 is a description of the Telescope Array (TA) experiment. While giving a general overview of all TA detectors types and their stand-alone performances, the main focus of the chapter is the TA surface detection (SD) because its measurements are used for calculating physics results in this paper. A brief discussion of the TA low energy extension (TALE) detector will be provided also.

Chapter 3 describes the TA SD trigger, data acquisition, data format, and calibration. Since the TA SD is expected to be collecting data for another decade, this technical note is intended to serve as a reference to those who plan on engaging in similar analyses.

Chapter 4 is a description of the Monte-Carlo techniques used in determining the response of the TA SD to the cosmic rays. Comparisons of reconstructed variables between data and the MC will be shown to prove the validity of the simulation.

Chapter 5 describes the reconstruction of cosmic ray events by the TA surface detector. The discussion includes signal analysis, pattern recognition, geometry and energy determination, quality cuts (event selection), and resolution in pointing direction and energy.

Chapter 6 describes the result of the measurement. Energy spectrum and its calculation based on the aperture derived from the Monte-Carlo will be described in detail, and relevant systematic uncertainties will be evaluated.

Chapter 7 is the conclusion of this analysis. The result in Chapter 6 will be compared to other experiments and its physical implications will be discussed.

Chapter 8 is the appendix that lists common acronyms used in the field.

Acknowledgements

I would like to thank the following individuals and organizations:

- My graduate advisor, Prof. Gordon Thomson, for an excellent guidance and help with organizing the analysis, which lead to this work. Also, the chairman of my graduate committee, Prof. Amitabh Lath, for undertaking this task on a short notice.
- My family, for their support.
- Profs. Douglas Bergman and Charles Jui, for good over-lunch discussions, which contributed to my understanding of the analysis and physics involved in this work.
- Prof. John Matthews, for helping me with organizing work at the University of Utah over the past ~ 3 years spent in Salt Lake City.
- Dr. Benjamin Stokes, for his contribution to the simulation and understanding of the detector.
- Profs. Ronald Ransome and Theodore Williams, for ensuring that I meet all graduate school requirements.
- S. Stratton, for helping me to schedule the time and place of my defense and getting my candidacy papers from Rutgers. This would have been difficult to do from Utah.
- Nancy DeHaan, Heidi Frank, Shirley Hinds, Frank Misak, Vicki Nielsen, and Helen Posluszny, for helping me in dealing with lots of paperwork at

Rutgers and the University of Utah.

- Members of my graduate committee: Profs. John Paul Chou, Eric Gawiser, Amitabh Lath, Scott Thomas, and Gordon Thomson, for keeping my graduate work in check.
- Dr. John Krizmanic, for good questions and comments, which helped me to prepare for the defense.
- Members of the Telescope Array collaboration, for their invaluable suggestions and criticisms, which resulted in better understanding and improvements of the results of this work. My special thanks go to Dr. Grigory Rubtsov, for finding and promptly reporting mistakes in my analysis programs.
- My fellow graduate students at Rutgers University and the University of Utah, for good times.
- Finally, I would like to thank the agencies and universities, described in the paragraph below [1], for funding the Telescope Array construction, operations, conferences, and providing facilities for analyzing the data.

The Telescope Array experiment is supported by the Japan Society for the Promotion of Science through Grants-in-Aid for Scientific Research on Specially Promoted Research (21000002) "Extreme Phenomena in the Universe Explored by Highest Energy Cosmic Rays", and the Inter-University Research Program of the Institute for Cosmic Ray Research; by the U.S. National Science Foundation awards PHY-0307098, PHY-0601915, PHY-0703893, PHY-0758342, and PHY-0848320 (Utah) and PHY-0649681 (Rutgers); by the National Research Foundation of Korea (2006-0050031, 2007-0056005, 2007-0093860, 2010-0011378, 2010-0028071, R32-10130); by the Russian Academy of Sciences, RFBR grants 10-02-01406a and 11-02-01528a (INR), IISN project No. 4.4509.10 and Belgian

Science Policy under IUAP VI/11 (ULB). The foundations of Dr. Ezekiel R. and Edna Wattis Dumke, Willard L. Eccles and the George S. and Dolores Dore Eccles all helped with generous donations. The State of Utah supported the project through its Economic Development Board, and the University of Utah through the Office of the Vice President for Research. The experimental site became available through the cooperation of the Utah School and Institutional Trust Lands Administration (SITLA), U.S. Bureau of Land Management and the U.S. Air Force. We also wish to thank the people and the officials of Millard County, Utah, for their steadfast and warm support. We gratefully acknowledge the contributions from the technical staffs of our home institutions and the University of Utah Center for High Performance Computing (CHPC).

Dedication

To my parents and grandparents

Table of Contents

Abstract ii

Preface iv

Acknowledgements vi

Dedication ix

List of Tables xiii

List of Figures xv

1. Introduction 1

1.1. Extensive Air Showers 4

1.2. UHECR Mass Composition 11

1.3. UHECR Accelerators 17

1.4. UHECR Spectrum 19

2. The Telescope Array Detector 25

2.1. Air-Fluorescence Detector 30

2.2. Surface Detector 32

3. TA SD Data 42

3.1. Trigger and Data Acquisition 42

3.2. Raw Data Format 47

3.3. Calibration 56

3.4. Pass0 Analysis 63

3.5. DST Data Format 63

4. TA SD Monte Carlo 66

4.1. CORSIKA Simulation 68

4.2. Detector Response 72

4.3. Full Monte-Carlo 81

4.4. Validating the Monte-Carlo 84

5. TA SD Event Reconstruction 91

5.1. Signal Selection and Pattern Recognition 92

5.2. Geometry Definitions and Starting Values 94

5.3. Time Fit 98

5.4. Lateral Distribution Fit 100

5.5. First Energy Estimation 100

5.6. Energy Scale 101

5.7. Quality Cuts and Resolution 103

5.8. Analysis Structure 110

6. TA SD Energy Spectrum 115

6.1. Measurement Procedures 116

6.2. Measured Flux 122

6.3. Systematic Uncertainties of the Flux 126

6.4. Final Result 131

7. Conclusions 133

7.1. Comparison with Other Experiments 133

7.2. Astrophysical Interpretation 140

8. Appendix 145

8.1. Acronyms 145

Bibliography 148

List of Tables

3.1. Description of the GPS time stamp 48

3.2. Description of the event header 49

3.3. Description of the waveform header 51

3.4. Description of the waveform data header 51

3.5. Description of the waveform data, part 1. 52

3.6. Description of the waveform data, part 2. 53

3.7. Monitoring data format 55

3.8. Description of the monitoring histograms. 56

3.9. Description of the additional monitoring data. 57

3.10. Summary of the rusdraw bank. 65

4.1. Summary of the rusdmc bank. 83

4.2. Cosmic ray parameters generated in the TA SD Monte-Carlo. . . 84

5.1. Efficiency of the quality cuts 108

5.2. Summary of the rufptn bank. 112

5.3. Summary of the rusdgeom bank. 113

5.4. Summary of the rufldf bank. 114

6.1. Results of fitting the TA SD spectrum to a broken power law function (Equation 6.12). 126

6.2. Estimation of the systematic uncertainty of the flux due to the $\sigma_{S800}/S800$ cut. Cuts on $\sigma_{S800}/S800$ are changed from their base value of 0.25 to induce a ∼68% change in the numbers of accepted events in the two energy bins. The results are then estimated using Equation 6.19. 131

6.3. Cosmic ray flux measured by the TA surface detector. For each bin in $\log_{10}E$, the following quantities are tabulated: $\log_{10}(E/\text{eV})$ is the energy of the bin center, b is the bin size, N is the number of events, J is the flux in [$\text{eV}^{-1}\,\text{s}^{-1}\,\text{m}^{-2}\,\text{sr}^{-1}$], $\sigma^{\text{STAT}}_{\text{LOWER}}$ and $\sigma^{\text{STAT}}_{\text{UPPER}}$ are the statistical uncertainties on the flux that correspond to the lower and upper 68% confidence limits, and σ^{SYS} is the estimated systematic uncertainty of each bin. All uncertainties are in [$\text{eV}^{-1}\,\text{s}^{-1}\,\text{m}^{-2}\,\text{sr}^{-1}$]. 132

7.1. Comparison of the results of the fits to the broken power law function (Equation 6.12) among different cosmic ray experiments. Only the parameters describing the shape of the spectrum are quoted (most experiments do not officially quote the overall normalization constant K). 140

List of Figures

1.1. Air-fluorescence spectrum measured by the FLASH experiment. Bar widths have been chosen to represent the resolution of the instrument at each point (± 2nm). 7

1.2. HiRes mean x_{max} result [2]. Points with error bars are the data and lines represent the predictions of the hadronic models for the proton and iron primaries. According to this result, the UHECR primary particles consist of mostly protons above 1.6×10^{18} eV. . 12

1.3. Pierre Auger mean x_{max} result [3] (points with error bars) plotted on top of the predictions from the hadronic models (lines) for the proton and iron primaries. The Pierre Auger data suggests that the composition becomes heavy above 3×10^{18} eV. 12

1.4. Preliminary Telescope Array measurement of the mean x_{max}, adopted from [4]. Points with error bars are the data and lines show the hadronic model predictions for the proton and iron primary particles. This result shows that the UHECR mass composition is consistent with protons above 1.6×10^{18} eV. 13

1.5. Deflection angle due to the GMF for $E \simeq 4 \times 10^{19}$ eV proton adopted from [5], which uses the GMF model described in [6]. The color-coded result (in degrees) is plotted in Galactic coordinates (galactic latitude vs galactic longitude) using the Hammer-Aitoff projection. 15

1.6. Arrival map of $E > 4 \times 10^{19}$ eV events in equatorial coordinates (using Hammer-Aitoff projection) reported by three experiments in the Northern hemisphere: HiRes [7], AGASA [8], and the TA SD (preliminary, using data in May 11, 2008 to April 25, 2011 range). Additionally, stars label the locations of the center of the Milky Way galaxy (GC) and the Messier 87 (M87), a large elliptical galaxy 16.7 Mpc away [9]. 16

1.7. Hillas plot adopted from [10]. Magnetic field strength is plotted versus the size of the potential accelerator. Acronyms in the figure should be interpreted as follows: AGN - active galactic nuclei, SNR - supernova remnants, GRB - gamma ray bursts. Astrophysical objects capable of accelerating iron and proton nuclei to 10^{20} eV should lie above the dashed and solid lines, respectively. 18

1.8. Differential cosmic ray flux for E > 100 TeV reported by a variety of experiments. The flux is plotted versus the logarithm of energy. Dashed line is a least-squares fit to a single power law function of index -3. 19

1.9. Energy spectrum measured by the High Resolution Fly's Eye experiment [11], with superimposed result of the AGASA experiment [12]. The plot is adopted from [11]. 21

1.10. Contributions to the energy losses for the proton primaries propagating in the cosmic microwave background plotted versus the proton energy. Solid (1) and dotted (2) curves are results of calculations by Berezinsky *et. al.* [13] and the squares points correspond to the calculation by Stanev *et. al.* [14]. The plot is adopted from [13]. Labels "$e^+ e^-$", "pion-prod" and "red-shift" correspond to the energy losses due to the pair production, photopion production, and the expansion of the universe, respectively. 23

1.11. Fits to the energy spectrum results of (a) AGASA (with rescaled energies) and (b) HiRes, done by Berezinsky *et. al.*. The plot is adopted from [13]. See the text for more details. 24

2.1. The Telescope Array Detector 26

2.2. TA SD Trigger efficiency obtained from simulations for the cases of proton and iron. Counters in the currently operating SD array are separated by [1200 m] (triangles) and the efficiency plateaus at $\sim 10^{19}$ eV. Squares and circles correspond to the (proposed) TALE infill array which will have counters separated by 400 m and 600 m. 27

2.3. TA On-time. Total observation time for each detector is plotted versus (Gregorian) date. 28

2.4. TA Aperture. Area × solid angle × efficiency for each detector working in stand-alone mode is plotted for every 0.1 bin in logE (E is the cosmic ray energy). Effects of trigger and reconstruction of each TA detector are included. 29

2.5. Mirror and cluster box arrangements used by the Telescope Array fluorescence detectors: (a) Black Rock Mesa or Long Ridge, (b) Middle Drum. 31

2.6. TA FD fields of view. PMT altitude (above the horizon) versus azimuth (in coordinate systems of each FD) are plotted. Each PMT effectively samples a $\sim 1^\circ$ cone on the sky. 31

2.7. Exterior view of the TA surface detector unit: 1 - Wireless communication antenna, 2 - GPS receiver, 3 - Battery and electronics box, 4 - Solar panel, 5 - Iron roof, 6 - Supporting metal frame. . 33

2.8. TA SD interior configuration, top view (top) and the cross-sectional view (bottom). 1 - Stainless steel enclosure box, 2 - Scintillator (right side of, represented by the shaded area), 3 - Wavelength shifting fiber (WLS), 4 - Photomultiplier tube, 5 - Tyvek sheet, 6 - WLS (cross section), 7 - Grooves for the WLS placement, 8 - Separator plate 34

2.9. Mean energy deposition in a 1.2 cm thick scintillator by a vertical muon plotted versus muon kinetic energy, obtained from a GEANT4 simulation. The minimum ionizing energy occurs at 300 MeV. 36

2.10. Energy loss histogram of a vertical 300 MeV (minimum ionizing) muon in the 1.2 cm scintillator, obtained from a GEANT4 simulation. The MPV (most probable value) defines the VEM unit, which is 2.05 MeV for the TA SD. Dashed curve shows a fit to the Landau function. 37

2.11. Battery charging cycle of a typical SD unit plotted versus time since UTC midnight (10/24/2011). 38

2.12. TA SD Waveforms: (a) corresponds to the Level-0 and (b) to Level-1 triggers. Flat regions surrounding the pulses, called *pedestals*, are $\sim$ 5 FADC counts / time slice in these examples. 39

2.13. Calibration histograms from a typical TA SD counter collected over a 10 minute period (monitoring cycle). (a) are the 1-MIP histograms, sampled at $\sim$750 Hz for upper and lower layers in coincidence. (b) are the pedestal histograms, sampled at $\sim$6.25 MHz for each layer. 41

3.1. TA SD counters deployed on a 1200 m grid shown using the CLF coordinate system with the origin redefined at X = -14.69 km, Y = -19.73 km, and Z = 0. Additionally, the distance is measured in 1200 m units so that most (physical) counter locations are nearly on the grid, allowing one to identify the counters by the integer parts of their X and Y positions. The (integer) counter position ID is described by one number, which is ID = $X \times 100 + Y$. Filled circles represent the communication towers, location of the CLF is labeled by the star, solid line describes the edge of the array and dashed lines show the T-shape boundary, which divides the array into 3 logical sub-arrays. Counter positions are marked by open squares. 44

3.2. TA SD trigger patterns, up to rotations by $\pi/2$. Circles represent counters on a 1200 m square grid. Filled circles correspond to Level-1 trigger counters ($\geq\sim$3 MIP) occurring in the same 8 μS window. Any pair of Level-1 trigger counters is within 2 spacing units (2400 m). 45

3.3. Difference between the core time and the trigger time reported by the TA SD data acquisition system. The RMS of the distribution is $\simeq 1$ μS. Only $\sim$0.5% of events are outside of this $\pm\,10$ μS window. Events with (reconstructed) zenith angle less than 45° were used. 50

3.4. Mean gain in FADC counts per VEM, represented by color, over a typical day of data: (a) for the upper scintillator layers, (b) for the lower layers. The gain is plotted versus counter X-Y position. 58

3.5. Energy deposition by atmospheric particles simulated using CORSIKA and GEANT4 simulation of the TA SD. The results are shown as (normalized) histograms of energy depositions in the upper and lower scintillator layers. 59

3.6. Fitting 1-MIP histograms to determine the detector gains in FADC counts / MeV (and also FADC counts/VEM): (a) is the upper layer and (b) is the lower layer. Circles represent the real 1-MIP histograms and curves represent the fitted values. 61

3.7. Ratio of the 1-MIP histogram peak location (pedestal subtracted), taken from the real data, and the FADC counts per VEM, obtained from the 1-MIP simulation procedure described above. The ratio is plotted for each day over 3 years of data . Black points represent the mean value for each day over all working counters in all events and the gray-shaded area represents the RMS (for each day). The RMS is better than 1.5 %. 62

3.8. Summary of pass0 outputs which consist of two information pieces: calibrated events and (separately written) calibration and monitoring information. Separated calibration and monitoring are necessary for generating detailed Monte-Carlo simulations of the TA SD with the same characteristics (and format) as the actual data. . . 64

4.1. (a): Illustration of the problem caused by the thinning approximation in simulating the surface detector. Dotted lines represent the discarded particles (which would exist in a real shower) and the solid lines represent the weighted particles (thicker lines correspond to larger weights). The surface detector counters are represent by the filled polygons. (b): Illustration of the CORSIKA dethinning algorithm, adopted from [15]. 70

4.2. Comparisons of the energy deposition in the TA SD counters (vertical axis) at varying distances from the shower axis (horizontal axis) for a 10^{19} eV proton shower with a zenith angle of 45°: (a) 10^{-6} thinned shower compared to the same non-thinned shower (b) dethinned shower compared to the same non-thinned shower. The comparisons demonstrate that the dethinning procedure correctly reproduces both the mean and the RMS of the energy deposition, while the thinning method alone reproduces only the mean values. 72

4.3. Illustration of the detector and the beam set-up used in generating the TA SD response library by the GEANT4-based program. X, Y are the randomly chosen coordinates inside the 6m x 6m square, θ is the (given) zenith angle of the particle, and ϕ is the randomly chosen azimuthal angle. Arrow represents the direction of the simulated particle. 74

4.4. Examples of the energy deposition histograms used in preparing the TA SD response library. X-axis is the energy deposition occurring in the upper layer, Y-axis is the energy deposition in the lower layer, and the Z-axis (represented by colors) is the frequency. The examples use 1 GeV μ^+ and 1 GeV γ: (a): μ^+ at $\sec(\theta) = 1.0$, (b): μ^+ at $\sec(\theta) = 2.0$, (c): γ at $\sec(\theta) = 1.0$, (d): γ at $\sec(\theta) = 2.0$. . 77

4.5. Comparison of the energy deposition dE/dX distributions in the scintillators produced by the response library (black points) and the exact simulation program (dotted lines). The comparisons are made for two particles: (a): 5 GeV γ of $\theta = 40°$ (b): 5 GeV μ^+ of $\theta = 40°$. Large spikes at $dE/dX = 0$ (accurately reproduced by the response library) correspond to the cases where the particles miss the detector: the area of each scintillator is 1.5 m x 2.0 m, and the area of the sampling square is 6 m x 6 m. The edge and back-scattering effects (especially in the case of γ) near $dE/dX = 0$ are also reproduced correctly by the response library. 79

4.6. Response shape to a minimum ionizing particle for a typical TA SD counter. 80

4.7. Distributions of generated shower parameters in the TA SD Monte-Carlo. In (a)-(c), points represent the samples and the solid lines correspond to the theoretical distributions from which the samples were drawn. A detailed description of the plots is provided in the text and in Table 4.2. 86

4.8. Comparison of the normalized fit residuals between the data and Monte-Carlo, where the residuals Δ/σ are plotted versus the counter distance from the shower axis R. Each entry represents a counter. The results are accumulated over all events in the data and MC sets. Points with error bars are the profile plots superimposed on top of the two-dimensional histograms. The profile points and error bars correspond to the mean and the RMS in each R slice, respectively. (a): Normalized time fit residuals of the data (Equation 4.1). (b): Normalized time fit residuals of the MC. (c): Normalized lateral distribution fit residuals of the data (Equation 4.2). (d): Normalized lateral distribution fit residuals of the MC. . . . 87

4.9. Data and Monte-Carlo comparison of the variables that describe the quality of the fits that determine the shower geometry and energy. Points with error bars are the data and solid lines are the MC histograms. The Monte-Carlo histograms have been normalized to have the same integrals (area) as the data. These variables are described in detail in Chapter 5. 88

4.10. Comparison of the data and Monte-Carlo histograms of the quantities related to the reconstruction of the shower geometry. Points with error bars represent the data and the solid lines correspond to the MC. The MC histograms are normalized to the data by area. 89

4.11. Data and MC comparison of the lateral distribution quantities. Points with error bars represent the data and the solid lines are the MC histograms normalized to the same area as the data. . . 90

5.1. Examples of the (processed) counter signals. Dashed lines show the signal selection. In both plots, the left dashed lines indicate the leading edges of the pulses, which define the counter time. (a): An example of a typical signal that is a part of the shower. (b): A signal from the shower (contained within the dashed lines) that was preceded by a random muon pulse, which occurred $\sim 25\mu$ S earlier. Then the counter was silent for $\sim 25\mu$ S (no Level-0 trigger), and finally, the counter triggered again due to the signal from the shower. The random muon pulse was excluded by the signal selection algorithm. 93

5.2. Event display picture of a typical TA SD event. Circle centers correspond to the counter positions, the circle areas are proportional to the logarithms of the counter pulse heights and the circle colors represents the counter times. The star shows the position of the shower core, and the arrow is the shower axis projected onto the ground, which is labeled by $\hat{\mathbf{u}}$. 94

5.3. Schematic view of the shower front at the time T_0. The variables are described in the text. 95

5.4. Two fits for determining the SD event geometry and $S800$. (a): An illustration of the SD time fit. Counter time is plotted versus distance along the $\hat{\mathbf{u}}$-axis (points). Solid line represents the fit expectation time for counters that would lie directly on the $\hat{\mathbf{u}}$-axis, dashed and dotted lines are the fit expectation times for counters that are 1 km and 2 km off the $\hat{\mathbf{u}}$-axis, respectively. (b): Lateral distribution fit to the AGASA function. Counter pulse height is plotted versus the perpendicular (lateral) distance from the shower axis. Solid line represents the fit curve. Error bars with no points represent the silent counters (working counters which did not register any signal). 99

5.5. TA SD Energy Estimation Table 101

5.6. TA SD and TA FD energy comparison plots. Well reconstructed events seen in common by the TA SD and the 3 TA FDs (BR, LR, MD) are compared simultaneously. The TA SD CORSIKA-derived energy has been reduced by a factor of 1/1.27 before making these comparisons. (a) is the scatter plot of E_{FD} versus E_{SD}. Solid line represents the $E_{FD} = E_{SD}$ case. (b) is the logarithm of the ratio of E_{FD} and E_{SD} represented by a 1-dimensional histogram. Dashed line is a fit to a Gaussian. 102

5.7. Effect of the quality cuts (added incrementally) on the energy resolution. Two dimensional histograms of reconstructed energy (E_{REC}) versus the MC generated energy (E_{GEN}) are plotted in all cases. Box size is proportional to the logarithm of the numbers of events in each (two dimensional) bin, and the dashed line represents the $E_{REC} = E_{GEN}$ case. (a): no cuts, (b): $N_{SD} \geq 5$, (c): $\theta < 45°$, (d): $D_{\text{Border}} > 1200$ m, (e): $\chi^2/\text{dof} < 4$, (f): $\sqrt{\sigma_\theta^2 + \sin^2(\theta)\sigma_\phi^2} < 5°$, (g): $\sigma_{S800}/S800 < 0.25$. This also describes the final case, where all of the 6 cuts have been applied. 105

5.8. Reconstructed event core position after the $D_{\text{Border}} \geq 1200$ m cut: (a) for 2008/05/11 - 2008/11/10 range, (b): for 2008/05/11 - 2011/04/25 range. Solid line represents the edge of the array and the dashed line represents the T-shape boundary (applicable only for 2008/05/11- 2008/11/10 data). 106

5.9. The TA SD angular resolution evaluated using a Monte-Carlo spectral set. Cumulative histograms of the opening angle between the reconstructed and the true (MC generated) event directions are shown using three energy slices: (a) $10^{18.0}$eV $< E < 10^{18.5}$eV, (b) $10^{18.5}$eV $< E < 10^{19.0}$eV, (c) $E > 10^{19.0}$eV. X axis represents the opening angle δ and the Y axis represents the fraction f of events (in percent), reconstructing within a given opening angle with respect to their true directions. Dashed lines represents the 68% confidence limits, which are the values of δ containing 68% of all reconstructed events in the given energy ranges. 109

5.10. The TA SD energy resolution evaluated using the Monte-Carlo spectral sets. Energy resolution is shown for three energy slices (in MC generated energy): (a) $10^{18.0}$eV $< E_{\mathrm{GEN}} <$ $10^{18.5}$eV, (b) $10^{18.5}$eV $< E_{\mathrm{GEN}} < 10^{19.0}$eV, (c) $E_{\mathrm{GEN}} > 10^{19.0}$eV. Natural logarithm of the ratio of the reconstructed energy divided by the MC generated energy was used for producing the histograms. 110

5.11. Event reconstruction analysis chain, which is the same for both data and the Monte-Carlo. Pass1 analysis, done by a program called "rufptn", adds two DST banks for each event: "rufptn" (intermediate variables) and "rusdgeom" (geometry results). Pass2 analysis, done by a program called "rufldf", adds a DST bank called "rufldf", which stores the results of the fit to the AGASA lateral distribution function (LDF) and the (reconstructed) event energy. 111

6.1. (a): TA SD Reconstruction efficiency. 100% efficiency plateau ($E > 10^{18.9}$ eV) corresponds to the (geometric) aperture value $A\,\Omega = 890$ km^2 sr. (b): Normalized distributions of the event $\sin^2\theta$ for $E < 10^{18.9}$ eV (open circles) and $E > 10^{18.9}$ eV (filled circles). Dashed and solid lines show linear fits to these distributions. Above the $10^{18.9}$ eV threshold, the acceptance does not depend on the zenith angle: the slope of the solid line is 0.003 ± 0.03. 117

6.2. Generalized TA SD aperture and exposure calculated by the Monte-Carlo method (Equation 6.10). Small-scale features in these quantities seen at $E \sim 10^{19}$ eV and $E \sim 10^{19.8}$ eV are caused by rapid changes in the detector efficiency and the power law of the (MC) input energy spectrum, respectively. (a): Generalized TA SD aperture. For $E > 10^{18.9}$ eV, the aperture becomes $\sim$ 890 km^2 sr. (b): Generalized TA SD exposure over 1080 days of data. Above $10^{18.9}$ eV, the exposure is $\sim$ 2640 km^2 sr. Both (generalized) aperture and exposure include the detector efficiency and the effects of the resolution. 121

6.3. (a): Histogram of reconstructed event energies of the TA SD data in 2008/05/11 - 2011/04/25 range, using 0.1 $\log_{10}E$ binning. (b): Differential cosmic ray flux as a function of event energy calculated from the TA SD energy histogram in (a) using Equation 6.7. The sizes of the last three (highest energy) bins are 0.2, 0.2, and 0.3 in $\log_{10}E$. Error bars show the statistical uncertainties on the flux (68% confidence limits). 122

6.4. Cosmic ray flux measured by the TA SD plotted versus energy. The flux has been multiplied by E^3. The following features are now clearly visible: an ankle (change in the power law) at $E = 10^{18.7}$ eV and a suppression, which begins at $E = 10^{19.7}$ eV. Solid line shows the fit to the broken power law function (Equation 6.12) which is obtained by the fitting procedure described in Equation 6.14. . . 123

6.5. Energy histogram fitted into the broken power law function (Equation 6.12) using the minimization procedure defined by Equation 6.14. Open circles represent N_i and the solid line represents the fit values $N_{\mathrm{BPL}}(E_i)$. Feldman-Cousins 68% confidence limit error bars are attached to the data points N_i for illustration purpose only. Last bin with zero events (shown as an error bar without the data point) is included in the fit. See the text for more details. 125

6.6. Fractional change in the flux after eliminating either $\sigma_{S800}/S800 < 0.25$ or $N_{\mathrm{SD}} \geq 5$ cuts (estimated using Equation 6.19) plotted versus the (reconstructed) event energy. For $E > 10^{18.2}$ eV, the variation is within $\sim 2\%$. (a): Change in the flux when the cut on $\sigma_{S800}/S800$ is removed. (b): Change in the flux when N_{SD} cut is removed. 130

7.1. Comparison of the TA SD (Chapter 6) and HiRes [11] cosmic ray flux results. The results are multiplied by E^3 to emphasize the spectral features. 134

7.2. χ^2 (per degree of freedom) comparison of the TA SD flux (open circles) and the broken power law function (BPL) fit result reported by HiRes in [11] (solid line). 135

7.3. Comparison of the TA SD (Chapter 6) and the AGASA [16] cosmic ray flux results. (a): TA SD superimposed on top of the official AGASA energy spectrum result. (b): Comparison of the TA SD and AGASA results after the AGASA energy scale has been reduced by 28%. 138

7.4. Comparison of the TA SD (Chapter 6) and the Pierre Auger Observatory (PAO) [17] cosmic ray flux results. (a): TA SD superimposed on top of the official PAO energy spectrum result. This version of the PAO spectrum is a combination of the surface detector and hybrid (surface detector and SD) measurements. (b): Comparison of these results after the Pierre Auger energy scale has been increased by 23%. 138

7.5. Determination of $E_{1/2}$ value from the TA SD flux measurement. Integral flux (Equation 6.2) is plotted as a function of energy. Points with error bars are the data, solid line is the result of the fit to the BPL function (Equation 6.12), the dashed line is the extension of the spectral index l beyond the second break E_2, and the dotted line shows the energy $E_{1/2} = 10^{19.69\pm0.10}$ eV, where the integral flux (solid line) becomes 1/2 of that in the absence of the cutoff (dashed line). 142

7.6. TA SD spectrum fitted to the broken power law function (Equation 6.12). Solid lines in both figures show the actual result of the fit, while the dashed lines represent the extension of the power law l beyond the second break E_2, as if the suppression did not exist (dashed lines show the limit $E_2 \to \infty$). Points with error bars represent the data. (a): TA SD flux multiplied by E^3. (b): Energy histogram. If the suppression at E_2 (dotted line) did not exist and the flux continued with the power law $l = -2.68$, one would expect $N_{\text{EXP}} \simeq 54.9$ events (Poisson average) above $E_2 = 10^{19.7}$ eV, while the number of observed events in the TA SD data between May 11, 2008 and April 25, 2011 is $N_{\text{OBS}} = 28$. 144

Chapter 1

Introduction

In 1912, an Austrian-American physicist V. F. Hess discovered [18] that the electroscope discharge rate increased with altitude ∼1 km above sea level. Since the amount of material from the top of the atmosphere reduces with increasing altitude and the intensity of radiation from the Earth decreases, the result clearly implied that the effect was due to radiation from the outer space. Moreover, the measurements taken at night showed that the Sun is not the only source of this radiation. The precise nature of the corresponding primary particles was unknown at the time of the discovery, and the species were named simply "Cosmic Rays" (CR). Modern literature still uses this term in reference to extraterrestrial charged particles.

Over the next two decades, it was established that the primary cosmic rays consist predominantly of positively charged particles [19, 20]. Studies of the geographical latitude and longitude dependence [21] of the CR intensity showed that the observed variations could be explained only by an excess of positively charged primaries interacting with the geomagnetic field. The early measurement techniques included mostly Geiger-Mueller counters and cloud chambers, which allowed registering the cosmic rays and taking snapshots of their trajectories. These measurements also resulted in discoveries of new exotic particles such as the positron, muon, and pion (later also kaon and sigma). The existence of some of these particles had been predicted by pioneering efforts in quantum physics (e.g. [22]), and these experimental discoveries (e.g. positron, [23] and muon [24]) provided the necessary foundation for the successful development of the theory.

Experimental particle physics emerged as a consequence of the discovery and study of cosmic rays. However later, with the advance of particle accelerators, the two fields effectively separated. The aim of cosmic ray research now lies mostly in addressing astrophysical questions using the methods of particle physics and astronomy.

The discovery of the extensive air showers (EAS) in 1938 by P. Auger [25] was a key turning point in cosmic ray history, which later lead to the discovery of ultra-high energy cosmic rays. It turns out that energetic extraterrestrial particles of ultra-high energies are very rare. In a 1 km^2 detector, one would have: $\sim$1 particle per day for $E > 10^{18}$ eV, $\sim$1 particle per year for $E > 10^{19}$ eV, and $\sim$1 particle per century for $E > 10^{20}$ eV (these estimates can be obtained from Figure 1.8). However, they produce cascades of secondary particles (EAS) in the atmosphere of the Earth, and the secondary particles reach the ground level, which makes it possible to reconstruct the primary particles that initiated the EAS using sparsely separated detectors on the ground. B. Rossi [26] pioneered the surface detection technique and later, a ground array experiment Volcano Ranch claimed the discovery of a primary cosmic ray particle of $\sim 10^{20}$ eV [27]. Interactions at such high energies are impossible to achieve even by the present day accelerators such as the Tevatron [28] and the Large Hadron Collider [29]. The detection of ultra-high energy particles resulted in substantial theoretical and experimental efforts aimed at establishing their sources and the mechanisms of acceleration and propagation. These tasks are being currently addressed by measuring and interpreting the primary cosmic ray energy spectrum (flux), mass composition, and the arrival directions. These measurements are made indirectly by observing and reconstructing the extensive air showers.

Before discussing the cosmic ray measurements and interpretation in more detail, we point out an important theoretical finding that proved to be a big experimental challenge over the past 50 years. In the 1960s, Greisen [30], and

Zatsepin and Kuzmin [31] predicted a strong suppression (GZK cutoff) in the cosmic ray spectrum at 6×10^{19} eV due to the interaction of protons with the cosmic microwave background (CMB) radiation [32][33][34], which corresponds to 2.7 K $= 2.4 \times 10^{-4}$ eV blackbody radiation [35]. The maximum energy of the cosmic rays was constrained by the (efficient) energy loss mechanism due to the photopion production via the $\Delta(1234)$ resonance: since the interaction took place in the laboratory frame with hundreds of MeV to 1 GeV γ particles incident on stationary protons, the same must apply for the energetic protons in the environment of the 2.4×10^{-4} eV CMB radiation. The fact that the early experiments Volcano Ranch [27], SUGAR [36], and Yakutsk[37] were reporting events above the 6×10^{19} eV threshold challenged the basic physical principles: the absence of the GZK cutoff would imply the violation of Lorenz invariance. Even more startlingly, the early Fly's Eye experiment, after successfully implementing the new air fluorescence technique pioneered by the experiment at Cornell [38], reported seeing an event of energy 3×10^{20} eV [39], which is the highest measured particle energy to date. In the cosmic ray field, such primaries are called *super-GZK* particles.

Despite the reports of the super-GZK particles by the early experiments, the absence of the GZK suppression could not be proven due to the limited exposure (*area* × *solid angle* × *on-time* factors) of these experiments. The effective collecting areas of the early ground arrays were on the order of tens to a few tens of square kilometers, and the observation time scales of these experiments were typically on the order of 10 years, with a notable exception of Yakutsk experiment [37] which has been taking data for the past 30 years. High-statistics samples at energies $E > 10^{19}$ eV were needed to conclusively prove or disprove the existence of the GZK cutoff. First experiment, sufficiently large to measure cosmic ray flux at $E > 10^{19}$ eV, was the Akeno Giant Air Shower Array (AGASA) [16] (with an area of 100 km^2). The experiment reported the absence of GZK cutoff in 1999 [40].

Within a decade, however, the High Resolution Fly's Eye (HiRes) air-fluorescence experiment, with a significantly larger exposure at energies $E > 10^{19}$ eV, reported the first *observation* of the GZK suppression [11] in 2008, while a clear hint of the effect was already seen in the HiRes data in 2003 [41].

This work is an experimental contribution with aim of resolving the discrepancy between the HiRes and AGASA experiments surrounding the existence of the GZK cutoff. The data used in this work comes from the Telescope Array surface detector (using data collected between May 11, 2008 and April 25, 2011), which is a much larger AGASA-like ground array overlooked by three HiRes-like fluorescence telescopes. The construction of the experiment, operations, and data analyses are managed mostly by the members of the former HiRes and AGASA collaborations.

1.1 Extensive Air Showers

Reconstruction of of ultra-high energy cosmic rays (energy, direction, mass composition) rely on measurements of atmospheric extensive air showers (EAS) induced by the primary particles. A description of the important EAS phenomenology and measurement techniques provided here follows [42], [43], [44], and [45].

1.1.1 Hadronic Core

The extensive air showers produced by $E > 10^{18}$ eV cosmic rays are cascades of billions of secondary particles, which result from the interaction of the energetic primary particles (proton or heavier nuclei) in the atmosphere. Typically, the first interaction occurs within ~ 100 g cm^{-2} with respect to the top of the atmosphere, which can be summarized as follows:

$$proton \rightarrow pions, kaons, baryons, ... \tag{1.1}$$

If the primary particle were a nucleus of energy E_0 and the mass number A, then the EAS should be viewed as a simple superposition of A showers with the primary energy of E_0/A each. The hadronic interactions then continue in the narrow region around the shower axis (direction of the primary particle) called the *hadronic core* until their energy is depleted. Currently, hadronic models such as QGSJET-II [46] have to rely on the extrapolation of the accelerator measurements of cross-sections for these processes at $E > 10^{17}$ eV, which results in large systematic uncertainties in the determination of the EAS energy by cosmic ray experiments that are sensitive to the details of these interactions and do not have alternatives that are less model-dependent.

1.1.2 Electromagnetic Component and Calorimetric Energy

The next important part of the EAS is the electromagnetic (EM) component, which originates from the hadronic core due to the decay of neutral pions (mass $m_{\pi^0} \simeq 135$ MeV and life time $\tau_{\pi^0} \simeq 8.4 \times 10^{-17}$ s [47]):

$$\pi^0 \rightarrow 2\gamma \tag{1.2}$$

(the π^0 particles are mainly produced by the processes in 1.1, as well as by the subsequent kaon decays $K_s^0 \rightarrow 2\pi^0$ and $K^{\pm} \rightarrow \pi^{\pm} + \pi^0$). The resulting γ particles then immediately pair produce ($\gamma \rightarrow e^+ + e^-$) and the subsequent interactions that result in the large EM cascades include the ionization losses and bremsstrahlung (by the secondary charged particles), and pair production, Compton scattering, and photoelectric effect (by the secondary γ particles). This EM physics is implemented in the simulation models such as EGS4 [48].

A special importance of the EM component is attributed to the fact that the charged EM particles carry about 85 to 90% of the energy of the showers induced by $E > 10^{18}$ eV primary cosmic rays [49], and these numbers can be verified experimentally [50] by counting muons (non-electromagnetic part of the shower). This effectively allows for a *calorimetric* energy determination of the primary particle by measuring the net energy deposition into the atmosphere by all EM particles. This method of determining the EAS energy does not heavily rely on the details of the first interaction and subsequent processes in the hadronic core (apart from the remaining 15%), which constrains the systematic uncertainty due to the models to 5% [49].

1.1.3 Fluorescence Detectors

Energy deposition into the atmosphere by charged EM particles results in the emission of the fluorescence photons, which propagate through the atmosphere (including the Rayleigh and aerosol scattering, as well as the ozone absorption [43]) and are collected by the fluorescence detector telescopes. The number of charged particles N at any given slant depth x (from the top of the atmosphere, in g/cm^2) is parametrized by the Gaisser-Hillas longitudinal profile function [51]:

$$N(x) = N_{\max}\left[\frac{(x - x_0)}{x_{\max} - x_0}\right]^{(x_{\max}-x_0)/\lambda} \exp\left[\frac{x_{\max} - x}{\lambda}\right], \tag{1.3}$$

where λ is a phenomenological scale parameter with the value of $\simeq 70$ g/cm^2, x_0 is the point of the first interaction, and $x_{\max}$ is the depth where the maximum number of electrons $N_{\max}$ occurs. The electron lateral distribution is described by the Nishimura-Kamata-Greisen (NKG) function [52]:

$$\rho = \frac{N}{r^2}\left(\frac{r}{r_{\mathrm{M}}}\right)^{s-2}\left(1 + \frac{r}{r_{\mathrm{M}}}\right)^{s-4.5}\frac{\Gamma(4.5 - s)}{2\pi\Gamma(s)\Gamma(4.5 - 2s)} \tag{1.4}$$

where N is the total number of particles, ρ is the particle density (per unit area), r is the perpendicular distance from the shower axis, r_{M} is the Moliere radius, and s is the "age" variable, which characterizes the longitudinal development:

$$s = \frac{3}{1 + 2x_{\max}/x} \tag{1.5}$$

The charged EM particles in the shower excite nitrogen molecules of the air, which then de-excite to their ground state and emit the fluorescence light (isotropically):

$$\frac{\mathrm{d}^2 N_\gamma}{\mathrm{d}l\,\mathrm{d}\Omega} = \frac{YN}{4\pi}\,, \tag{1.6}$$

where $\mathrm{d}N_\gamma$ is the number of fluorescence photons emitted into the solid angle $\mathrm{d}\Omega$ when the electron travels distance $\mathrm{d}l$, N is the number of electrons at a given point in the shower, and Y is the fluorescence yield, which is on the order of $\sim$4 photons per meter per electron, for 10 MeV electrons [53] (in the actual simulations, one should take into account the electron energy dependence, and the Y values will be generally different). The fluorescence light spectrum is shown in Figure 1.1. The measurement is provided by the FLASH experiment [54], where the atmospheric air shower energy deposition was emulated using beams of 28.5 GeV electrons. It is seen that this light is in 300-420 nm range.

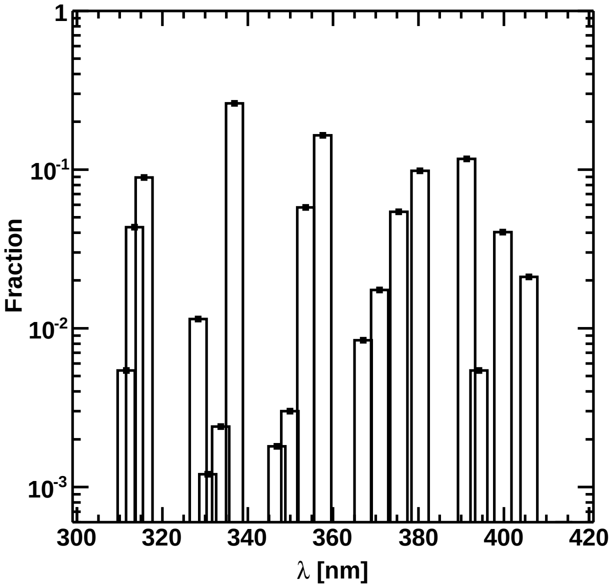

Figure 1.1: Air-fluorescence spectrum measured by the FLASH experiment. Bar widths have been chosen to represent the resolution of the instrument at each point (± 2nm).

Additionally, fast electrons of the EAS emit Cherenkov radiation (number of Cherenkov photons $\mathrm{d}N_{\gamma,C}$ in the frequency interval $\mathrm{d}\nu$ per unit length $\mathrm{d}l$ traveled by an electron):

$$\frac{\mathrm{d}N_{\gamma,C}}{\mathrm{d}l\,\mathrm{d}\nu} = \frac{4\pi\alpha\delta}{c}(1 - E_t^2/E^2)\,, \tag{1.7}$$

where $\delta \equiv n - 1$ (n is the index of refraction of air), α is the fine structure constant, E is the electron energy, and $E_t \simeq 0.511\ \mathrm{MeV}/\sqrt{2\delta}$ is the minimum threshold energy for emitting the Cherenkov light by electrons. The Cherenkov light is not isotropic but follows an angular distribution (θ is the angle to the shower axis):

$$\frac{\mathrm{d}N_{\gamma,C}}{\mathrm{d}\Omega\,\mathrm{d}l} = \frac{\mathrm{d}N_{\gamma,C}}{\mathrm{d}l}\exp(-\theta/\theta_0)/\mathrm{sin}\theta\,, \tag{1.8}$$

where $\theta_0 \simeq 0.83E_t^{-0.67}$ [42]. The Cherenkov light is estimated and subtracted because it is easier to determine the numbers of particles along the shower axis using only the fluorescence light (with smaller systematic uncertainties). Also, the fluorescence detectors are not optimized for measurements of the direct Cherenkov light (cases of showers coming directly at the detector).

The geometry of the shower is reconstructed using the time of the arrival of the fluorescence photons at the photomultiplier tubes (PMT) of the detector cameras (for a brief description, see Chapter 2). The flux of the fluorescence photons is then determined from the PMT pulse height readings and the total (calorimetric) energy deposition into the atmosphere by the EM component is inferred. At the final step, the energy of the primary particle is recovered by correcting for the missing energy, i.e. raising the electromagnetic calorimetric energy by 10 to 15% of its value to account for the contributions that were not a part of the electromagnetic component [49].

An important parameter of the EAS, also reconstructed by the fluorescence detectors, is the depth of the shower maximum x_{max} in Equation 1.3. From the simplest model, where the number of particles in the shower doubles after every (slant depth) distance step D, until their energies reach some minimum value

E_{min} (below which the ionization losses prevent the production of new particles, e.g. for $e^{\pm}$, $E_{\mathrm{min}} \sim 2$ MeV) it is easy to convince oneself that the place where the maximum number of particles occurs is related to the atomic number A of the primary particle: $x_{\mathrm{max}} \propto D \log[E/(A\, E_{\mathrm{min}})]$. Such dependence enables the study of the mass composition (on statistical basis) of ultra high energy cosmic rays using the fluorescence detector.

1.1.4 Muon Component

Muons are mainly produced by the (leptonic) decays of charged pions (mass $m_{\pi^{\pm}} \simeq 140$ MeV and life time $\tau_{\pi^{\pm}} \simeq 2.6 \times 10^{-8}$ s [47]) and kaons (mass $m_{K^{\pm}} \simeq$ 490 MeV and life time $\tau_{K^{\pm}} \simeq 1.2 \times 10^{-8}$ s [47]), originating from the hadronic core:

$$\pi^{\pm} \rightarrow \mu^{+}(\mu^{-}) + \nu_{\mu}(\bar{\nu_{\mu}})$$
$$K^{\pm} \rightarrow \mu^{+}(\mu^{-}) + \nu_{\mu}(\bar{\nu_{\mu}})$$

The secondary cosmic ray muons are usually close to their minimum ionizing energy of 100 MeV to 1 GeV [47], which makes them long-lived (muon mass and life time are $m_{\mu^{\pm}} \simeq 106$ MeV and $\tau_{\mu^{\pm}} \simeq 2.2 \times 10^{-6}$ s [47]) and penetrating. Therefore, muons (as well as electrons and gamma) can make a significant contribution to the signal measured by the ground array detectors. Also, the ground arrays can be designed to measure the electromagnetic component separately from muonic component: counters that register signals from the muons only can be placed underground for shielding them from the EM component [37]. The reason for doing such measurements is that the ratio of numbers of electrons to muons is sensitive to the mass composition of the primary particle. If the energy of the primary is fixed, then in the case of a smaller mass number, the $\pi^{\pm}$ particles within the hadronic core are more energetic and thus are more likely to interact rather than decay into muons, so that more neutral pions are produced, which in turn feed the electromagnetic component of the EAS. The main difficulty of using the electron to muon ratio method for composition studies at high energies ($E > 10^{17}$ eV) is that this quantity is very sensitive to the details of interactions at the hadronic core, and systematic errors due to the hadronic models are difficult to control. An example of an on-going study can be found in [55]. The secondary muons carry less than 15% of the total EAS energy for $E > 10^{18}$ eV primary particles [49].

Examples of currently available tools that allow detailed computer modeling of the extensive air showers by simulating the hadronic interactions and transport of the secondary particles through the atmosphere to the detectors are CORSIKA [56], COSMOS [57], and AIRES [58]. These tools combine the hadronic interaction models of the highest energies (e.g. QGSJET-II) with those of the EM component (e.g. EGS4) and the low energy hadronic models (e.g. FLUKA [59]). For any given primary (cosmic ray) particle type, direction of incidence, and energy, these simulation tools predict the secondary particle fluxes (also their energy spectra and angular distributions) throughout all stages of the EAS development. This, in principle, enables one to calculate the photon fluxes (either fluorescence or Cherenkov) at the camera telescopes of the fluorescence detectors, and also the time and the number of particle distributions on the ground, needed by the ground arrays.

1.1.5 Surface Detectors

Surface detectors (ground arrays) typically sample the fluxes of the secondary cosmic ray particles (muons, electrons, gammas) at the ground level resulting from the EAS. Some detectors, e.g. Yakutsk [37], can also measure the direct Cherenkov light (Equation 1.7). While the sampling areas of individual surface counters range from 1 to 10 m^2, the detectors (in modern UHECR ground array experiments) are deployed using large inter-counter spacing, ranging from 1 to

1.5 km. As a result, the observation areas covered by the ground arrays range from 100 to 3000 km^2.

The surface detector (SD) counters are typically made of either plastic scintillators that emit the scintillation light when penetrated by the particles (e.g. AGASA [16] and Telescope Array SD, described in Chapter 2), or water tanks, which are sensitive to the Cherenkov light produced by the secondary particles in the water (e.g. Pierre Auger SD, [17]). The detectors record the particle number densities (or the energy deposition in the counters) and the particle (signal) times. The shower arrival direction is then reconstructed using the time of the counters that were hit, and the shower lateral distribution profile (particle number density or energy deposition versus distance from the shower axis) is determined from the counter pulse heights. The energy of the primary cosmic ray is estimated from the lateral distribution information. A detailed description of the EAS reconstruction by the Telescope Array SD will be given in Chapter 5.

1.2 UHECR Mass Composition

Ultra high energy cosmic ray (UHECR) composition is currently inferred from the fluorescence detector measurements of the position of the shower maximum x_{max} (Equation 1.3). At present, conflicting measurements of the UHECR composition exist. According to the High Resolution Fly's Eye (HiRes) experiment, which reported the mean x_{max} measurements made in the Northern hemisphere [2], the mass composition of UHECR is predominantly light (protonic) for $E > 1.6 \times 10^{18}$ eV. Figure 1.2 shows the HiRes x_{max} result. The Pierre Auger Observatory (PAO), on the other hand, reports the measurements (made in the Southern hemisphere) which indicate that the UHECR mass composition becomes heavier (more iron-like) above $\sim 3\times10^{18}$ eV, as Figure 1.3 shows. Finally, the preliminary

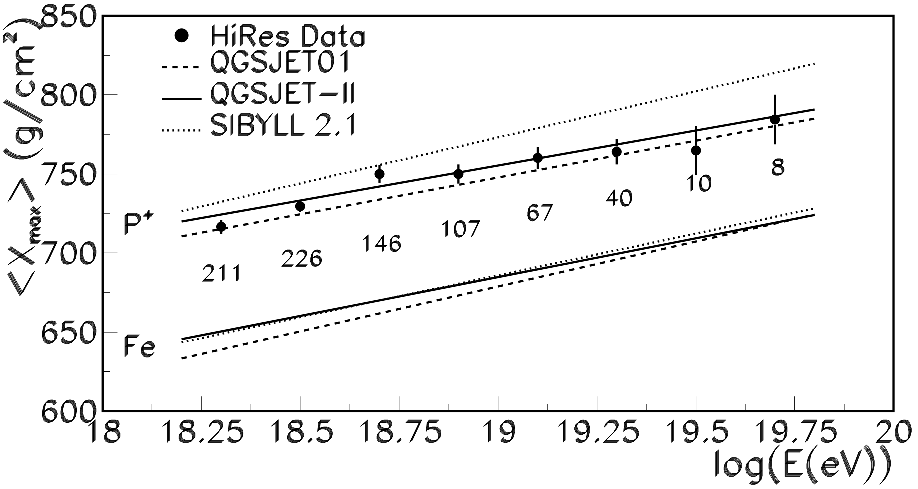

Figure 1.2: HiRes mean $x_{\max}$ result [2]. Points with error bars are the data and lines represent the predictions of the hadronic models for the proton and iron primaries. According to this result, the UHECR primary particles consist of mostly protons above 1.6×10^{18} eV.

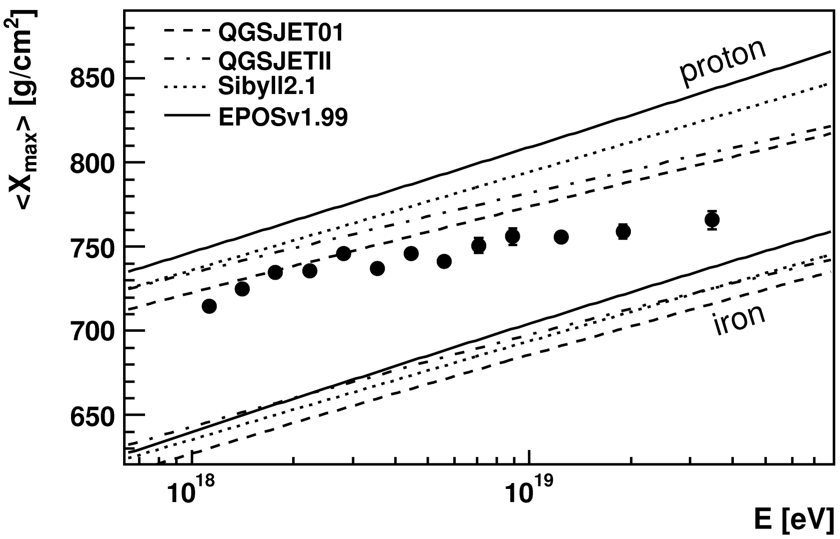

Figure 1.3: Pierre Auger mean $x_{\max}$ result [3] (points with error bars) plotted on top of the predictions from the hadronic models (lines) for the proton and iron primaries. The Pierre Auger data suggests that the composition becomes heavy above 3×10^{18} eV.

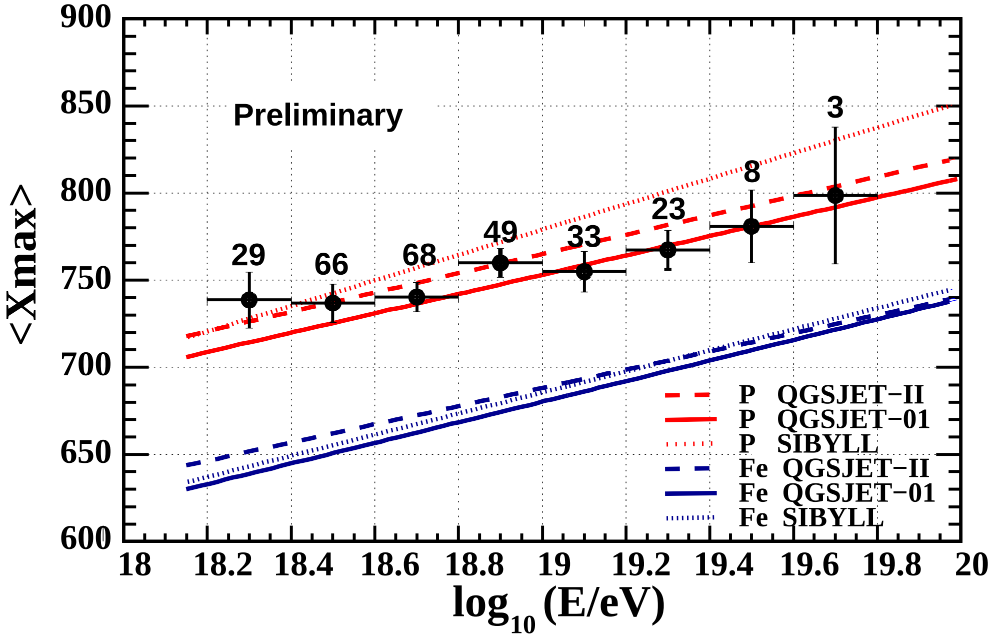

Figure 1.4: Preliminary Telescope Array measurement of the mean x_{max}, adopted from [4]. Points with error bars are the data and lines show the hadronic model predictions for the proton and iron primary particles. This result shows that the UHECR mass composition is consistent with protons above 1.6×10^{18} eV.

results of the Telescope Array experiment [4] shown in Figure 1.4 favor the proton-like composition above 1.6×10^{18} eV.

The knowledge of the UHECR mass composition is necessary for interpreting the cosmic ray anisotropy and the energy spectrum results, as will be shown below. The controversial results reported by the HiRes, PAO, and the TA experiments may be indicative of either a North and South asymmetry of the UHECR sources (or propagation), or this discrepancy could be attributed to the poorly understood systematic uncertainties of the analyses. Establishing whether the later is true is currently an on-going effort among the three collaborations.

1.2.1 UHECR Anisotropy

A direct way of finding the sources of UHECR is by examining the event arrival directions. The charged particles, however, are deflected by the galactic magnetic field (GMF) of the Milky Way galaxy before reaching the Earth. The GMF field is on the order of 1 to 4 μG and the thickness of the galactic disk is $\sim$ 300 pc [10]. The deflection angle is the ratio of the distance d traveled in the GMF B to the Larmor radius R_L:

$$\Delta\theta \simeq \frac{d}{R_L} \simeq 0.52^\circ \, Z \, \frac{10^{20}\ \text{eV}}{E} \, \frac{d}{1\ \text{kpc}} \, \frac{B}{1\ \mu\text{G}}\,, \tag{1.9}$$

where E and Z are the energy and the charge number of the primary particle, respectively. A more detailed calculation of the deflection angle of the proton primaries of $E \simeq 4 \times 10^{19}$ eV is shown in Figure 1.5 [5], where the Tinyakov-Tkachev parametrization of the GMF is used [6]. From Equation 1.9, it is clear that the charged particle astronomy is possible only in the case of light composition (small Z values) and by examining the highest energy events (generally $E > 10^{19}$ eV), otherwise the GMF makes the directions of the UHECR sources untraceable (by distorting the charged particle trajectories).

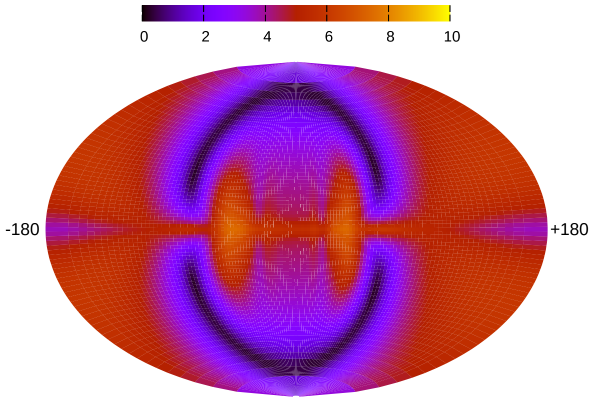

Figure 1.5: Deflection angle due to the GMF for $E \simeq 4 \times 10^{19}$ eV proton adopted from [5], which uses the GMF model described in [6]. The color-coded result (in degrees) is plotted in Galactic coordinates (galactic latitude vs galactic longitude) using the Hammer-Aitoff projection.

Figure 1.6 shows a map of UHECR arrival directions above 4×10^{19} eV measured by 3 experiments in the Northern hemisphere. HiRes stereo [7] has an angular resolution (68% confidence level) of 0.5°, the resolution of the AGASA [8] SD is 1.6°, and the TA SD (this work, using TA SD data in May 11, 2008 to April 25, 2011 range) angular resolution is 1.5° (c.f. Chapter 5). A detailed report of the anisotropy results from the Telescope Array measurements, which include a larger data sample from the TA SD, is expected to appear in [60]. It should be pointed out that both HiRes and TA SD have larger exposure than the AGASA. However, the energy estimation by the AGASA experiment is systematically larger than that of HiRes and the TA SD (c.f. Chapter 7) by ∼20%, which resulted in a larger number of events above 4×10^{19} eV reported by the AGASA. As Figure 1.6 shows, there are no obvious point sources (excesses in the cosmic ray intensity) currently seen by these experiments. Possible explanations are:

- Insufficient statistics. UHECR sources are numerous and therefore, a larger

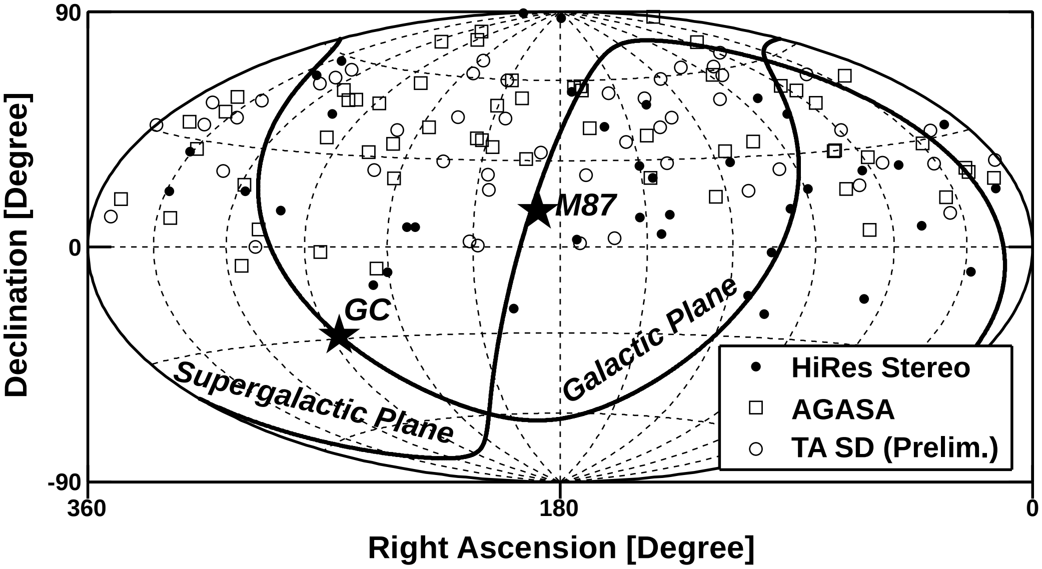

Figure 1.6: Arrival map of $E > 4 \times 10^{19}$ eV events in equatorial coordinates (using Hammer-Aitoff projection) reported by three experiments in the Northern hemisphere: HiRes [7], AGASA [8], and the TA SD (preliminary, using data in May 11, 2008 to April 25, 2011 range). Additionally, stars label the locations of the center of the Milky Way galaxy (GC) and the Messier 87 (M87), a large elliptical galaxy 16.7 Mpc away [9].

data sample is required before the sources can be resolved.

- Poorly understood extragalactic magnetic fields (regular and turbulent) [10], which can distort the charged particle trajectories and make the measurements of anisotropy more difficult.
- Heavier mass composition (larger Z values) [3]. It should be noted, however, that currently two experiments in the Northern hemisphere are reporting proton dominated UHECR composition above $10^{18.2}$ eV [2, 4].

1.3 UHECR Accelerators

Currently, there are no identified sources that can accelerate particles to ultra-high energies. However, one can speculate of what the potential sources might be based on a simple argument, originally proposed by Hillas [10]: the Larmor radius of the charged particle being accelerated should be within the size of the accelerator (astrophysical object). The maximum acceleration energy achievable by an astrophysical object is then limited to:

$$E_{\mathrm{MAX}} = \Gamma\, Z\, e\, B\, R\,, \tag{1.10}$$

where Γ is the Lorentz factor due to the bulk motion in the source, $Z\,e$ is the charge of the accelerated particles, B is the magnetic field inside the source, and R is the source size. Figure 1.7, called the *Hillas plot*, shows a summary of possible astrophysical sources capable of accelerating p and Fe primaries to 10^{20} eV energies.

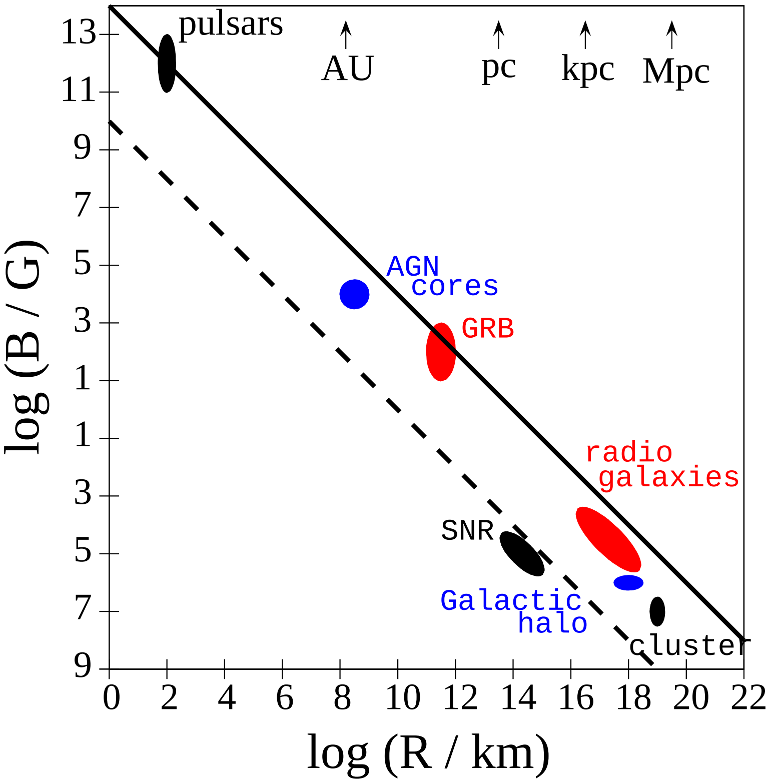

Figure 1.7: Hillas plot adopted from [10]. Magnetic field strength is plotted versus the size of the potential accelerator. Acronyms in the figure should be interpreted as follows: AGN - active galactic nuclei, SNR - supernova remnants, GRB - gamma ray bursts. Astrophysical objects capable of accelerating iron and proton nuclei to 10^{20} eV should lie above the dashed and solid lines, respectively.

1.4 UHECR Spectrum

1.4.1 Power Law Nature

Figure 1.8 shows the differential cosmic ray (CR) flux with respect to energy, for $E > 100$ TeV, measured by the following experiments: Akeno [61], AGASA [16], Tibet [62], Fly's Eye [63], HiRes [11], Yakutsk [37], KASCADE-Grande [64], and Pierre Auger Observatory [17]. The Telescope Array Surface Detector (TA SD) spectrum points are a result of the work described later in this paper. On the

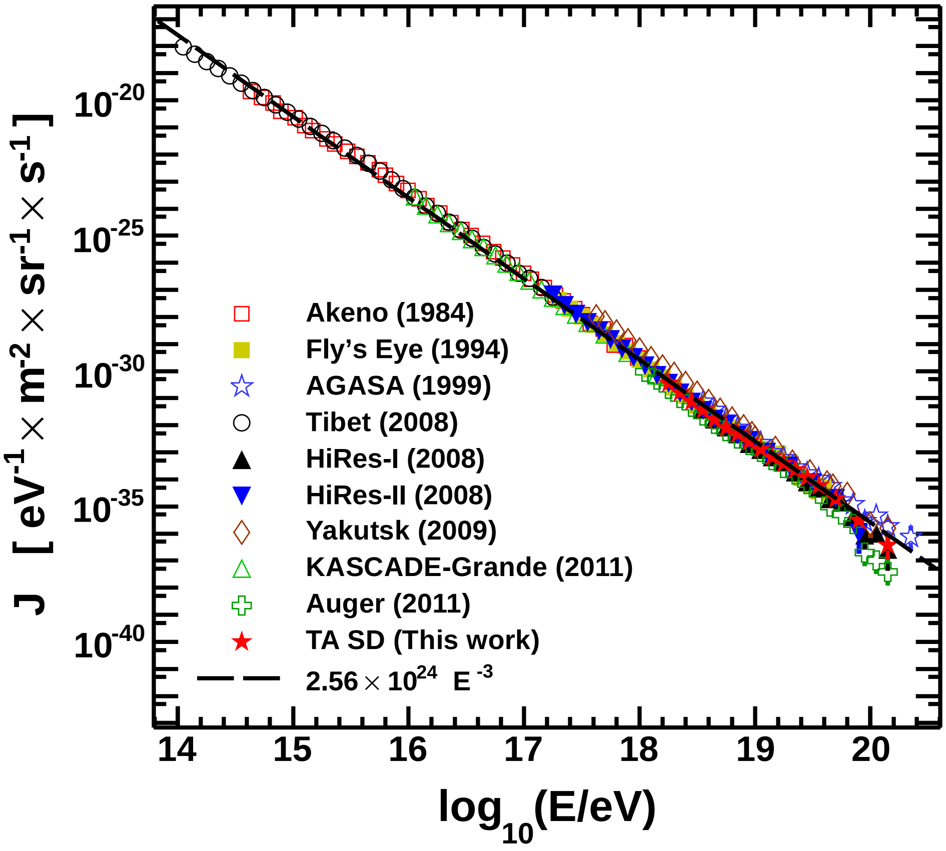

Figure 1.8: Differential cosmic ray flux for $E > 100$ TeV reported by a variety of experiments. The flux is plotted versus the logarithm of energy. Dashed line is a least-squares fit to a single power law function of index -3.

large scale, the CR flux follows the shape of a single power law function, to a good approximation:

$$J(E) \simeq (2.56 \times 10^{24}\ \mathrm{eV}^{-1}\,\mathrm{m}^{-2}\,\mathrm{sr}^{-1}\,\mathrm{s}^{-1}) \left[\frac{E}{\mathrm{eV}}\right]^{-3} \tag{1.11}$$

This implies that the CR are of non-thermal nature: otherwise, the flux would peak somewhere, rather than continuing as a single power law. A model, which explains the CR acceleration up to 10^{17} eV and results in a power law flux prediction was proposed by E. Fermi. It assumes that the charged particles are accelerated by the hydrodynamic shocks (carrying strong irregular magnetic fields) near the supernova remnants. Currently, the Fermi model is accepted as a possible acceleration mechanism for the galactic cosmic rays (originating within the Milky Way galaxy), although no direct experimental evidence exists to date. An interested reader should consult standard texts [52] and [65] for more details.

1.4.2 Knee at $\sim 3 \times 10^{15}$ eV

While the main subject of this discussion concerns the UHECR, it should be pointed out that there is a prominent feature in the CR spectrum visible in Figure 1.8: a change in the power law near $\sim 3 \times 10^{15}$ eV that forms the shape of a knee. One explanation is based on the following observation. The critical energy E_C of the proton primaries ($Z = 1$), such that the protons can be contained effectively by random galactic magnetic fields $B \sim 3\ \mu$G [66], can be estimated from the requirement that the particle Larmor radius is of the same order as the correlation length of the magnetic field domains $l_C \sim 0.1$ kpc [66]:

$$E_C = Z\,e\,B\,l_C \simeq 3 \times 10^{17}\ \mathrm{eV} \tag{1.12}$$

Since E_C is much larger than $\sim 3 \times 10^{15}$, the natural interpretation is that the $\sim 3 \times 10^{15}$ eV knee is caused by the maximum acceleration energy available at the galactic sources. The fact that the the position of the knee depends only on the rigidity E/Z [10] fits this explanation also: galactic sources can accelerate heavier nuclei to higher energies, which scale with Z.

1.4.3 Ankle and a Break above $10^{18.0}$ eV

Figure 1.9 shows the cosmic ray flux measured by HiRes [11] and AGASA [12] experiments, multiplied by E^3 to emphasize the features beyond the overall $\sim E^{-3}$ fall off. While the two results have a clear systematic energy shift (with AGASA energy estimation being $\sim$ 20% higher than that of HiRes, c.f. Chapter 7), it is clear that the two spectra have a changing power law feature ($10^{18.65}$ eV for HiRes and $\sim 10^{19.0}$ eV for AGASA) that forms an ankle. Another prominent feature is the break that begins at $E \simeq 10^{19.65}$ eV in HiRes case but not seen in the AGASA result. A model of extragalactic proton propagation in the 2.7 K cosmic microwave background (CMB) developed by Berezinsky *et.al.* [13] explains simultaneously both features seen in HiRes spectrum and fits the proton composition reported by HiRes [2]. In the model, the spectral features are caused by the proton energy

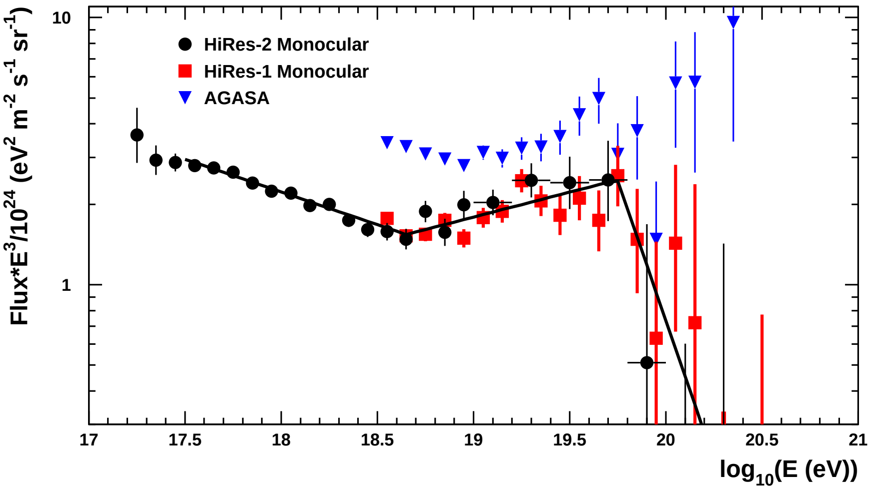

Figure 1.9: Energy spectrum measured by the High Resolution Fly's Eye experiment [11], with superimposed result of the AGASA experiment [12]. The plot is adopted from [11].

losses due to the red-shift (Hubble expansion of the universe), pair production of the CMB photons in the vicinity of the energetic proton, and the photopion production via the Δ-resonance (the GZK mechanism, [30, 31]). Figure 1.10 shows a detailed calculation of the proton energy losses due to these processes.

Figure 1.11 shows the fits [13] to the observed energy spectra of the AGASA and HiRes experiments. The energy loss model from the Figure 1.10 is used for calculating the fit values for the observed spectra. In all cases, non-evolving cosmological source model was assumed and the generated spectrum (as produced by the sources) was assumed to be of the form $J_g \propto E_g^{-2.7}$ (E_g are the energies generated by the sources). Curves 1 and 2 correspond to the maximum E_g values of 3×10^{20} eV and 1×10^{21} eV, and curve 3 is the case of no maximum limit on E_g. The deviation from the fit curve for energies $E < 10^{18}$ eV is caused by the cosmic rays originating within our galaxy [13] because the galactic cosmic rays are not included in this model. The ankle corresponds to the place where the energy loss due to the red-shift becomes comparable to that due to the pair production, and the cutoff (in the HiRes data) corresponds to the place where the photopion production turns on. The results from the HiRes and AGASA experiments are clearly incompatible and require a further experimental verification.

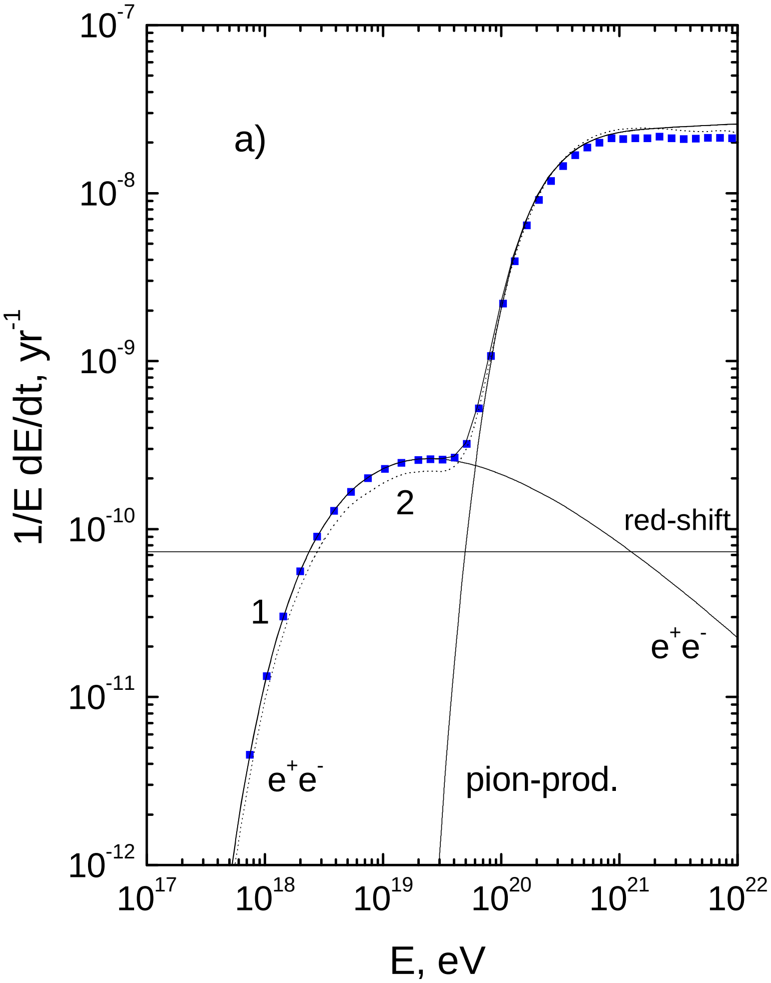

Figure 1.10: Contributions to the energy losses for the proton primaries propagating in the cosmic microwave background plotted versus the proton energy. Solid (1) and dotted (2) curves are results of calculations by Berezinsky *et. al.* [13] and the squares points correspond to the calculation by Stanev *et. al.* [14]. The plot is adopted from [13]. Labels "$e^+ e^-$", "pion-prod" and "red-shift" correspond to the energy losses due to the pair production, photopion production, and the expansion of the universe, respectively.

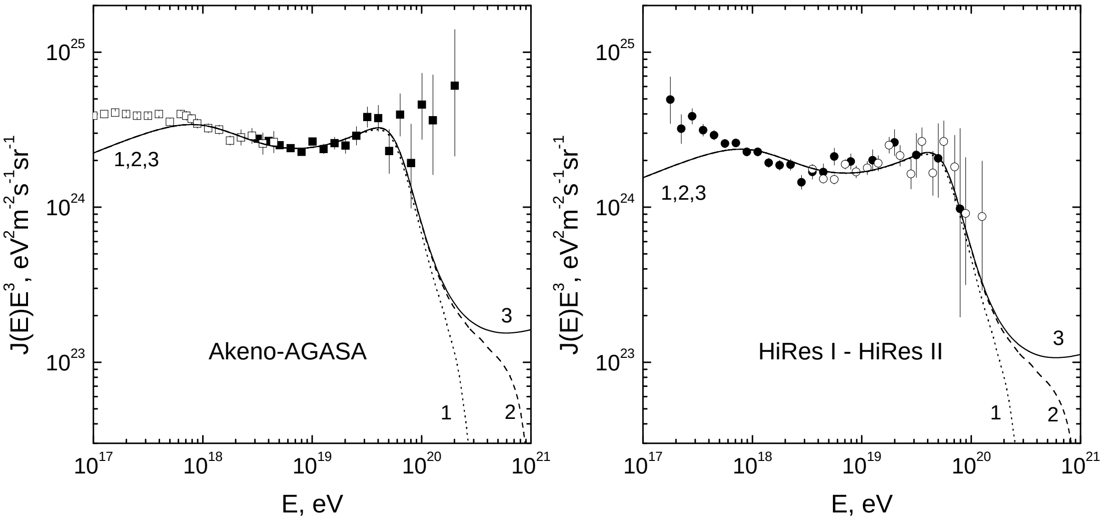

(a) (b)

Figure 1.11: Fits to the energy spectrum results of (a) AGASA (with rescaled energies) and (b) HiRes, done by Berezinsky *et. al.*. The plot is adopted from [13]. See the text for more details.

Chapter 2

The Telescope Array Detector

The Telescope Array is the largest cosmic ray detector in the northern hemisphere designed for measuring the extensive air showers (EAS) induced by the ultra high energy cosmic rays (UHECR) in the atmosphere of the Earth. The TA is located in Millard County, Utah, with GPS coordinates of $39^{\circ}11'20''$ North, $112^{\circ}54'31''$ East, and 1370 m above the sea level (876 $\mathrm{g/cm^2}$ vertical mass overburden). These coordinates correspond to the TA Central Laser Facility(CLF) placed in the middle of the detector and primarily used for the atmospheric calibration purposes of the TA fluorescence detectors. We first present a general overview of the TA detector, and then discuss each detector type separately in subsequent sections. Since the main focus of this paper is the analysis of the TA SD, we will keep the discussion of the fluorescence detector details brief.

The Telescope Array consists of a surface detector array of 507 plastic scintillation counters, separated by 1200 m on a square grid, covering 680 $\mathrm{m^2}$ area on the ground, and overlooked by 3 fluorescence detector stations, as shown in Figure 2.1. Open square boxes correspond to the positions of the scintillation counters, the solid line marks the edge of the SD array, the triangles represent the communication towers (CT) used by the SD data acquisition system, and the dashed arrows represent the azimuthal fields of view of of the TA fluorescence detectors: Black Rock Mesa (BR), Long Ridge (LR), [67] and Middle Drum (MD) [68]. Description of the detector geometries is provided in corresponding sections of this chapter.

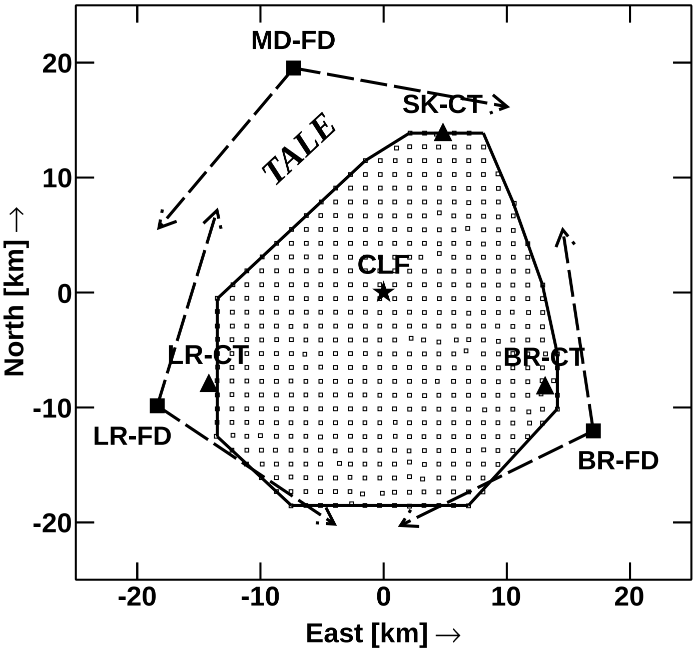
MD-FD
SK-CT
TALE
CLF
LR-CT
BR-CT
LR-FD
BR-FD
North [km] →
East [km] →
20
10
0
-10
-20
-20
-10
0
10
20

Figure 2.1: The Telescope Array Detector

Measurements by TA provide the cosmic ray arrival direction, energy spectrum, and the cosmic ray mass composition. These measurements are currently performed in the $E > 10^{18}$ eV energy range. A proposal exist to extend this sensitivity down to $\sim 10^{16}$ eV by including the TA low energy extension detector (TALE) in the North-West side of the existing 1200 m TA SD array. The comparison of the surface detector trigger efficiencies is shown in Figure 2.2. The proposed infill array will be a combination of 400 m and 600 m spacing surface detectors, and Figure 2.2 shows that the trigger efficiency drops to 10% at $E = 10^{16.0}$ eV for the 400 m separation array. When the trigger efficiency is much less than 10%, it becomes difficult to reliably estimate the aperture; all arrays have a 100% trigger efficiency after 10^{19}eV. The area near the MD labeled as "TALE" in Figure 2.1 has thus been reserved for closely spaced low energy extension infill arrays. The TALE fluorescence telescopes, with high elevation angle coverage, will be added

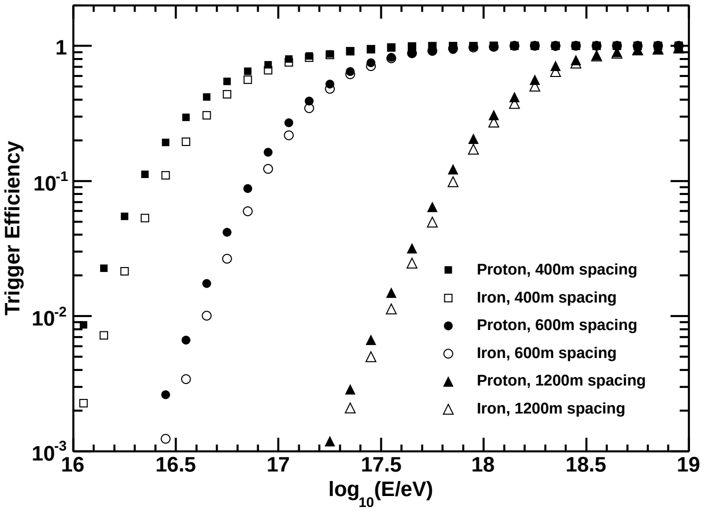

Figure 2.2: TA SD Trigger efficiency obtained from simulations for the cases of proton and iron. Counters in the currently operating SD array are separated by [1200 m] (triangles) and the efficiency plateaus at $\sim 10^{19}$ eV. Squares and circles correspond to the (proposed) TALE infill array which will have counters separated by 400 m and 600 m.

to the MD site. The construction work on TALE detectors has began at the end of 2011, and the data collection is expected to start by the end of the year 2012.

Currently designed TA detector is continuously taking cosmic ray data since the completion of its construction in the end of the year 2007. Figure 2.3 shows the integrated on-time versus date over ∼3 years of data, and Figure 2.4 shows the aperture of each TA detector. Fluorescence detector information was used from [69], [68], and [70].

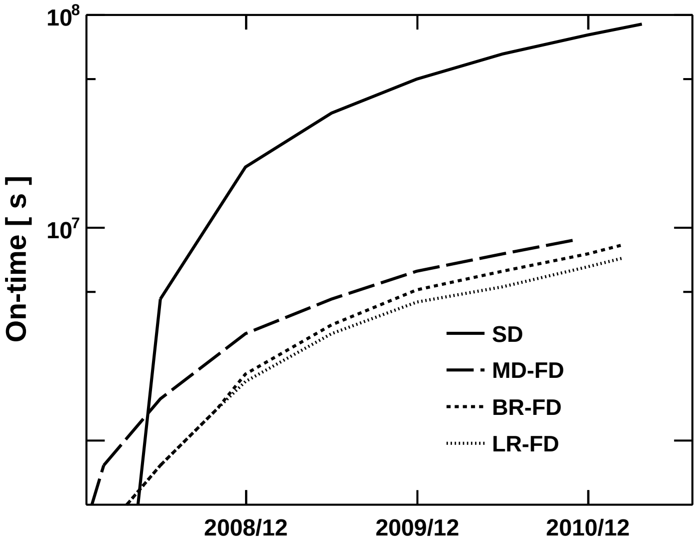

Figure 2.3: TA On-time. Total observation time for each detector is plotted versus (Gregorian) date.

The air-fluorescence detectors successfully measure inclined shower events up to $60 - 70^o$ in zenith angle, while the TA surface detector currently reconstructs events only with zenith angle $\theta < 45^o$. High energy cosmic rays also produce more light in the atmosphere and can be seen by the fluorescence detectors at increasingly larger distances, while the TA surface detector is constrained by a fixed area on the ground. These effects make the TA SD aperture smaller than the TA MD by a factor of ∼4 at $E = 10^{20}$eV, as seen in Figure 2.4. While the

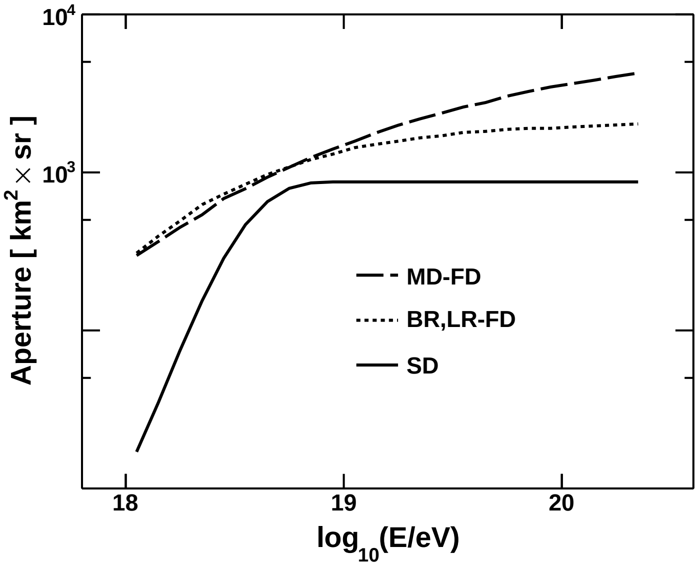

Figure 2.4: TA Aperture. Area × solid angle × efficiency for each detector working in stand-alone mode is plotted for every 0.1 bin in logE (E is the cosmic ray energy). Effects of trigger and reconstruction of each TA detector are included.

TA FD has a clear advantage in terms of area and solid angle coverage, the duty cycle of the fluorescence detectors is severely limited by daylight and weather conditions, so that the on-time of any TA fluorescence detector is a factor ∼10 smaller than that of the SD, as seen in Figure 2.3. From these considerations, the TA SD has at least a factor of 2.5 larger exposure in area and solid angle than any of the TA air-fluorescence detectors, when the exposure is integrated over the highest energies starting at $E \sim 10^{18.8}$eV.

While the TA surface detector has superior statistics in measurements of event arrival directions and the energy spectrum, it should be noted that the TA fluorescence detector sees the full longitudinal profiles of the air showers in the atmosphere and therefore determines their energies more accurately than the TA SD, a fact which is needed later for determining the SD energy scale more accurately than the one provided by the current hadronic models. Also, the FD longitudinal profile is used for determining the mass composition of the primary cosmic ray particles, when the event geometries are well constrained by simultaneous FD and SD measurements. Such events are called the “hybrid events”, and for this reason, the TA is often referred to as a “hybrid “ cosmic ray detector in the literature. Despite the large differences in their stand-alone performances, both detector types complement each other in measuring important physical quantities.

2.1 Air-Fluorescence Detector

The Telescope Array has 3 fluorescence detectors, sensitive to 300-420 nm fluorescence light, isotropically emitted due to the atmospheric energy deposition by charged particle cascades produced in the course of the development of extensive air showers. The relevant light is in the ultra-violet (UV) range, thus the FD can operate only during moonless nights and in dry weather conditions, when the scattered light pollution is minimal. Consequently, to maximize the FD duty cycle and the quality of data, the Telescope Array experiment has been deployed in the desert of Utah.

Figure 2.5 shows the arrangements of the camera units (mirror and cluster box pairs) used by the TA FD, and Figure 2.6 shows their fields of view, where the altitude is plotted versus elevation as seen by each photomultiplier tube (PMT) in coordinate systems of each FD station. Mirrors focus the UV light from cosmic ray showers onto the cluster box cameras, which consist of 256 PMTs, covered by the UV filters to reduce the noise from external light pollution.

2.1.1 Black Rock Mesa and Long Ridge

The TA Black Rock Mesa and Long Ridge FDs are new detectors, each having two rings of mirrors, with mirrors of ring 1 placed over the ring 2 mirrors in both BR and LR cases (Figure 2.5a). There are 12 mirrors per station, 3 m in diameter each. Both FDs cover 3 - 33° in altitude, and 108° in azimuth (Figure 2.6), and

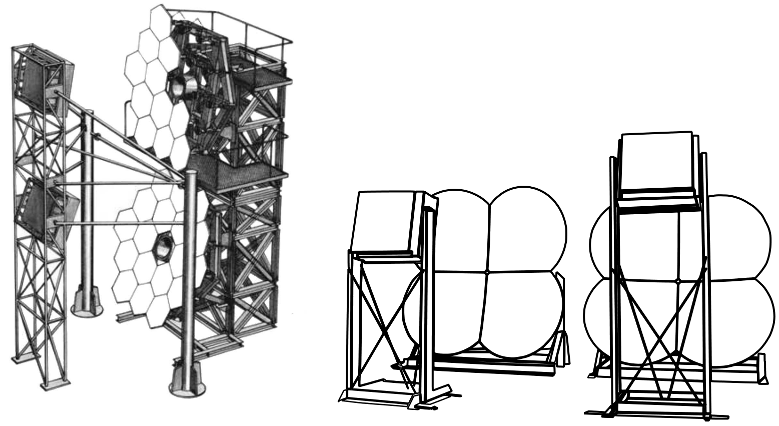

(a) (b)

Figure 2.5: Mirror and cluster box arrangements used by the Telescope Array fluorescence detectors: (a) Black Rock Mesa or Long Ridge, (b) Middle Drum.

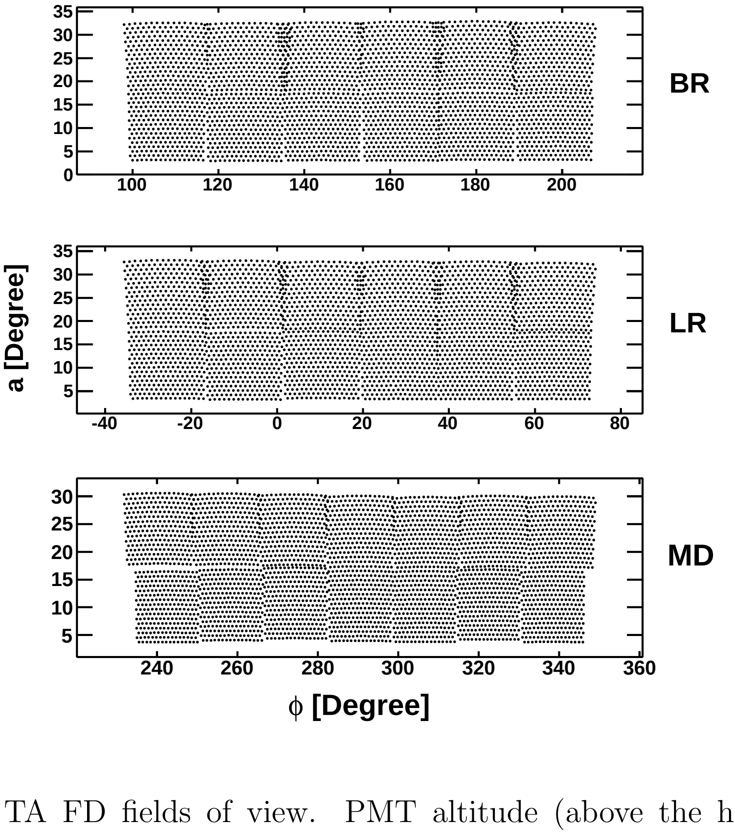

Figure 2.6: TA FD fields of view. PMT altitude (above the horizon) versus azimuth (in coordinate systems of each FD) are plotted. Each PMT effectively samples a $\sim 1^\circ$ cone on the sky.

their PMT signals are recorded by 10 MHz FADC devices. A detailed description of these detectors can be found in [67] and [71].

2.1.2 Middle Drum

The TA MD was built from existing components used previously by the HiRes experiment [72]. The MD detector has 14 refurbished HiRes-II mirrors, 2 m in diameter each, which are also deployed in a 2 ring configuration. Ring 1 mirrors are placed next to the ring 2 mirrors (Figure 2.5b) and they cover 3 - 31° in altitude and 112° in azimuth (Figure 2.6). The PMT times and pulse heights are read out separately by a TDC and an ADC sample-and-hold integrator. For a detailed description of the TA MD, one should consult [68].

2.2 Surface Detector

In this section, we describe the important components of an individual TA SD unit, which include the the exterior bulk parts, communication devices, electronics components, and parts sensitive to the energy depositions by ionizing particles. We also describe measurements and simulations directly related to the characteristics of each individual TA SD counter, as well as the low level triggers, which are locally decided by the electronics of each counter. The event (global) trigger, data acquisition, calibration, and full Monte Carlo simulation are discussed in the next chapters.

2.2.1 Exterior Parts and Communication

Figure 2.7 shows an exterior view of a TA surface detector unit. The scintillation layers and photomultiplier tubes, which are sensitive to radiation, are enclosed in a 1.2 mm thick, 2.3 m×1.7 m×10 cm stainless steel box and are housed under a 1.2 mm thick iron roof (item 5 in Figure 2.7). The unit uses a 12 V deep cycle

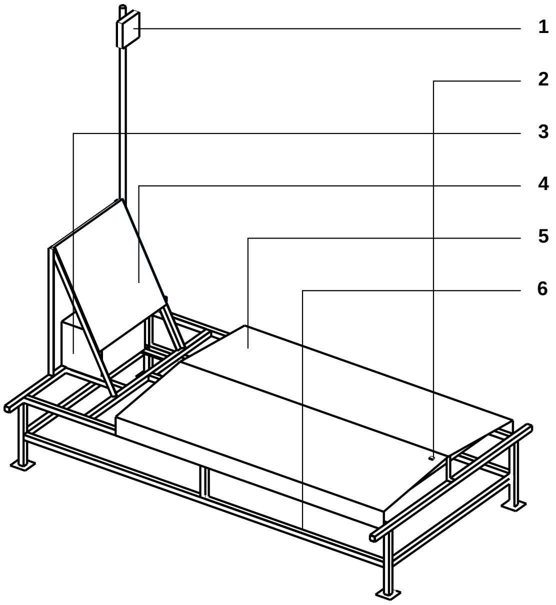

Figure 2.7: Exterior view of the TA surface detector unit: 1 - Wireless communication antenna, 2 - GPS receiver, 3 - Battery and electronics box, 4 - Solar panel, 5 - Iron roof, 6 - Supporting metal frame.

battery to operate its electronics at 5 W (item 3). The battery is automatically charged during the daylight by a 1 m^2, 125 W solar panel unit [73], which is shown in Figure 2.7, item 4. This ensures a nearly 100% data collection duty cycle of the TA SD.

Since the TA SD counters are placed sparsely over a large area on the ground, using the fiber optic cables, to synchronize the outputs of each SD unit as did the AGASA experiment [16] is unfeasible. To match the data in time and to transfer voluminous data produced by the FADC systems of each counter, the TA instead uses GPS and wireless communication. The readings of all counters are synchronized in time using GPS Motorola M12+ modules of 10 nS resolution [74] (item 2 in Figure 2.7), mounted on the roof of each detector. The data is transmitted to the collecting towers by a 2.4 GHz wireless radio [75] using directional antennas (item 1) . The wireless local area network (WLAN) modules are ADLINK540 and use a customized networking protocol that is based on IEEE 802.11b and provides a transfer rate of 11 MB/s, which is sufficient for the TA SD calibration and data acquisition purposes.

2.2.2 Sensitive Part

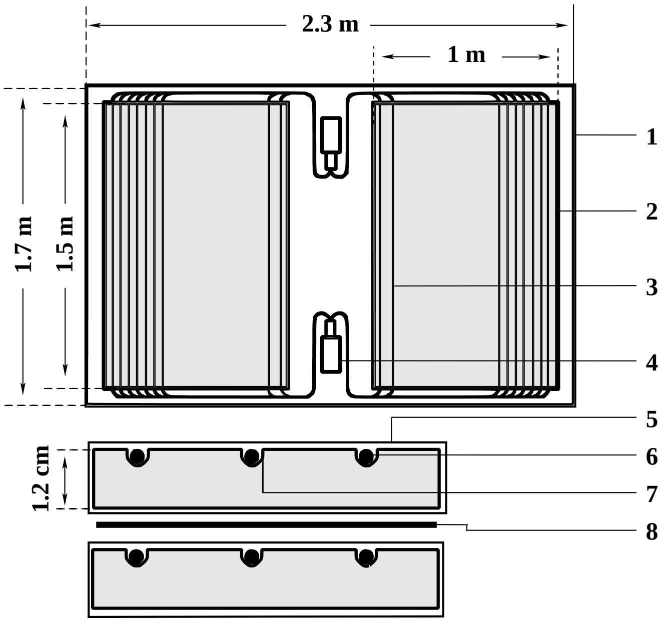

Figure 2.8: TA SD interior configuration, top view (top) and the cross-sectional view (bottom). 1 - Stainless steel enclosure box, 2 - Scintillator (right side of, represented by the shaded area), 3 - Wavelength shifting fiber (WLS), 4 - Photomultiplier tube, 5 - Tyvek sheet, 6 - WLS (cross section), 7 - Grooves for the WLS placement, 8 - Separator plate

Figure 2.8 shows the schematics of the interior of the TA SD unit [73] [76] [77]. The sensitive detector is the part from which the particle ionizing energy deposition is read out. In TA SD, this is the two layers (upper and lower) of 2 m x 1.5 m x 1.2 cm plastic scintillator, which use polyvinyl toluene (C_9H_{10}, 1.032 g/cm^2) as base and Y-11 Kurray wavelength shifting fibers (WLS) to reduce the frequency and attenuation of the light and to direct it to the PMTs. Each of the two (upper, lower) layers is read out by a separate PMT. The PMTs operate at $\sim$ 1000 V and provide a gain of $\sim 2 \times 10^6$ per photoelectron. As can be seen from Figure 2.8 (item 2, shaded area), each layer is additionally divided into two 1 m x 1.5 m x 1.2 cm pieces, one on each side of the PMTs (both pieces of the same layer are read out by a single PMT). Each of the 1 m x 1.5 m x 1.2 cm pieces is composed of 4 sub-units, 25 cm x 1.5 m x 1.2 cm each. Next, the TA SD uses 104 WLS, 47 cm long and 1 mm in diameter each (items 3 and 6 in Figure 2.8). These fibers are placed into 1.2 mm (in diameter) grooves made in the base scintillator(polyvinyl toluene) (Figure 2.8, item 7). The adjacent grooves are separated by 2 cm. Lastly, both scintillator layers are separately wrapped in Tyvek sheets, and there is a 1 mm thick stainless steel separator plate between them (Figure 2.8, items 5 and 8).

2.2.3 Vertical-Equivalent Muon (VEM) Definition

Figure 2.9 shows the mean ionization energy deposition of a vertical muon in one of the 1.2 cm thick (1.24 g/cm^2) layers of scintillator obtained from a GEANT [78] [76] simulation of the TA SD. A broad minimum occurs around 300 MeV, which is called the minimum ionizing energy. Since the energy loss is much smaller than the particle kinetic energy, the statistical distribution of the energy loss (deposition) is well approximated by the Landau distribution [79], as Figure 2.10 shows. A small tail on the left is due to the edge effects. We define the *vertical-equivalent muon* (VEM) unit of energy deposition to be 1 VEM $\equiv$ 2.05 MeV, which is the *most probable* energy deposition for a vertical muon at the minimum ionizing energy (300 MeV).

2.2.4 Electronics, Level-0 and Level-1 trigger

The important electronics components of the SD unit are the charge controller, WLAN modulus, main board, GPS, FPGA, FADC, and the CPU boards, all contained in the electronics box (item 3 in Figure 2.7). We mostly focus on parts

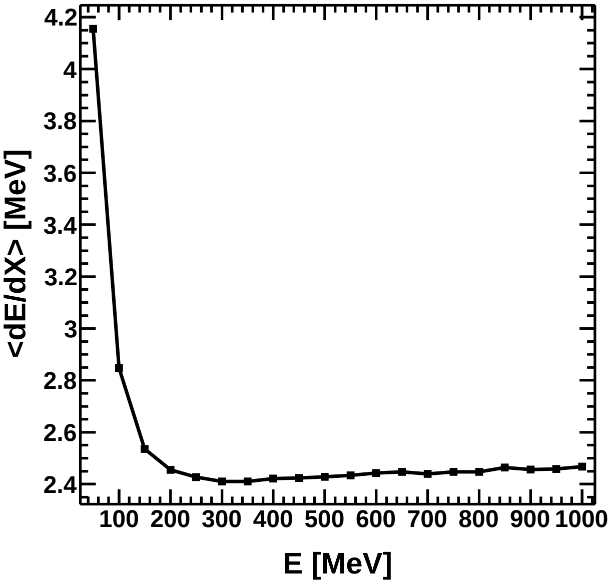

Figure 2.9: Mean energy deposition in a 1.2 cm thick scintillator by a vertical muon plotted versus muon kinetic energy, obtained from a GEANT4 simulation. The minimum ionizing energy occurs at 300 MeV.

directly related to the physical measurements. More details on the designs can be found in [74], [73], and [1].

The charge controller is responsible for monitoring the battery condition and applying charge from the solar panel as needed. Figure 2.11 shows a battery charging cycle of a typical TA SD counter with respect to the hour since the UTC midnight. Dark period shows as a gradual decrease in voltage (2 - 14 h window) while the steep rise and fall correspond to the solar power turning on (∼14 h) and off (∼0 h).

The CPU (SH4, Renesas, 266 MHz) executes the data acquisition software and controls the electronics and information readout processes, which occur either locally, using a serial port or through the wireless communication (WLAN). In most cases, tasks such as the assessment of the detector conditions, configuration, and adjustment of software parameters are done remotely using the wireless

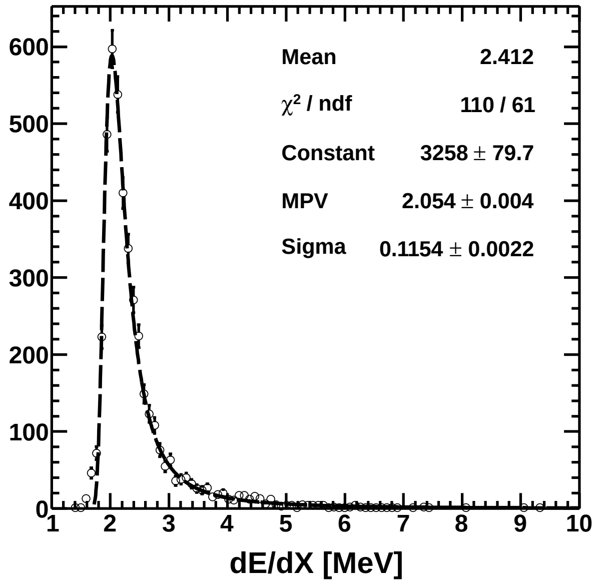

Figure 2.10: Energy loss histogram of a vertical 300 MeV (minimum ionizing) muon in the 1.2 cm scintillator, obtained from a GEANT4 simulation. The MPV (most probable value) defines the VEM unit, which is 2.05 MeV for the TA SD. Dashed curve shows a fit to the Landau function.

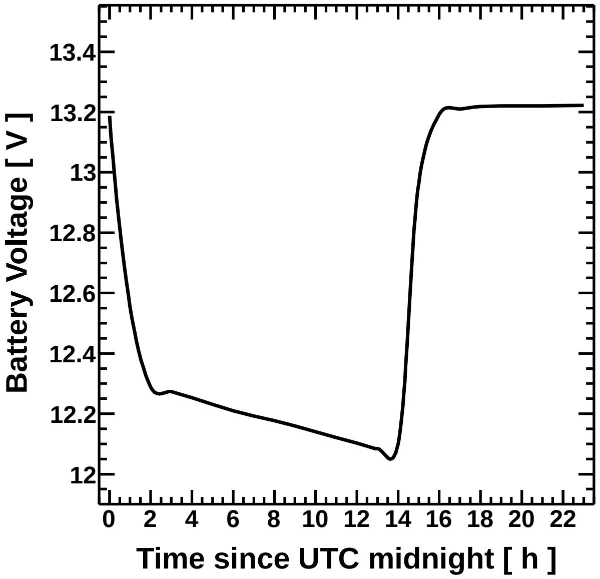

Figure 2.11: Battery charging cycle of a typical SD unit plotted versus time since UTC midnight (10/24/2011).

communication.

The next major component is the Flash Analog-to-Digital Converter (FADC) board, which is used for digitizing the signals produced by the two PMTs. The FADC is of 12 bit precision and is sampled at a 50 MHz rate by the CPU board. The digitized PMT signal, called *waveform*, thus has a 1/50 MHz = 20 nS time resolution and the maximum (digitized) signal size per 20 nS time bin is $2^{12} = 4096$ FADC counts. The waveforms are always sampled in pairs, one from each PMT (corresponding to the upper and lower scintillator layers), and the extent of each waveform is 128 FADC time bins (2.56 μS) as shown in Figure 2.12. Waveforms with integrated signal exceeding 15 FADC counts above the pedestal in both layers in coincidence correspond to the *Level-0 trigger* (Figure 2.12a). Such waveforms are stored in a circular buffer and can be sent to the communication towers, if requested. Waveforms with integrals over 150 FADC counts above the pedestals in coincidence between the two layers correspond to the *Level-1 trigger*

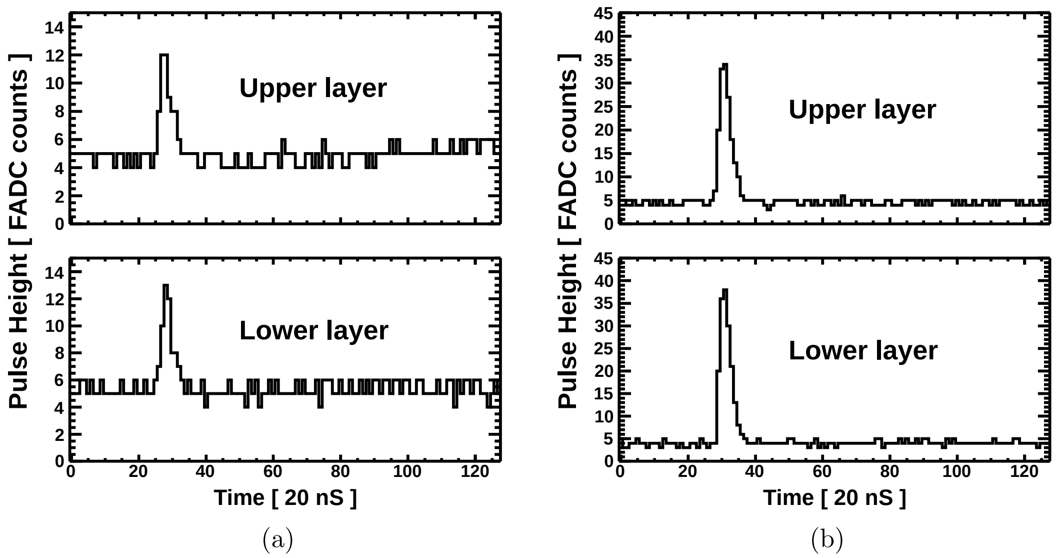

(a)

(b)

Figure 2.12: TA SD Waveforms: (a) corresponds to the Level-0 and (b) to Level-1 triggers. Flat regions surrounding the pulses, called *pedestals*, are ~ 5 FADC counts / time slice in these examples.

(Figure 2.12b), and such signals always reported to the communication towers. Waveform time stamps are assigned by the GPS and an additional 50 MHz (20 nS resolution) sub-clock mounted on the main board. Up to 10 waveforms (25.6 μS total) from each SD unit can be sent to the tower per request. The software executed on communication tower computers then examines all Level-1 trigger waveforms and decides whether the event trigger, which is also called the *Level-2 trigger*, should be issued. Details of the event trigger and the data acquisition process are described in the next chapter.

Last item is the Field-Programmable Gate Array (FPGA, Xilinx SPARTAN 3) chip, which is attached to the CPU board. The chip monitors the FADC outputs and decides on the trigger. The chip also adjusts the pedestals to maintain the Level-1 trigger rate close to ~ 30 Hz and the Level-0 rate at ~ 750 Hz, which is roughly equal to the rate of random atmospheric muons.

2.2.5 Monitoring

Each surface detector unit accumulates monitoring information over a 10 minute period. The information is then transferred to the communication tower over the following 10 minutes, while new (updated) monitoring data is being collected. These *monitoring cycles* repeat indefinitely, and there are 144 cycles per day per counter. The monitoring cycles consist of histograms and status variables of every SD unit.

Information relevant for calibrating the detector are the *1-MIP* and pedestal histograms. All Level-0 pulses are integrated over 12 FADC time slices (240 nS) and saved into a histogram called the 1-MIP histogram. The rate is that of the Level-0 trigger ($\sim$ 750 Hz). For the pedestal case, all FADC signals are integrated over 8 FADC time slices (160 nS) and the results are sampled at a $\sim$6.25 MHz rate. Figures 2.13a and 2.13b show the examples of 1-MIP and pedestal histograms collected over a 10 minute monitoring cycle by a typical TA SD counter. Small non-Gaussian tails on the right seen in the pedestal histograms are mostly due to the atmospheric particles, occurring at a rate much smaller than 6.25 MHz, thus producing a $\sim$ 750 Hz/6.25 MHz $\simeq$ 0.01% effect. The tails on the right in the 1-MIP histograms are mostly caused by asymmetric fluctuations in the energy deposition by the atmospheric particles. The effects due to multiple particles occurring in the same 240 nS pulse integration window are negligible. For example, the contribution of the double-muon signals is only $\sim$ 750 Hz $\times$ 240 nS $\simeq$ 0.02%. Muons at the minimum ionizing energy are the most abundant atmospheric particles capable of penetrating through the metal enclosure of the scintillator, which means that the Level-0 triggers are dominated by minimum ionizing particles (MIP). Histograms of all Level-0 signals (1-MIP) and pedestals are used in the off-line analyses for determining the detector gain in FADC counts per MeV of energy deposition in each scintillator or, equivalently, in FADC counts per VEM (2.05 MeV). While we describe the calibration in detail in

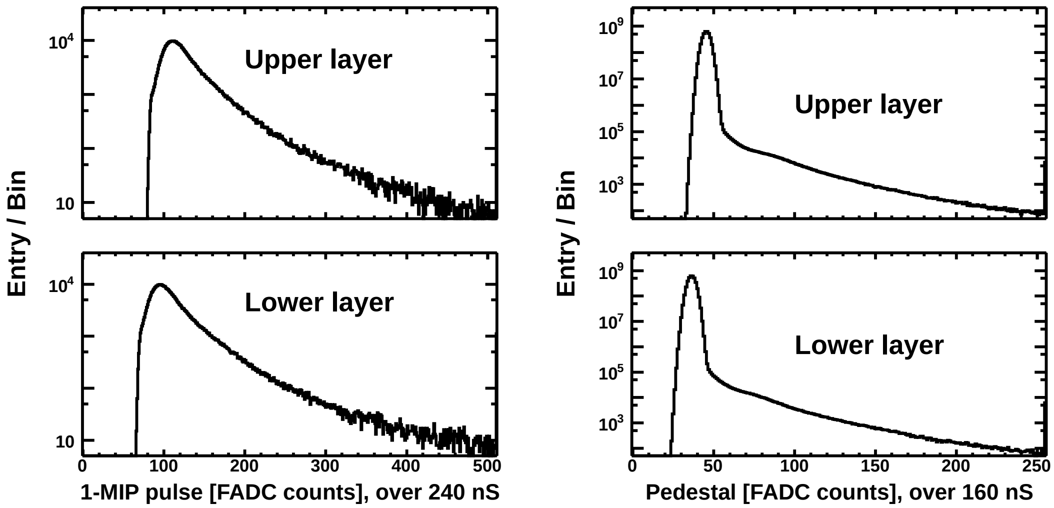

(a) (b)

Figure 2.13: Calibration histograms from a typical TA SD counter collected over a 10 minute period (monitoring cycle). (a) are the 1-MIP histograms, sampled at ∼750 Hz for upper and lower layers in coincidence. (b) are the pedestal histograms, sampled at ∼6.25 MHz for each layer.

the next chapter, we note here that the Level-0 trigger (15 FADC counts above the pedestal) roughly corresponds to 0.3 MIP energy deposition and Level-1 trigger (150 FADC counts above pedestal) correspond to ∼3 MIP in a typical TA SD scintillator.

Chapter 3

TA SD Data

The steeply falling nature of the cosmic ray energy spectrum results in relatively large rates of primary particles of $E \ll 10^{18}$ eV. For a successful reconstruction of the air showers, it is required that sufficient numbers of the daughter particles reach the ground level on distance scales of $\sim$1200 m from the core of the shower, producing detectable signals in multiple counters. Moreover, since the thin scintillation counters mostly measure the energy losses of minimum ionizing particles, the counter pulse heights need to be sufficiently large to avoid fluctuations which have an adverse impact on resolution. These factors effectively constrain the range of the TA SD reconstruction to $E > 10^{18}$ eV, which is taken into account in the design of the TA SD stand-alone trigger and data acquisition. To achieve timely storage and retrieval of the data, and to optimize the required storage space, the TA SD implements an elaborate scheme of selecting and recording useful event and calibration information. We provide a detailed description of these processes, as well as the TA SD data format and calibration in the sections that follow.

3.1 Trigger and Data Acquisition

The TA SD array is logically divided into 3 sub-arrays, each responding to its own designated communication tower (CT), as shown in Figure 3.1. An additional boundary that divides the array into the three parts, which we call the *T-shape boundary*, is represented by dashed lines. Currently, 170 counters respond to BR-CT, 189 to LR-CT, and 148 to SK-CT (507 counters total). When the TA SD began its operation in March 2008 (stable data begins on May 11, 2008), the 3 sub-arrays were triggering and recording data independently. On November 10, 2008, the trigger and the data acquisition (DAQ) software were updated to allow for an additional cross-tower communication, so that the entire array triggers as a single unit.

When the event trigger is issued, the data is recorded by all three communication towers separately and stored in the ASCII format on their local hard drives. The data is then compressed and transferred, on a daily basis, from the temporary CT storage space to a computer inside the Millard County Cosmic Ray Center, Delta, UT, where it is saved and recorded on DVD disks. The disks are distributed to the TA collaboration and subsequent event and calibration time matching are performed by the off-line analysis programs.

3.1.1 Labeling Counters (Logical ID)

Before describing the data acquisition, we first need to introduce the counter position ID system. Since most of the counters are positioned (nearly) on the 1200 m square grid, it is natural to use their X and Y position values for their logical identification. Figure 3.1 shows the position ID scheme used by the TA SD. In the CLF coordinate system with suitably adjusted origin (X = -14.69 km, Y = -19.73 km, Z = 0) and distance measured in 1200 m units, counter X and Y positions are nearly integers. This provides a unique labeling of every counter by just one integer number: ID = $X \times 100 + Y$. This labeling scheme is used by the TA SD data acquisition system and throughout the rest of the analysis.

3.1.2 Trigger

Each SD unit automatically sends Level-1 trigger ($\geq$150 FADC counts, $\sim$3 MIP) signals to corresponding communication towers (c.f. Chapter 2). Lists of positions

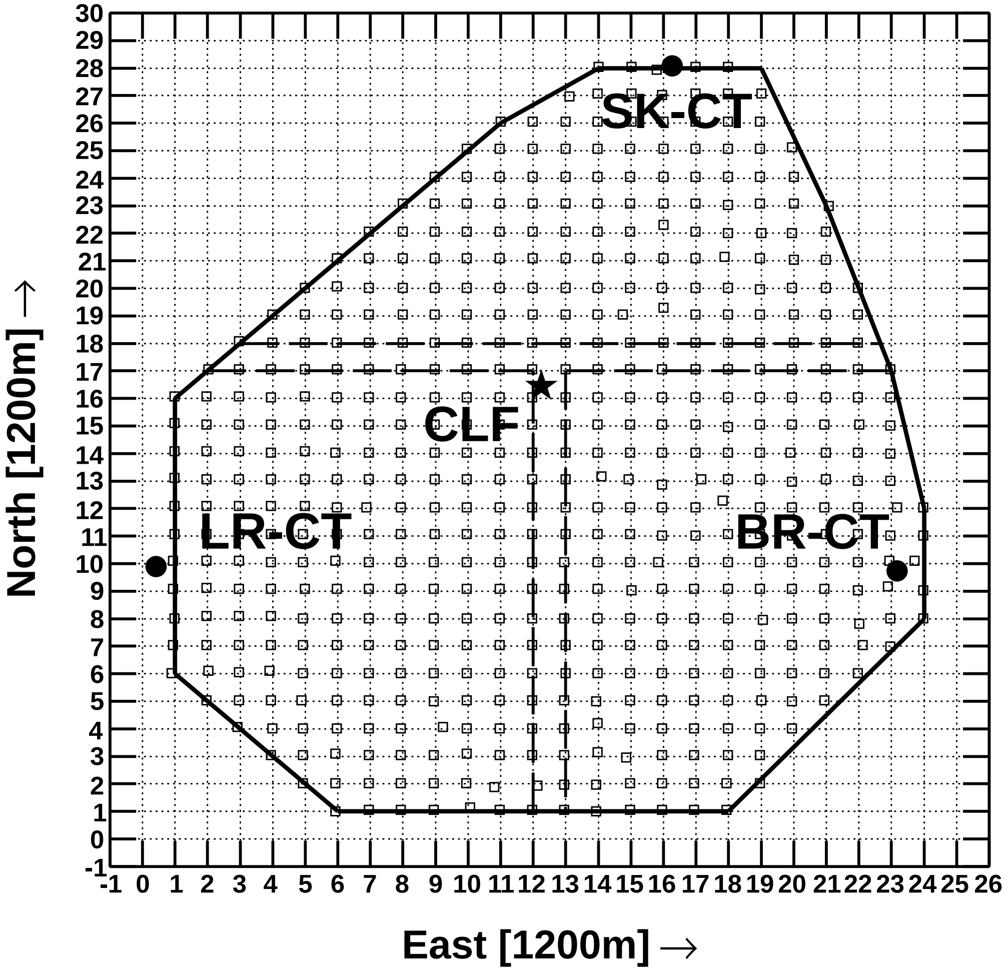
North [1200m] →
East [1200m] →
SK-CT
CLF
LR-CT
BR-CT
30
29
28
27
26
25
24
23
22
21
20
19
18
17
16
15
14
13
12
11
10
9
8
7
6
5
4
3
2
1
0
-1
-1 0 1 2 3 4 5 6 7 8 9 10 11 12 13 14 15 16 17 18 19 20 21 22 23 24 25 26

Figure 3.1: TA SD counters deployed on a 1200 m grid shown using the CLF coordinate system with the origin redefined at X = -14.69 km, Y = -19.73 km, and Z = 0. Additionally, the distance is measured in 1200 m units so that most (physical) counter locations are nearly on the grid, allowing one to identify the counters by the integer parts of their X and Y positions. The (integer) counter position ID is described by one number, which is ID = $X \times 100 + Y$. Filled circles represent the communication towers, location of the CLF is labeled by the star, solid line describes the edge of the array and dashed lines show the T-shape boundary, which divides the array into 3 logical sub-arrays. Counter positions are marked by open squares.

of Level-1 trigger counters (logical ID numbers) and their signal times constitute the *trigger tables*. The trigger tables are stored in circular buffers on communication tower computers and are continuously scanned for the *Level-2* (event) trigger patterns, displayed in Figure 3.2. Level-2 triggers are issued whenever

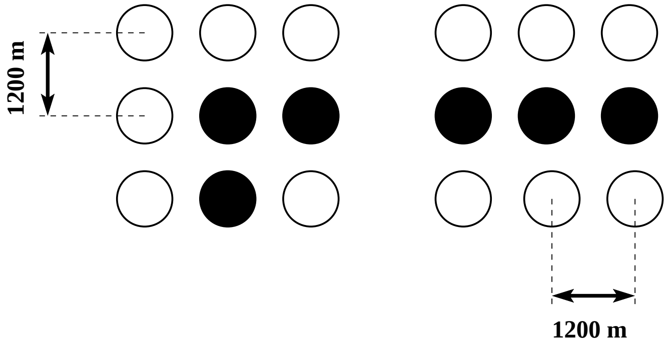

Figure 3.2: TA SD trigger patterns, up to rotations by $\pi/2$. Circles represent counters on a 1200 m square grid. Filled circles correspond to Level-1 trigger counters ($\geq\sim$3 MIP) occurring in the same 8 μS window. Any pair of Level-1 trigger counters is within 2 spacing units (2400 m).

such patterns of 3 adjacent counters, within 2400 m on the grid and $\geq$150 FADC counts ($\sim$3 MIP) each, fire in the same 8 μS window [80, 81, 77].

3.1.3 Data Acquisition

When the Level-2 trigger is called, the software on communication towers (the firmware) first creates the *event trigger time*, which is the time stamp of one of the Level-1 trigger counters from the triplet which first met the trigger pattern requirement. The firmware then saves the event time information (integer second and microsecond) into the data stream, marked with a special event label. Next, the communication towers request all Level-0 waveforms (≥ 15 FADC counts, or $\sim$0.3 MIP) from all counters within $\pm\, 32$ μS of the event trigger time and save the counter positions (logical unit numbers), waveform time stamps, and digitized signals in FADC counts (in 20 nS time slices). As mentioned in Chapter 2, there can be up to 10 Level-0 trigger waveforms from each counter. Finally, the event ending (after all waveforms have been recorded) is clearly marked in the data stream to simplify the data parsing by the off-line analysis programs.

3.1.4 Monitoring Data

As described in Chapter 2, each surface detector unit accumulates monitoring histograms over 10 minute monitoring cycles and sends the results to designated communication towers. The transfer of monitoring information occurs over 10 minutes also, while new monitoring data is being collected. The sending/receiving process is synchronized with the GPS one-second pulses (1-PPS). Each second of a (600 second long) monitoring cycle is identified with a certain part of the monitoring data acquired from all counters by the communication tower. The first monitoring cycle of the day always begins exactly at midnight in UTC and the last cycle ends at 23:59 UTC. The UTC second since midnight modulo 600, called the *second number*, is an important quantity which not only characterizes the monitoring information, but is also used in encoding the event time stamps in the raw data, as will be shown in the later section which describes the format of the data.

3.1.5 Hybrid Trigger

External triggers due to the TA fluorescence detectors are an important extension of the surface detector stand-alone trigger. Low energy events, which can be reconstructed by the FD but do not generate the Level-2 trigger patterns (Figure 3.2) would be missing in the SD data. However, even one counter can provide valuable time information on the ground for constraining the event geometry, resulting in a better reconstruction than that of the FD in stand-alone mode. This problem has been solved by introducing the *hybrid trigger*, a protocol which prompts the data acquisition in the same way as the Level-2 trigger, if requested so by a signal from any of the three TA FD stations. The hybrid trigger events are clearly marked in the data and can be easily separated from the actual Level-2 triggers if one were to analyze the SD data only. The hybrid trigger has been deployed in 09/2010.

3.2 Raw Data Format

We describe the output ASCII file format as recorded by the collecting towers, using BR-CT as an example. The outputs from the other two towers are identical in form, except for different counters. This description involves three major parts: GPS time keeping, event data, and monitoring (calibration) information. After the off-line parsing process is complete for all towers for the entire day, any time matching event and monitoring data must be combined and grouped into event and (10 minute long) calibration packets, containing readings of all counters from all three communication towers.

3.2.1 GPS Time Information

The acquisition and transfer of monitoring data are synchronized by the GPS 1 second pulses (1-PPS). For every second, recorded quantities include the UTC date and time (up to a second), the number of Level-1 triggers received by the tower from its counters, and the number of the GPS satellites seen by the tower. This information is also used for determining the event times up to the integer second (second fractions relative to the GPS integer second are recorded separately). The GPS 1-PPS status information is recorded in the raw data every second using the format described in Table 3.1.

Line in the data file: “#T 006b3980 111017 132405 5204 245 5”

Column #	Value	Description
1	#T	GPS time stamp delimiter
2	006b3980	Counting the time stamps for troubleshooting purposes (hexadecimal)
3	111017	UTC date: year 2011, month 10, day 17
4	132405	UTC time: hour 13, minute 24, second 5
5	5204	Number of Level-1 triggers received by the tower in 1 second
6	245	Second since midnight modulo 600, for a consistency check: $(13 \times 3600 + 24 \times 60 + 5) \mod 600 = 245$
7	5	Number of GPS satellites seen at this time

Table 3.1: Description of the GPS time stamp

3.2.2 Event Data

Shown below is the (abbreviated) appearance of the event information in the raw data file:

```
E 0000ed5c 0f545714

W 1317 1

w 0 0 132

40d901fa

02f6036e

00005006

01005007

........

7f005007

02faee56

35102632

........
```

```
### DONE 925894 0f545714
```

Event data begins with the header information, described in Table 3.2. To determine the event date and time, one must refer to the *most recent* GPS time information (Table 3.1) in the data, which has the same second since midnight modulo 600 value as that in the event header. The event trigger micro-second described in Table 3.2 corresponds to the time of one of the counters in the triplet that was first found to meet the trigger criteria (Figure 3.2) and is typically well within ± 10 μS of the time when the shower core hits the ground (from the event reconstruction), as shown in Figure 3.3. This time is mainly used for the purposes of time matching the events among different TA detectors, as well as determining which counters are relevant and should be read out by the TA SD data acquisition system.

Line in the data file: “E 0000ed5c 0f545714”

Column #	Value	Description
1	E	Event header delimiter
2	0000ed5c	Event trigger ID (hexadecimal)
3	0f545714	Hexadecimal encoding of the trigger mode and the event time

Hexadecimal trigger time and mode flag (column 3, value 0f545714):

Bits	Value (decimal)	Description
First (top) 2 bits	0	0 is standard Level-2 trigger, >0 is hybrid
Next 10 bits	245	Second number since UTC midnight modulo 600
Last 20 bits	284436	Event second fraction (trigger micro-second)

Table 3.2: Description of the event header

Next, we describe the event waveform data which is recorded (the entire event readout is completed within 4 seconds) since the event header line. The beginning of a series of waveforms from any given counter (up to 10 waveforms per counter) is

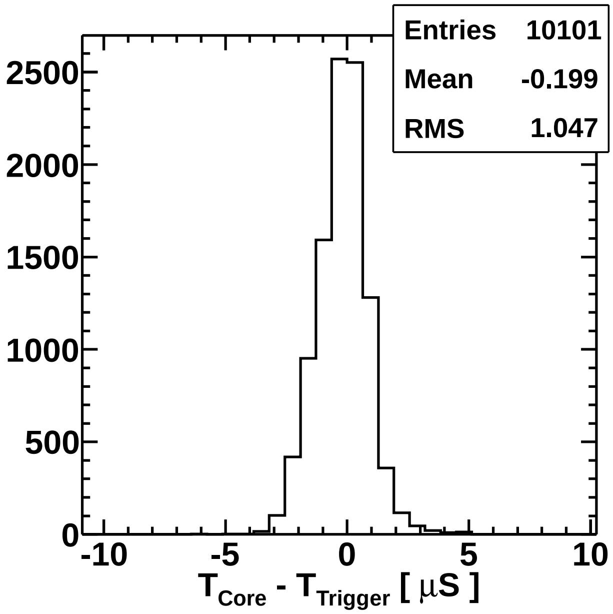

Figure 3.3: Difference between the core time and the trigger time reported by the TA SD data acquisition system. The RMS of the distribution is $\simeq 1$ μS. Only $\sim$0.5% of events are outside of this $\pm\,10$ μS window. Events with (reconstructed) zenith angle less than 45° were used.

denoted by a waveform header described in Table 3.3. The waveform data (signal in FADC counts, and time in integer clock counts) are recorded after the waveform header information. The waveform data begins with the (waveform) data header described in Table 3.4, which does not have reference to the counter because the counter has been provided in the waveform header information (Table 3.3). After the waveform data header, there are 132 lines of waveform information, described in Tables 3.5 and3.6 (using the excerpt from the raw data shown above as an example). The signal time with respect to the integer second (c.f. GPS-1PPS information, Table 3.1) is determined later in the analysis using the following variables:

Line in the data file: "W 1317 1"

Column #	Value	Description
1	W	Waveform header delimiter
2	1317	Counter position ID (c.f. Figure 3.1)
3	1	Numbers of waveforms received from the counter

Table 3.3: Description of the waveform header

Line in the data file: "w 0 0 132"

Column #	Value	Description
1	w	Waveform data header delimiter
2	0	Waveform number, for the integrity check, when multiple waveforms are being recorded
3	0	Number of re-tries in obtaining this waveform over the wireless radio (for monitoring purposes)
4	132	Number of lines (that follow) describing the waveform data

Table 3.4: Description of the waveform data header

- FADC time slice number, i, from 0 to 127 (Line #3, Table 3.5)

Line #	Value (hexadecimal)	Description
1	40d901fa	Top 3 bits are the trigger code, remaining 29 bits are the sub-clock count

Detailed description of line 1, value 40d901fa:

Bit # (from top)	Value (decimal)	Description
1	0	Software trigger, for troubleshooting purposes
2	1	Normal trigger (is set in this example)
3	0	Delayed trigger flag, for troubleshooting purposes
4-32	14221818	Sub-clock count at the beginning of the waveform

Waveform data description (continued):

Line #	Value (hexadecimal)	Description
2	02f6036e	Sums of signals (FADC counts) over 128 time slices (2.56 μS) for the upper (top 16 bits, 758 FADC counts) and lower (last 16 bits, 878 FADC counts) layers. Used mostly for the data integrity checks.
3	00005006	Signal (FADC counts) in the 1^{st} 20 nS time slice

Detailed description of line 3, value 00005006:

Bit # (from top)	Value (decimal)	Description
1-8	0	Time slice number, from 0 to 127 (software notation) (this means from 1 to 128 in human-readable form)
9-20	5	Signal in the time slice (FADC counts) for the lower layer
21-32	6	Signal in the time slice (FADC counts) for the upper layer

Table 3.5: Description of the waveform data, part 1.

Waveform data description (continued):

Line #	Value (hexadecimal)	Description
4	01005007	Signal (FADC counts) in the 2^{nd} 20 nS time slice
...	...	...
130	7f005007	Signal (FADC counts) in the 128^{th} 20 nS time slice
131	02faee56	Number of sub-clock counts in one second (decimal value is 49999446)
132	35102632	Information for troubleshooting purposes

Detailed description of line 132, value 35102632:

Bit # (from top)	Value (decimal)	Description
1-16	13584	Waveform pointer (in firmware) for troubleshooting
17-24	38	Noise (FADC counts, lower layer) in 8 FADC time slices (160 nS)
25-32	50	Noise (FADC counts, upper layer) in 8 FADC time slices (160 nS)

Table 3.6: Description of the waveform data, part 2.

- Sub-clock count at the beginning of the waveform, n, from 0 to 50×10^6 (Line #1, Table 3.5)
- Number of sub-clock counts in one second, N, typically $\sim 50 \times 10^6$ (Line #131, Table 3.6)

The second fraction of an i^{th} FADC time slice is then found from Equation 3.1:

$$t_i = \frac{n}{N} + (20 \times 10^{-9}) \times i \tag{3.1}$$

After the waveforms from all Level-0 counters within $\pm 32\,\mu$S of the event trigger time have been received, the event readout is finalized by a line

```
### DONE 925894 0f545714
```

This line contains two numbers: first number (925894) was initially used for troubleshooting purposes during the firmware development and is no longer useful. The second number (0f545714) corresponds to the event trigger and time information (same as Line #2, Table 3.2), which is used for the data integrity checks.

3.2.3 Monitoring Information

As discussed above (and in Chapter 2), the TA SD monitoring (calibration) cycle is 10 minutes long. The transfer time of the monitoring information is also 10 minutes. Every second of the 600 second transfer cycle represents a different monitoring data part from each counter. A monitoring cycle is recorded into the data stream in the following way:

```
...
#T 006b3ae3 111017 133000 5183 0 6
...
L 1301 a603 0 000 0 038 2faeffd 0 0 0 0
L 1302 2a5ca9 0 000 0 039 2faece7 0 0 0 0
L 1303 28eb39 0 000 0 041 2faeed7 0 0 0 0
....
#T 006b3ae4 111017 133001 5279 1 6
...
#T 006b3afb 111017 133024 5293 24 6
...
L 1301 a61b 0 024 0 032 2faeffd 64b 651 6fb 771
L 1302 2a5cc1 0 024 0 025 2faece7 535 4d1 500 4b2
L 1303 28eb51 0 024 0 040 2faeed6 747 7ed 90d a3e
...
#T 006b3d3a 111017 133959 5276 599 5
...
L 1301 a7ba 0 599 0 026 2faeffb 0 0 0 0
```

```
L 1302 2a5ea8 0 599 0 037 2faece7 0 0 0 0

L 1303 28ed48 0 599 0 047 2faeed8 0 0 0 0

...

#T 006b3d3b 111017 134000 5359 0 5

...
```

For every GPS second, explained in Table 3.1, all 170 counters (in BR-CT case) report their monitoring information (only 3 counters are shown in the above example). Each monitoring cycle begins at the *second number* (second since midnight modulo 600) of 0 and ends at the second number 599, producing a total of $170 \times 600 = 102000$ lines of monitoring information (in BR-CT case). Table 3.7 describes the format of the monitoring data received from each counter in one second. The last 4 lines (lines 9 - 12) of Table 3.7 are special variables, denoted by V_1, V_2, V_3, V_4, which correspond to different monitoring data parts depending on the second number. Variables $V_1 - V_4$ are described in Tables 3.8 and 3.9.

Line in the data file: "L 1301 a61b 0 024 0 032 2faeffd 64b 651 6fb 771"

Column #	Value	Description
1	L	Monitoring information delimiter
2	1301	(Decimal) counter position ID
3	a61b	(Hexadecimal) Wireless communication status flag
4	0	(Decimal) Wireless communication error flag
5	024	Second since midnight modulo 600 (second number) reported by the counter for data integrity checks
6	0	Number of triggered waveforms (not implemented yet)
7	032	Number of Level-1 triggers sent by the counter in one second
8	2faeffd	(Hexadecimal) number of counter sub-clock counts in 1 second
9	64b	(Hexadecimal) V_1 (depends on the second number)
10	651	(Hexadecimal) V_2 (depends on the second number)
11	6fb	(Hexadecimal) V_3 (depends on the second number)
12	771	(Hexadecimal) V_4 (depends on the second number)

Table 3.7: Monitoring data format

Second number	V_1, V_2, V_3, V_4
0	Channels 0 - 3 of the 1-MIP histogram (lower layer)
1	Channels 4 - 7 of the 1-MIP histogram (lower layer)
...	...
126	Channels 504 - 507 of the 1-MIP histogram (upper layer)
127	Channels 508 - 511 of the 1-MIP histogram (upper layer)
128 - 255	Channels 0 - 511 of the 1-MIP histogram (lower layer)
256 - 319	Channels 0 - 255 of the pedestal histogram (upper layer)
320 - 383	Channels 0 - 255 of the pedestal histogram (lower layer)
384 - 415	Channels 0 - 127 of the pulse height linearity histogram (upper layer)
416 - 447	Channels 0 - 127 of the pulse height linearity histogram (lower layer)
448 - 479	Channels 0 - 127 of the pulse charge linearity histogram (upper layer)
480 - 511	Channels 0 - 127 of the pulse charge linearity histogram (lower layer)

Table 3.8: Description of the monitoring histograms.

The most important information is the 1-MIP and pedestal histograms, discussed in Chapter 2 along with the SD electronics, because these histograms are needed for calibrating each surface detector using pulse heights of atmospheric particles. The remaining two monitoring histograms, described in Table 3.8, are the pulse height and pulse charge linearity histograms, used for monitoring purposes mainly. The pulse height linearity histogram is the distribution of the maximum pulse in a 20 nS FADC time slice in a waveform. The pulse charge linearity histogram is the distribution of waveform integrals (over 128 FADC time slices).

3.3 Calibration

The main objective of calibration is to determine the correspondence between the counter FADC reading and the energy deposition. This correspondence is

Second number	V_1, V_2, V_3, V_4
512	Charge controller readings in the 1^{st} minute of the monitoring cycle (part 1): V_1 - Battery voltage, V_2 - Blank, V_3 - Battery current, V_4 - Blank
513	Charge controller readings in the 1^{st} minute (part 2): V_1 - Reference voltage, V_2 - Battery temperature, V_3 - Solar panel voltage, V_4 - Charge controller temperature
514	Charge controller readings in the 2^{nd} minute (part 1)
515	Charge controller readings in the 2^{nd} minute (part 2)
...	...
530	Charge controller readings in the 10^{th} minute (part 1)
531	Charge controller readings in the 10^{th} minute (part 2)
532	Main board readings in the 1^{st} minute (part 1): V_1 - Ground voltage check, V_2 - Temperature (surrounding) V_3 - 5 V voltage check, V_4 - Humidity (surrounding)
533	Main board readings in the 1^{st} minute (part 2): V_1 - 3.3 V voltage check, V_2 - Main board temperature, V_3 - 1.8 V voltage check, V_4 - 1.2 V voltage check
...	...
550	Main board readings in the 10^{th} minute (part 1)
551	Main board readings in the 10^{th} minute (part 2)
552	Trigger rates for the 1^{st} and 2^{nd} minutes: V_1 - Number of Level-1 triggers in the 1^{st} minute, V_2 - Number of Level-0 triggers in the 1^{st} minute, V_3 - Number of Level-1 triggers in the 2^{nd} minute, V_4 - Number of Level-0 triggers in the 2^{nd} minute
...	...
556	Trigger rates for the 9^{th} and 10^{th} minutes
557	GPS status information for the counter: V_1 - UTC date, V_2 - UTC time, V_3 - GPS status flag, V_4 - Current Level-1 trigger rate
558-599	Temporary troubleshooting information. These fields can be used for additional monitoring information, when it becomes necessary.

Table 3.9: Description of the additional monitoring data.

a simple proportionality relationship [80], with a linearity range (typically up to 2000 FADC counts per 20 nS) determined prior to the deployment [82] and monitored since, using pulse height and pulse charge linearity histograms. This section describes the determination of the counter gain, in FADC counts per MeV (or VEM) using 1-MIP (and pedestal) histograms from the 10 minute monitoring cycles. Figure 3.4 shows the mean gain in FADC counts per VEM for each counter on a typical day (used November 11, 2009 in this example).

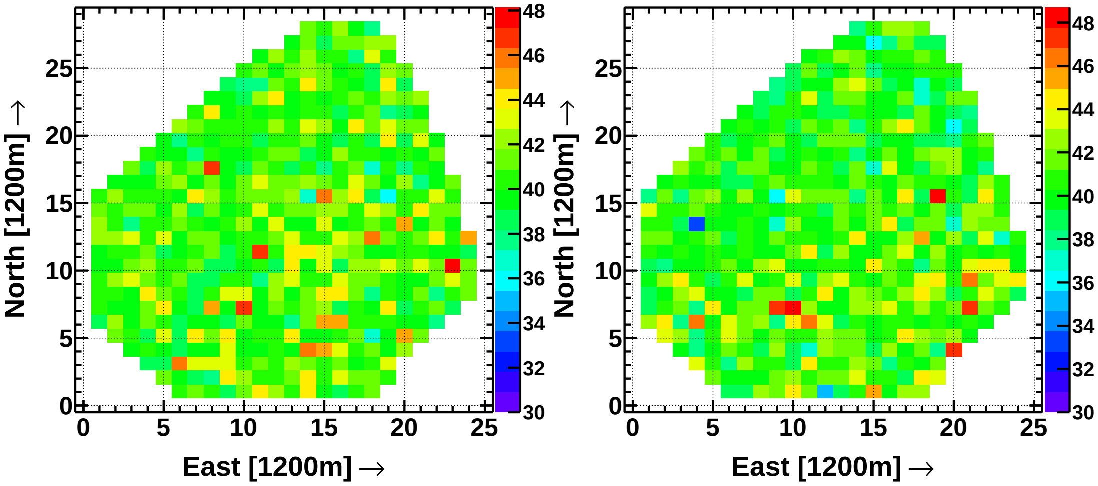

(a)

(b)

Figure 3.4: Mean gain in FADC counts per VEM, represented by color, over a typical day of data: (a) for the upper scintillator layers, (b) for the lower layers. The gain is plotted versus counter X-Y position.

3.3.1 1-MIP simulation

A direct way of determining the gain is by simulating the distribution of the atmospheric particles [83, 76] and determining the gain values which produce the same 1-MIP histograms as measured by the TA SD counters. Low energy cosmic rays (sampled from the power law spectrum) are simulated using CORSIKA [84, 56] and daughter particles reaching the TA SD level (1370 m above the sea level) are saved. This collection of simulated atmospheric particles is then passed through GEANT4 response simulation [76, 85] of the TA SD, and the net energy deposition histograms for the upper and lower scintillator layers are determined (Figure 3.5). The histograms in Figure 3.5 are made with large statistics and are independent of the detector electronics, which means these results can be reused in simulating the 1-MIP histograms of different TA SD counters. The 1-MIP simulation and fitting for a particular counter is done using the following procedure:

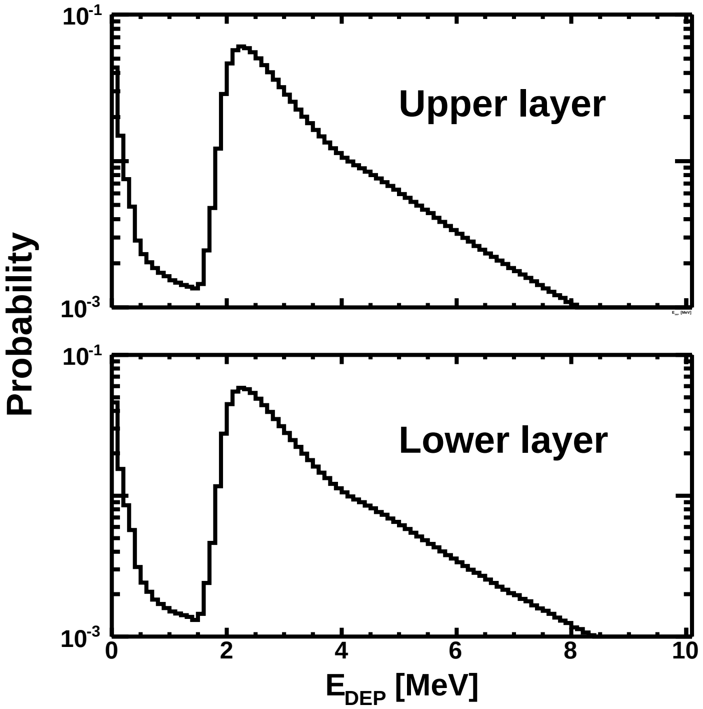

Figure 3.5: Energy deposition by atmospheric particles simulated using CORSIKA and GEANT4 simulation of the TA SD. The results are shown as (normalized) histograms of energy depositions in the upper and lower scintillator layers.

1. Assign the starting values for energy deposition to FADC count conversion factors (gains G_U, G_L for the upper and lower layers, respectively).

2. Sample the energy deposition from histograms in Figure 3.5 in the upper and lower layers.

3. Apply a measured 7% (Gaussian) non-uniformity smearing. This is the variation in the amount of light emitted and delivered to the PMTs, depending on where (in the scintillator) the energy deposition occurs.

4. Obtain the numbers of photo-electrons resulting from the energy depositions. For a typical typical counter, one has 10 photo-electrons per 1 MeV as the mean of the Poisson distribution (actual values were determined by a calibration prior to the deployment). Smear the numbers of photo-electrons according to the Poisson distribution and convert the results back to MeV.

5. Obtain the numbers of FADC counts using G_U, G_L and apply the Level-0 trigger condition, which means adding the pedestal (plus a small Gaussian noise due the RMS of the pedestal histogram) and requiring $\geq$15 FADC counts signal in coincidence between the upper and lower layers. If the Level-0 trigger condition is satisfied, then integrate the pulses over 120 nS and score the answers.

6. Repeat the above, starting from step 2, until sufficient statistics is obtained (in practice, same number of entries as in the actual 1-MIP histogram is sufficient).

7. Compare the simulated 1-MIP result with the real 1-MIP histogram using χ^2 comparison, scan through G_U, G_L values, repeating the above steps, until the χ^2 minimum is reached.

Figure 3.6 shows the fits of 1-MIP histograms for a typical TA SD counter. The result of this fit is $G_U = 18.2$ FADC counts /MeV (37.3 FADC counts /VEM) and $G_L = 17.4$ FADC counts /MeV (35.7 FADC counts /VEM).

This method is of general validity. The important contribution to the atmospheric particle distribution on the ground comes from the cosmic rays in 3 GeV

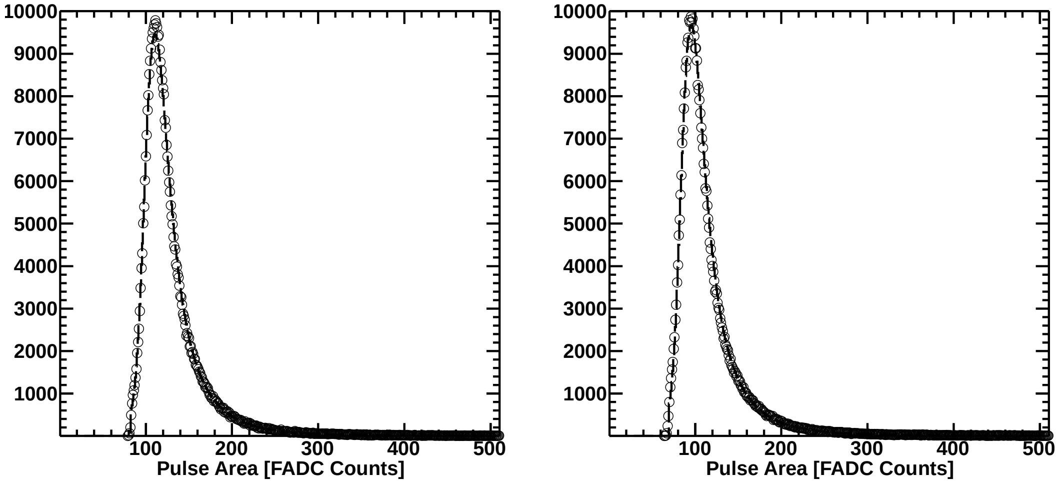

(a)

(b)

Figure 3.6: Fitting 1-MIP histograms to determine the detector gains in FADC counts / MeV (and also FADC counts/VEM): (a) is the upper layer and (b) is the lower layer. Circles represent the real 1-MIP histograms and curves represent the fitted values.

- 300 TeV range [83] due to their steeply falling spectrum and the detector sensitivity. Thus the systematic uncertainty due to the hadronic models is small. Also, this method uses an accurate simulation of the energy deposition into the scintillators by the atmospheric particles, while taking into account the response of the electronics of each individual counter. The overall accuracy of the method has been shown to be $\sim$ 1% [83].

3.3.2 1-MIP peak

Another calibration technique exists, which exploits the fact that there is a simple proportionality relationship between the location of the peak of the 1-MIP histogram (pedestal subtracted) and the detector gain. Furthermore, this relationship is independent of the details of the detector electronics on a $\sim$ 1.5% level, as Figure 3.7 shows. Since the 1-MIP peak represents the number of FADC counts due to the atmospheric minimum ionizing particles (mostly muons), the fact that

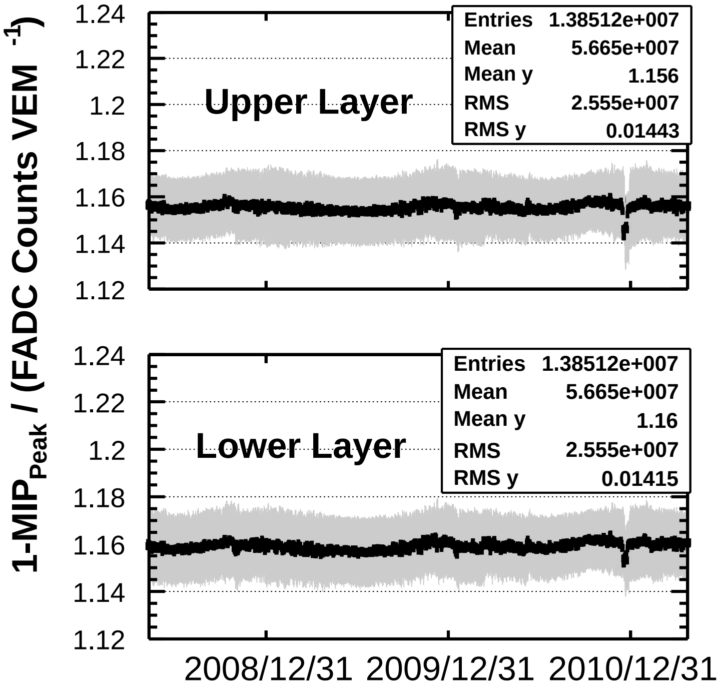

Figure 3.7: Ratio of the 1-MIP histogram peak location (pedestal subtracted), taken from the real data, and the FADC counts per VEM, obtained from the 1-MIP simulation procedure described above. The ratio is plotted for each day over 3 years of data . Black points represent the mean value for each day over all working counters in all events and the gray-shaded area represents the RMS (for each day). The RMS is better than 1.5 %.

this quantity is larger than the number of FADC counts in a VEM (vertical equivalent muon) by a factor of 1.16 can be simply interpreted as atmospheric muons coming at the most probable angle of $\sim 30^\circ$, so that their energy deposition scales roughly as the secant of this angle.

3.4 Pass0 Analysis

Two analysis programs exist for parsing the raw data and performing the calibration. One such program, called *rusdpass0*, has been developed at Rutgers University, NJ, USA and is a part of this work. Second program has been developed later, independently, by the TA collaborators at the Institute of Cosmic Ray Research, Kashiwa, Japan and includes more detailed calibration and monitoring information. The outputs of such programs, which we call *pass0* here, are the calibrated and time matched event data as well as the calibration information, written out separately. Calibrated event files are inputs for subsequent reconstruction programs, while the (separated) calibration information is used for generating Monte-Carlo (MC) simulations of the TA SD and writing simulated events in the same (calibrated event) format as the actual data. Both data and MC are then analyzed by the same reconstruction programs. Figure 3.8 shows the summary of these steps prior to the reconstruction. Details on the event reconstruction and MC generation are provided in the later chapters.

3.5 DST Data Format

The DST (Data Storage Tape) format is the official data format of the Telescope Array experiment. It is called so for historic reasons: in the 1990s, when High Resolution Fly's eye experiment started, the data was permanently stored on a magnetic tape. This format, however, after a few modest modifications, became suitable for storing the data on hard disks and has been found to satisfy the needs

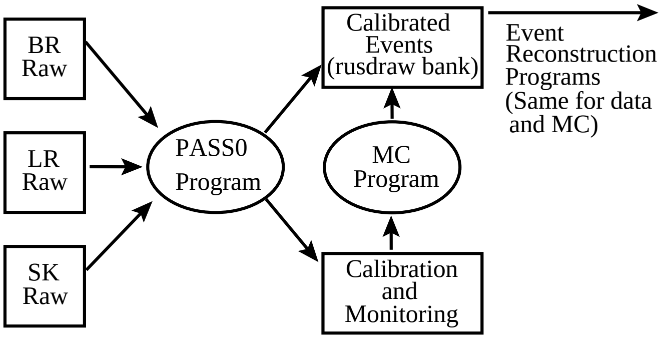
BR Raw
LR Raw
SK Raw
PASS0 Program
Calibrated Events (rusdraw bank)
MC Program
Calibration and Monitoring
Event Reconstruction Programs (Same for data and MC)

Figure 3.8: Summary of pass0 outputs which consist of two information pieces: calibrated events and (separately written) calibration and monitoring information. Separated calibration and monitoring are necessary for generating detailed Monte-Carlo simulations of the TA SD with the same characteristics (and format) as the actual data.

of the TA experiment.

Since the TA is a multinational and multicultural collaboration, a great variety of programming philosophies and analysis approaches exist within this groups, requiring the data format to be independent of programming languages, implementations, and platforms. Several general requirements of the format have been identified and are now satisfied by the DST system. First, it is stable over a 10 year time period: no major changes or updates to the format are currently projected. Second, the code system is supported by the common platforms, such as Linux/Unix, Mac OS, and Microsoft Windows. Third, the DST libraries have been devised for every major programming language, currently in use by most TA groups, which include C/C++, FORTRAN, Java, and Python. Fourth, no special administrative privileges are required to compile and execute the code, making it suitable for use in the environments of high performance computing. Finally, the DST system organizes the data into the event packets, with each event packet containing the structures of relevant data, called the *DST banks*. This allows physicists to seamlessly iterate over the events and use automatically filled structures of relevant information, which is a common analysis approach in the modern field of high energy physics.

We conclude this section by describing the calibrated SD event format (pass0, Figure 3.8). This is the output of both the *rusdpass0* parsing program for the data and the Monte-Carlo simulation of the TA SD. The DST bank which describes each event prior to the reconstruction is called *rusdraw.* The important variables of this bank are summarized in Table 3.10.

Variable	Description
event_num	Event number in the DST file
site	Flag representing the towers or combinations of towers which reported this event
run_id	Numbers labeling the raw data files for BR, LR, and SK
trig_id	Event trigger ID numbers for each tower
errcode	Event parsing error flag, 0 if no problems
yymmdd	UTC date
hhmmss	UTC time
usec	Event trigger micro second
nofwf	Number of waveforms recorded for this event

The following variables are available for each waveform:

Variable	Description
xxyy	Counter logical ID number
clkcnt	Sub-clock count at the beginning of the waveform
mclkcnt	Number of sub-clock counts in 1 second
fadc	Signal in FADC counts in the upper and lower layers, in all 128 (20 nS) time slices
mip	Peak channel of the 1-MIP histogram with pedestal subtracted

Table 3.10: Summary of the rusdraw bank.

Chapter 4

TA SD Monte Carlo

Measuring the cosmic ray flux over a wide range of energies requires an accurate determination of the detector efficiency and aperture, which often strongly depend on the event energy. Moreover, the air fluorescence detectors and ground arrays have a finite resolution that also evolves with energy. These effects must be understood and corrected for to extract meaningful results. In the case of the fluorescence detector, the aperture grows with energy because the high energy events produce more light in the atmosphere and can be seen further away from the detector, which increases the effective area of the detection. High energy events typically produce larger photon fluxes at the detectors, and therefore provide better signal-to-noise ratios and consequently, reconstruct with a better energy resolution. In the case of the ground array, there is a characteristic threshold energy above which the detector becomes fully efficient and the aperture becomes constant, since the surface detector is constrained by a fixed area on the ground. Below this threshold energy, the surface detector efficiency eventually reduces to zero with decreasing energy: low energy cosmic rays do not produce enough energetic secondary particles at the ground level that are spread on the distance scales comparable to the spacing of the surface detector counters. The high energy events, on the other hand, produce more daughter particles and thus yield larger energy depositions in the surface counters with smaller relative fluctuations, which leads to the improvements in the energy resolution, as will be demonstrated in the next chapter. As in the most high energy measurements involving complex instruments, the fluorescence and surface detector efficiencies, as well as the effects of the finite resolution, can be evaluated reliably only by detailed Monte-Carlo (MC) simulations.

The response to the atmospheric extensive air showers (EAS) induced by the primary cosmic rays of energies ranging from 10^{17} to $10^{20.5}$ eV so far has been evaluated accurately only for the fluorescence detectors (FD). The Monte-Carlo methods of simulating an FD were pioneered by the Fly's Eye [86] and HiRes-MIA [87] experiments, and later successfully implemented and tested by the HiRes collaboration [88]. By comparing the distributions of basic variables reconstructed in the same way for both data and the MC, the HiRes experiment effectively controlled the systematic uncertainties of the measurement and also demonstrated that the Monte-Carlo simulation made using the CORSIKA [56] QGSJET-II [46] proton model matched the cosmic ray data best [2]. The HiRes experiment evaluated its aperture by this technique and was first [11] to report the observation of the Graissen-Zatsepin-Kuz'min [30, 31] effect, which was later independently confirmed by the Pierre Auger Observatory [89], and the result of this work. For these reasons, the composition and the energy spectrum measured by the HiRes experiment are used in generating the TA surface detector Monte-Carlo, which is described later in the chapter.

This chapter describes an experimental technique that is new to the field. For the first time, a surface detector is successfully modeled by the CORSIKA Monte-Carlo in a detailed way for cosmic ray energies above 10^{17} eV. The same Monte-Carlo method is applied to the the Telescope Array surface detector as that used by the HiRes experiment for the air fluorescence detector case. At the same time, the long-standing technical difficulties of simulating the distributions of the secondary particles on the ground accurately [90, 91] by CORSIKA have been circumvented using a novel technique called *dethinning*, which will be briefly described below. The full description of the dethinning method and other relevant information can be found also in [15] and [92]. In the sections that follow, we describe the generation of the extensive air showers of 10^{17} to $10^{20.5}$ eV energies by CORSIKA [56], the GEANT4 [85, 76] simulation of the response of the TA surface detector to the secondary particles on the ground, and a full TA SD Monte-Carlo [84], including its validation by comparing the simulated distributions with those of the data. The work of this chapter is also expected to appear in the future publication [93] by the Telescope Array collaboration.

4.1 CORSIKA Simulation

4.1.1 Thinning Approximation

The computational resources required to generate large numbers of cosmic ray showers of $E > 10^{17}$ eV by CORSIKA (or equivalent programs like AIRES [58]) while tracking all secondary particles in the simulations are not available at the present time [92]. To reduce the demand for the computing power, a technique called *thinning* [94, 95] is commonly used by the air shower simulation codes. The approach consists of reducing the numbers of secondary particles being followed in the code by replacing them using representative particles that are assigned weights to account for the removed particles. A short description of the CORSIKA thinning approximation given here follows [91] and [95]. Let E_0 denote the energy of the primary cosmic ray that initiated the extensive air shower and let ϵ denote the *thinning level* parameter. Two cases are considered for every interaction within the shower. If $\sum\limits_j E_j < \epsilon E_0$ holds, where E_j are the energies of the secondary particles produced in the interaction, then the secondary particles are kept in the simulation with probability $p_i = E_i / \sum\limits_j E_j$. If $\sum\limits_j E_j \geq \epsilon E_0$, then the secondary particles of energies $E_i < \epsilon E_0$ are retained with probability $p_i = E_i / \min(\epsilon E_0, \sum\limits_{j,\ E_j < \epsilon E_0} E_j)$ (all particles with $E_i \geq \epsilon E_0$ are kept). In both cases, the selected secondary particles are assigned a weight of $w_i = w/p_i$, where w is the weight of the primary particle that started the interaction within the shower. The weights are normalized so that the weight of the primary cosmic ray particle equals unity. One can see that particles, rarely chosen to be retained due to their energies being small compared to ϵE_0, are assigned larger weights to account for the fact that many similar particles have been discarded. This algorithm also conserves the total energy: when the particle energies and all energy depositions into the surrounding materials are added (including the particle weights in the summation), then the weighted sum is equal to the energy of the primary particle that initiated the shower [94].

The thinning method yields satisfactory results for modeling the fluorescence detector [88] because the longitudinal (fluorescence light) profile measured by the FD is generated mainly by the shower core, a dense and narrow region around the shower axis that contains most of the secondary particles (with small relative fluctuations in their numbers) produced in the course of the EAS development. The main contribution to the statistical uncertainty in the energy determination by the FD (if the shower geometry is well constrained as in the HiRes stereo reconstruction [96]) is the Poisson fluctuation associated with sparse sampling of the photon flux by the fluorescence telescopes [97], not due to the fluctuations in the numbers of particles at the shower core.

The TA surface detector, in contrast, is measuring the lateral distributions of the shower (operating in the tail regions) and thus it is sensitive to the behavior at large distances (> 500 m) from the shower axis, where the density of the secondary particles is much lower than that at the core [90]. In the low (particle) density regime, the thinning procedure still reproduces correct average values of the kinematic variables [91, 98, 15] that can be expressed as weighted sums over all particles in the regions of interest. However, the approximation causes large artificial fluctuations in the numbers of particles and their arrival times and provides incorrect distributions of these quantities when compared with those of the non-thinned showers [15]. Figure 4.1a illustrates the problem. Because of this, simulations that use the thinning method alone are unfit for describing the surface detector.

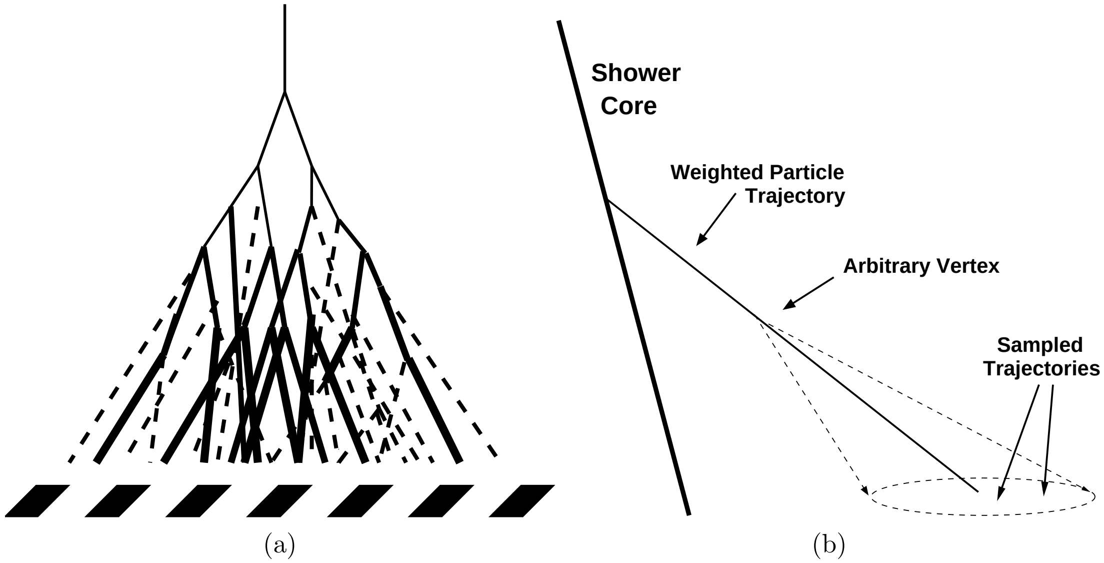

Figure 4.1: (a): Illustration of the problem caused by the thinning approximation in simulating the surface detector. Dotted lines represent the discarded particles (which would exist in a real shower) and the solid lines represent the weighted particles (thicker lines correspond to larger weights). The surface detector counters are represent by the filled polygons. (b): Illustration of the CORSIKA dethinning algorithm, adopted from [15].

4.1.2 Dethinning Method

Two methods of restoring the particle information on the ground after the thinning approximation have been developed independently by P. Billoir [98] and by B. T. Stokes [15, 84]. The methods are called "unthinning" and "dethinning", respectively. We briefly describe the later because the "dethinning" method is used in generating the CORSIKA Monte-Carlo of the TA surface detector. Also, the surface detector Monte-Carlo generated by this method has been successfully tested by comparing its distributions with the data, as will be shown later in this chapter.

This description of the dethinning method (applied to CORSIKA) closely follows [15] and [84]. First, one starts with an optimum thinning level, which has been shown to be $\epsilon = 10^{-6}$. This value of ϵ optimizes the use of computational resources while restricting the loss of information on the ground to an extent where the dethinning procedure reproduces the important properties of the original shower. Next, every weighted particle of weight w is smeared according to a Gaussian distribution (in angle) centered around its trajectory (Figure 4.1b), after choosing a point on the weighted particle trajectory (called the "Arbitrary Vertex" in Figure 4.1b). In the course of the procedure, $w-1$ particles of the same kind as the original weighted particle are sampled using this "Gaussian cone" and added to the original output of CORSIKA. The energies of the added particle are also sampled from a Gaussian distribution centered around the energy of the weighted particle to smooth their energy spectrum. While it is straightforward to assign the times of the sampled particles by approximating their velocities with that of the speed of light, there is an important causality constraint: the sampled particles should not be arriving at any point in space earlier than the light from the first point of interaction (point where the primary cosmic ray particle initiated the EAS) would.

The important parameters of the dethinning procedure are the width of the Gaussian cone used in sampling the trajectories, the width of the Gaussian used for smearing the energy distributions of the sampled particles, the minimum and maximum (lateral) distances for which the procedure applies, maximum height (above the ground) of the Gaussian cone, and the particle acceptance probability (for the sampled trajectories longer than that of the weighted particle). These parameters have been adjusted for the $\epsilon = 10^{-6}$ thinning case, so that the dethinned CORSIKA simulations accurately reproduce the non-thinned simulations. Figure 4.1b [84] shows the lateral distributions of the thinned ($\epsilon = 10^{-6}$) and dethinned shower simulations compared to the same shower simulated with no thinning. In all three cases, the CORSIKA showers have been passed through the detector response simulation, which will be described below. Additionally, [15] contains the comparisons of the the particle energy spectra, their number density, and their arrival time distributions (not including the detector response), between the dethinned and non-thinned showers. Those comparisons further demonstrate that the dethinning procedure correctly reproduces the essential properties of the non-thinned showers that are necessary for simulating the ground array detectors.

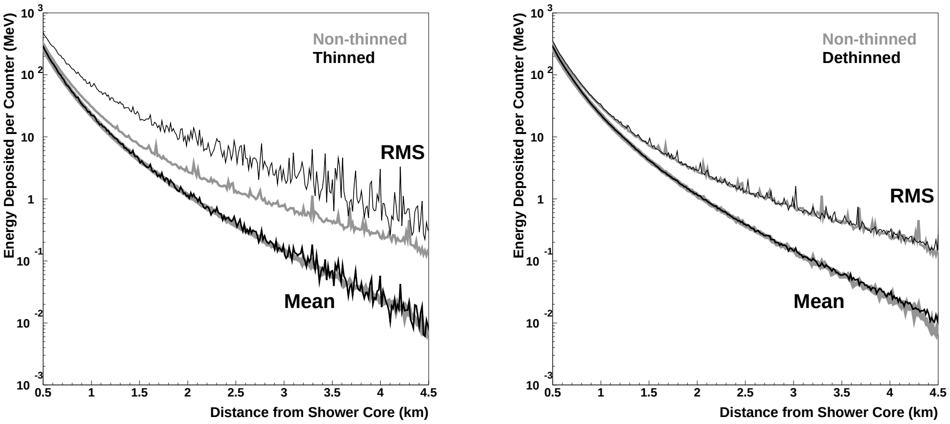

(a) (b)

Figure 4.2: Comparisons of the energy deposition in the TA SD counters (vertical axis) at varying distances from the shower axis (horizontal axis) for a 10^{19} eV proton shower with a zenith angle of 45°: (a) 10^{-6} thinned shower compared to the same non-thinned shower (b) dethinned shower compared to the same non-thinned shower. The comparisons demonstrate that the dethinning procedure correctly reproduces both the mean and the RMS of the energy deposition, while the thinning method alone reproduces only the mean values.

4.2 Detector Response

In the previous chapters, the TA SD electronics and the detector response to the minimum ionizing particles were described. Here, we provide the underlying details of the TA SD GEANT4 [78] simulation, which determines the energy deposition in the surface detector counters due to the secondary cosmic ray particles on the ground that are produced by (dethinned) CORSIKA showers. A description of the detector electronics simulation is included also.

4.2.1 Energy Deposition

The Telescope Array surface detector response simulation program [76] was originally developed by the TA collaborators K. Kobayashi, K. Miyata, S. Ogio, and N. Sakurai. The program, called *tasd*, uses GEANT4 [78] package and includes a detailed modeling of the TA surface detector unit geometry, parts, and corresponding materials; all have been described in detail in Chapter 2. The sensitive parts, which register the signal due to the secondary particles from the shower, are the upper and lower layers of the 2 m x 1.5 m x 1.2 cm plastic scintillator. For any given particle type, momentum, and trajectory, the simulation code provides the energy depositions in both scintillator layers.

In order to generate the CORSIKA Monte-Carlo events efficiently, including the response of the detector, it is advantageous to suitably parametrize the simulation of the energy deposition by the "tasd" program so that a large number of secondary particles can be simulated accurately in a short time. To this effect, a C-library package called "eloss_sdgeant" has been developed, which is a part of this work. It consists of a function that takes the CORSIKA particle ID and the momentum as arguments and provides the energy deposition in the upper and lower layers, which would be simulated by executing the "tasd" program. This library is easily integrated with the full surface detector Monte-Carlo (also written in C), and is capable of simulating the energy deposition distribution, in both scintillator layers, of $\sim 10^5$ particles of any energy in one second on a single 1 GHz CPU core, while using only $\sim$ 150 Mb of random access memory.

Figure 4.3 shows the detector and the beam arrangement used in generating the library of the TA SD response to the important secondary cosmic ray particles:

γ, $e^{\pm}$, $\mu^{\pm}$, p, n, and $\pi^{\pm}$. The library consists of a set of two-dimensional histograms of the energy deposition in the upper and lower scintillator layers for each particle type, energy, and (secant of) zenith angle θ, collected in the following way:

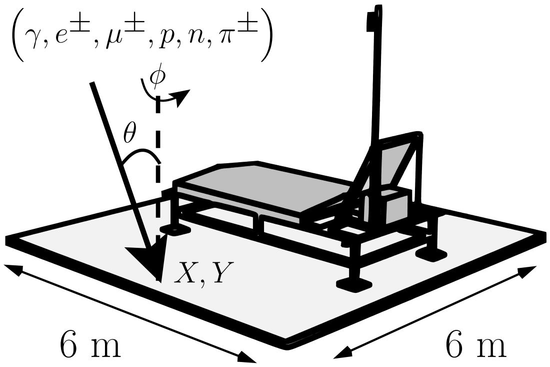

Figure 4.3: Illustration of the detector and the beam set-up used in generating the TA SD response library by the GEANT4-based program. X, Y are the randomly chosen coordinates inside the 6m x 6m square, θ is the (given) zenith angle of the particle, and ϕ is the randomly chosen azimuthal angle. Arrow represents the direction of the simulated particle.

1. Sample a random point X, Y on the ground inside the 6 m x 6 m square (Figure 4.3).

2. Sample a random azimuthal angle ϕ about the vertical axis.

3. Generate the particle trajectory in the θ, ϕ direction so that that the particle would pass through the X, Y point on the ground in the absence of interactions. Let the GEANT4 propagate the particle, including all possible interactions inside the detector unit and the materials surrounding it and score the resulting energy depositions (by the initial particle itself and/or the daughter particles) inside the upper and lower scintillators.

4. Repeat the above steps 1.2×10^{6} times.

The sampling area on the ground (6 m x 6 m) is made 12 times larger than that of each scintillator (1.5 m x 2 m) in order to include the edge effects (where the particles interact inside the detector frame), as well as the back-scattering effects, where the particles hit the ground near the detector and the resulting daughter particles penetrate into the scintillators. Figure 4.4 shows examples of the energy deposition histograms produced by this procedure, where only non-zero energy deposition cases are displayed, for simplicity. The cases where no energy deposition occurs in either scintillator or the energy deposition occurs only in one of the layers and not in the other are also included in the response library.

Figures 4.4a, 4.4b show examples of 1 GeV muons simulated using two zenith angles, 0° and 60°. The edge and back-scattering effects for 1 GeV muons are relatively small because these particles are penetrating: the muon minimum ionizing energy is in 300 MeV to $\sim$ 400 MeV range [47] for the most materials, and the energy loss increases only logarithmically with the particle energy. In both figures, there are strong peaks present (most probable energy deposition values). In the vertical case ($\sec(\theta) = 1.0$), the most probable energy deposition value is close to $\sim$2 MeV (in both layers), which was used for defining the vertical equivalent muon (VEM) unit of energy deposition (2.05 MeV) in Chapter 2. In the inclined case ($\sec(\theta) = 2.0$), the most probable value becomes $\sim$ 4 MeV, i.e. the energy deposition roughly scales as the secant of the zenith angle. In Figure 4.4b, there are also cases where the energy deposition is close to $\sim$ 4 MeV in one of the layers, while taking on a broad range of values in the other layer. The reason is geometrical: the inclined particles can pass through one of the layers while partially (or completely) missing the other layer.

Figures 4.4c and 4.4d illustrate the examples of 1 GeV γ particles. For the vertical case (Figure 4.4c), the most probable energy deposition is twice that of the vertical muon. The reason is that the γ particles pair-produce ($\gamma \rightarrow e^+ + e^-$), either in the roof of the detector or inside of the scintillator, and the ejected electron and positron pairs result in the energy deposition that is twice that of a single muon (the most probable value of a vertical $\sim$ 500 MeV electron or positron is also ~ 2 MeV in the TA SD scintillator). The feature in Figure 4.4c, where the lower layer has a roughly consistent energy deposition of ~ 4 MeV, while the upper layer has a broad range of values, corresponds to the cases where the pair production occurs in the upper scintillator and then e^{+}, e^{-} penetrate the lower scintillator. Both Figures 4.4c and 4.4d also show enhancements below 1 MeV, indicating that the edge and back-scattering effects are important in the case of γ particles, which have considerably shorter interaction length than that of minimum ionizing muons. The back-scattering effects are most prominent in the inclined ($\sec(\theta) = 2.0$) γ case, as Figure 4.4d shows.

The above examples of two-dimensional energy deposition histograms are just a few of the many. Such histograms have been generated for γ, $e^{\pm}$, $\mu^{\pm}$, p, n, and $\pi^{\pm}$ particles, for each energy and $\sec(\theta)$ slice. For γ particle, 63 slices in $\log_{10}E$ were used, starting at $\log_{10}(E_{\mathrm{MIN}}/\mathrm{eV}) = 4.7$ and ending at $\log_{10}(E_{\mathrm{MAX}}/\mathrm{eV}) = 11$. For $e^{\pm}$, $\mu^{\pm}$, p, and n, 50 energy slices were used, with $\log_{10}(E_{\mathrm{MIN}}/\mathrm{eV}) = 6.0$ and $\log_{10}(E_{\mathrm{MAX}}/\mathrm{eV}) = 11.0$. For $\pi^{\pm}$ particles, 49 energy slices were used, with $\log_{10}(E_{\mathrm{MIN}}/\mathrm{eV}) = 6.0$ and $\log_{10}(E_{\mathrm{MAX}}/\mathrm{eV}) = 10.9$. In all cases, 7 slices in $\sec(\theta)$ were used: $\sec(\theta) = 1, 1.5, 2.0, 2.5, 3.0, 3.5, 4.0$. These choices of binning in energy and angle were dictated by the physics of the extensive air showers (EAS) as well as the available computational resources. For example, the minimum energy included in the library for γ particles is lower than that of the rest of the particles because the low energy γ are ~ 10 times more numerous than the rest of the particles in a typical EAS and make a non-negligible contribution to the counter signal ($\sim 5\%$ due to γ particles of $E < 1$ MeV). The rest of the particles do not make a significant contribution to the signal when their energies are below 1 MeV. The particles of very high energies ($\log_{10}(E/\mathrm{eV}) > 11$) or large zenith angle ($\sec(\theta) > 4$), on the other hand, rarely reach the ground level without interacting in the atmosphere.

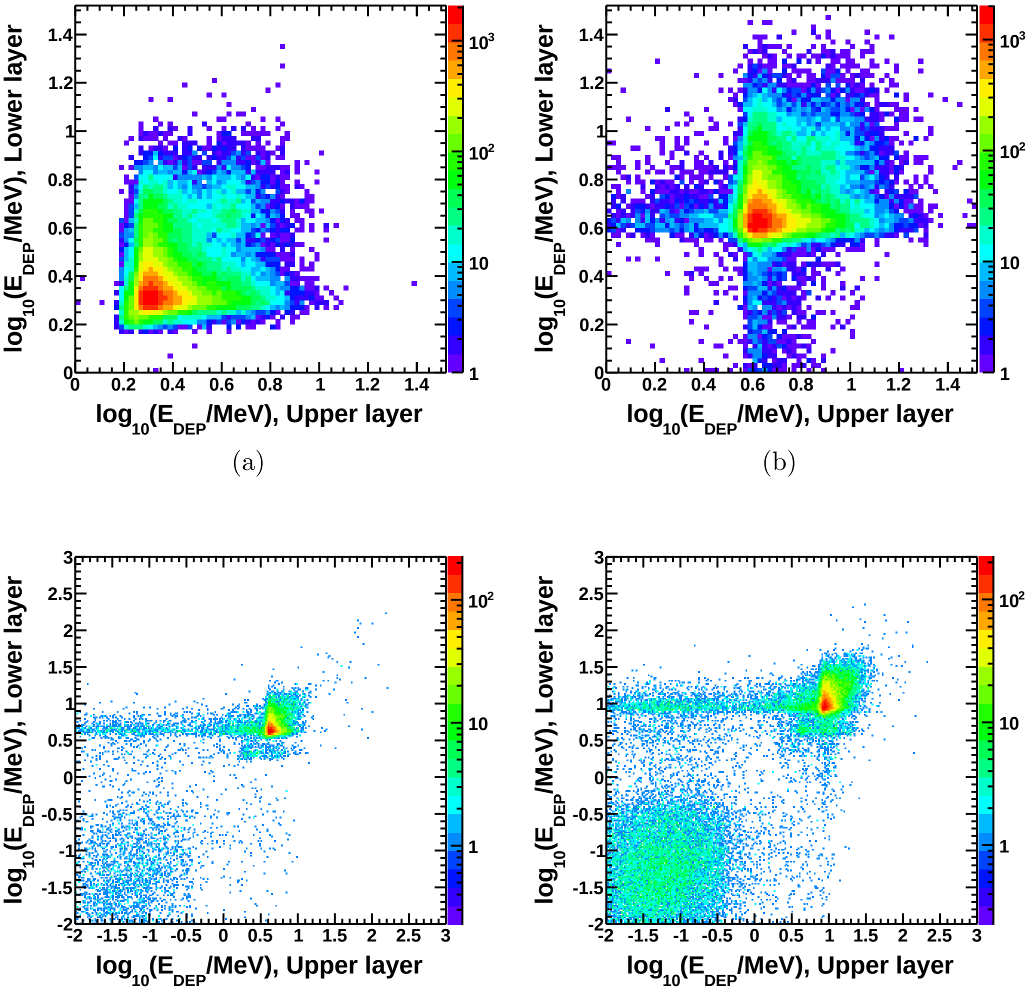

(a) (b)

(c) (d)

Figure 4.4: Examples of the energy deposition histograms used in preparing the TA SD response library. X-axis is the energy deposition occurring in the upper layer, Y-axis is the energy deposition in the lower layer, and the Z-axis (represented by colors) is the frequency. The examples use 1 GeV μ^+ and 1 GeV γ: (a): μ^+ at $\sec(\theta) = 1.0$, (b): μ^+ at $\sec(\theta) = 2.0$, (c): γ at $\sec(\theta) = 1.0$, (d): γ at $\sec(\theta) = 2.0$.

When the response library is used within the full detector Monte-Carlo, a special sampling routine obtains the particle type, energy, and $\sec(\theta)$ as arguments, and finds the closest energy and $\sec(\theta)$ values, for which the two-dimensional histograms are available within the response library. The energy depositions of the upper and lower scintillators are then sampled from these two-dimensional histograms, including the cases of no energy deposition at all and energy deposition in only one of the layers. Although the response library has maximum limits on the particle energy and zenith angle, in rare cases, when the particles of $\log_{10}(E/\mathrm{eV}) > 11$ or $\sec(\theta) > 4$ do reach the ground, correct energy depositions are obtained by extrapolating the library results of the boundary cases of $\log_{10}(E/\mathrm{eV}) = 11$ and/or $\sec(\theta) = 4$. Likewise, for intermediate energies and angles, the adjacent $\log_{10}(E/\mathrm{eV})$, $\sec(\theta)$ library results (two-dimensional histograms) are used, and the sampled energy deposition values are interpolated to yield the answers that are appropriate for the actual $\log_{10}(E/\mathrm{eV})$, $\sec(\theta)$ values. Figure 4.5 shows the comparison of the energy deposition distributions produced by the TA SD response library and the "tasd" (exact simulation) program. The comparison was made for two particles, γ (Figure 4.5a) and μ^+ (Figure 4.5b), of 5 GeV ($\log_{10}(E/\mathrm{eV}) \approx 9.7$) and $\theta = 40^\circ$ ($\sec(\theta) \approx 1.3$) each. The energy and angle were chosen so that they do not match any of the available library values and thus the sampling routine had to interpolate to get these answers: the closest values, for which the library histograms are available in this case are $10^{19.65}$ and $10^{19.75}$ eV in energy and 1.0 and 1.5 in $\sec(\theta)$. A good agreement in such comparisons means that the detector response library correctly reproduces the results of the "tasd" program and thus it can be used in the full Monte-Carlo simulation of the TA SD.

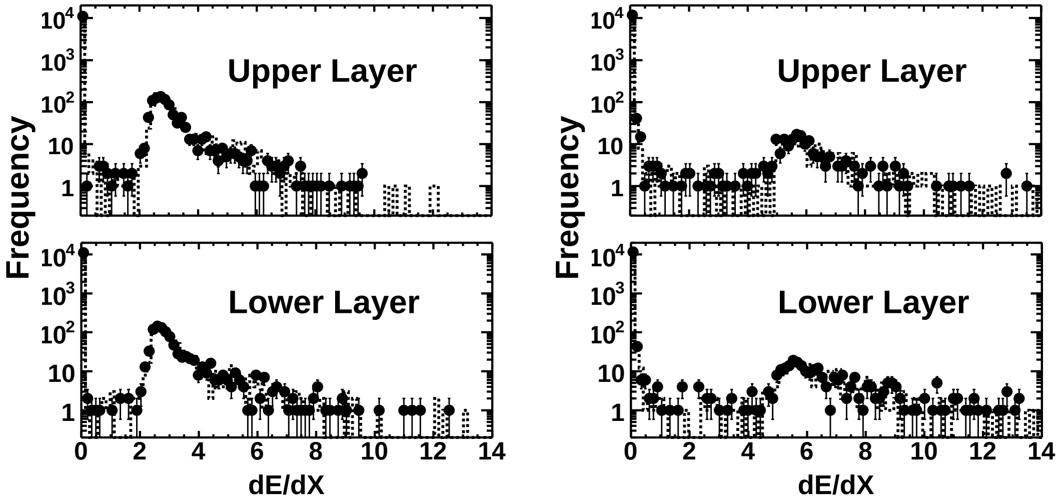

(a) (b)

Figure 4.5: Comparison of the energy deposition dE/dX distributions in the scintillators produced by the response library (black points) and the exact simulation program (dotted lines). The comparisons are made for two particles: (a): 5 GeV γ of $\theta = 40°$ (b): 5 GeV μ^+ of $\theta = 40°$. Large spikes at $dE/dX = 0$ (accurately reproduced by the response library) correspond to the cases where the particles miss the detector: the area of each scintillator is 1.5 m x 2.0 m, and the area of the sampling square is 6 m x 6 m. The edge and back-scattering effects (especially in the case of γ) near $dE/dX = 0$ are also reproduced correctly by the response library.

4.2.2 Electronics

The next major step after obtaining the energy deposition in the scintillators is to determine the signal read out by the detectors, as in the case of the real data. At this stage of the simulation, the energy deposition as a function of time is available for each counter, in both scintillator layers. Since the TA SD uses a 50 MHz FADC system, the signal is binned using 20 nS time slices.

First, the non-uniformity effects, the Poisson fluctuation of the number of photoelectrons at the PMTs, and Gaussian fluctuations of the pedestals are simulated (c.f. Section 3.3.1), and the result is converted to the FADC counts. In this process, real-time calibration constants are used, which are available for every 10 minute period of the detector on-time. Next, the signal in FADC counts, S_i, versus time (20 nS time slices are labeled by the index i) is convolved with the measured electronics response shape, R_i (Figure 4.6), to determine the signal $\tilde{S}_i$ as it would be reported by the FADC system of the counter: $\tilde{S}_i = \sum_{j=0}^{i} S_{i-j}\, R_j$ (for the upper and lower layers). The final step consists of applying the same

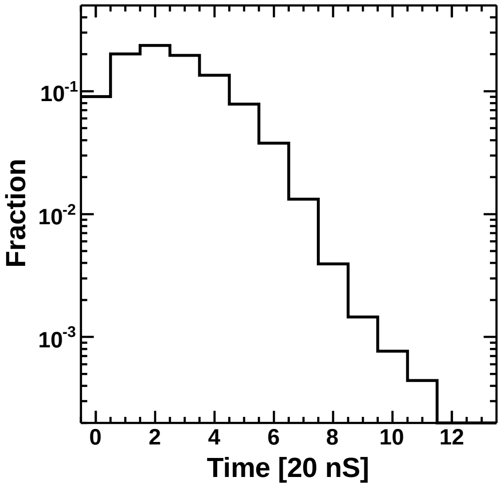

Figure 4.6: Response shape to a minimum ionizing particle for a typical TA SD counter.

trigger and data acquisition algorithms as those used in the real data, which were covered in detail in Chapters 2 and 3, and recording the simulated event using the same format as that of the data (“rusdraw” DST bank, c.f. Chapter 3).

4.3 Full Monte-Carlo

This section describes the simulation of the TA SD data as it exists in nature. The corresponding techniques, originally developed by the HiRes experiment [88], were adopted for the TA surface detector by B. T. Stokes. First, the TA SD *shower library* is introduced, which consists of sets of simulated CORSIKA showers, binned appropriately in zenith angle and energy so that the showers can be re-used in generating much larger Monte-Carlo sets. Then, the generation of a Monte-Carlo set that includes all known characteristics of the real cosmic ray data, called the *spectral set*, is described. The discussion below follows [84], and a more detailed description is expected to appear in [93].

4.3.1 Shower Library

Current TA SD shower library includes 16,800 CORSIKA [56] proton showers, simulated with $\epsilon = 10^{-6}$ thinning with the information on the ground restored using the dethinning procedure [15]. CORSIKA program was configured to use QGSJET-II [46] hadronic model at the highest energies, FLUKA [59] for hadronic interactions at low energies, and EGS4 [48] for simulating the electromagnetic component. The library is prepared using 38 bins in primary particle energy, starting with $\log_{10}(E_{\mathrm{MIN}}/\mathrm{eV}) = 16.75$ and ending at $\log_{10}(E_{\mathrm{MAX}}/\mathrm{eV}) = 20.55$. The numbers of library events per (logarithmic) energy bin range from 1000 (low energies) to 250 (high energies). Since the real (differential) cosmic ray flux is approximately a power law of the form E^{-3}, the low energy events are more numerous and therefore must be represented with more statistics within the library.

Also, the numbers of highest energy events are constrained by the computational power requirements, which are significant even in the case of $\epsilon = 10^{-6}$ thinning in CORSIKA. The zenith angle of the library showers is isotropically distributed in $[0, 60°]$ range.

For each shower in the library, the ground (desert floor) is binned using 6 m x 6 m tiles. The energy deposition of all secondary particles (in upper and lower layers) as function of time is saved using 20 nS time slices for each tile up to 7 km from the shower impact point. The details of the detector electronics and calibration are not used yet, only the energy deposition have been evaluated, as if each 6 m x 6 m tile contained a TA-type surface detector in the middle.

4.3.2 Spectral Set

The first step consists of sampling each of the 16,800 shower library events thousands of times (depending on the desired statistics) with randomly assigned time, impact position, and azimuthal angle. In the process, actual configuration of the TA SD array is used and the detector electronics is simulated, as described above. Random atmospheric muon flux is included also. The result is a large set of simulated events, recorded in the same format as the data, with an additional DST bank (see Chapter 3) called "rusdmc" (summarized in Table 4.1), which stores the true event information and which is used *after* the event reconstruction for determining the detector resolution and efficiency. The large event list, called the *event library*, is then used for generating Monte-Carlo, with cosmic ray energies sampled from the desired distributions. The final step consists of sparse sampling of the events from the library so that the (true) energies follow the energy flux shape measured by HiRes [11] experiment.

Table 4.2 and Figure 4.7 summarize the generated cosmic ray parameters and their distributions used in the Monte-Carlo spectral sets. It should be noted that the generated energy distribution in Figure 4.7a has been displayed in a

Variable	Description
event_num	MC Event ID
parttype	Type of the particle that initiated the shower
corecounter	Position ID (c.f. Chapter 3) of the counter closest to the shower impact point
tc	Time of the shower impact
energy	Particle energy
height	Height of the first interaction
theta	Particle zenith angle
phi	Particle azimuthal angle
corexyz	Position of the shower impact point (CLF frame, c.f. Chapter 3)

Table 4.1: Summary of the rusdmc bank.

different format than the rest of the quantities in Figure 4.7 (shown as histograms). The differential energy flux is a steeply falling power law: roughly, $dN/dE \propto E^{-3}$, which means that the energy histogram (using logarithmic bins) falls like $N \propto E^{-2}$. To make the changes in the spectral indices clearly visible, the generated energy histogram has been modified for the display: bin content of each logarithmic bin was divided by the bin size and multiplied by E^3. The result of the Figure 4.7a has also been normalized so that the first non-zero bin is unity. The solid line in the figure shows the broken power law spectrum function determined by HiRes, multiplied by E^3. The choices of limits on generated values of E and θ are adequate because only events with reconstructed $\theta < 45^\circ$ and $E > 10^{18}$ eV will be used in calculating the results. The Monte-Carlo simulation range is made wider than that of the reconstruction to model the edge effects, so that events with poor resolution can be studied and excluded from the data and MC samples by applying a suitably chosen set of cuts to both.

Parameter	Method of sampling
Composition	Pure proton [2]
Energy, E	HiRes broken power law function [11], Figure 4.7a: $E^{-3.25}, \quad E < 10^{18.65}\,\mathrm{eV}$ $E^{-2.81}, \quad 10^{18.65}\,\mathrm{eV} \leq E < 10^{18.75}\,\mathrm{eV}$ $E^{-5.1}, \quad E \geq 10^{19.75}\,\mathrm{eV}$
Zenith angle, θ	$\sin(\theta)\cos(\theta)$ distribution in $[0, 60°]$ range, Figure 4.7b
Azimuthal angle	Flat distribution in $[0, 360°]$ range, Figure 4.7c
Impact position	Randomly distributed inside a circle of 25 km radius centered at the CLF (c.f. Chapter 3), Figure 4.7d

Table 4.2: Cosmic ray parameters generated in the TA SD Monte-Carlo.

4.4 Validating the Monte-Carlo

The accuracy of the TA SD Monte-Carlo is most readily verified by comparing its reconstruction results with the data, after the MC is processed using the same analysis tools as the data. Below, we provide the data and MC comparison plots of the fitting residuals, as well as the distributions of reconstructed variables that are related to the shower geometry and the lateral distribution. A complete description of the event reconstruction techniques will be given in Chapter 5.

Fit residual is a useful quantity for testing whether the Monte-Carlo fits the same way as data. The normalized time fit residual for an i^{th} counter in the event is defined as:

$$\Delta_i/\sigma_i = \frac{t_i - t_i^{FIT}}{\sigma_i}, \tag{4.1}$$

where t_i is the time of the i^{th} counter, t_i^{FIT} is the time given by the fit function, and σ_i is the (time) uncertainty. Likewise, the normalized residual of the lateral distribution fit is defined:

$$\Delta_i/\sigma_i = \frac{\rho_i - \rho_i^{FIT}}{\sigma_i}, \tag{4.2}$$

where ρ_i is the pulse height of the i^{th} counter, ρ_i^{FIT} is the fit value, and σ_i is now the uncertainty of the pulse height.

Figure 4.8 shows the comparison of the time and lateral distribution fit residuals between the data and the MC, which indicate that the description of the shower front structure by the CORSIKA QGSJET-II Monte-Carlo closely resembles the real data. Also, Figure 4.9 shows a good agreement between the data and MC in variables that describe the quality of the fits, which means that the MC fits in the same way as the data. Therefore, this MC can provide reliable estimates of the detector resolution, which will be evaluated and quoted in the next chapter.

Finally, Figures 4.10 and 4.11 show a comparison between the data and the MC of the distributions of the geometrical variables, and the variables related to the lateral profiles of the showers. Detailed descriptions of these quantities and the underlying fitting procedures will be provided in the next chapter. A good agreement in this variables means that the MC can be used for calculating the aperture, which will be needed for unfolding the energy spectrum in Chapter 6.

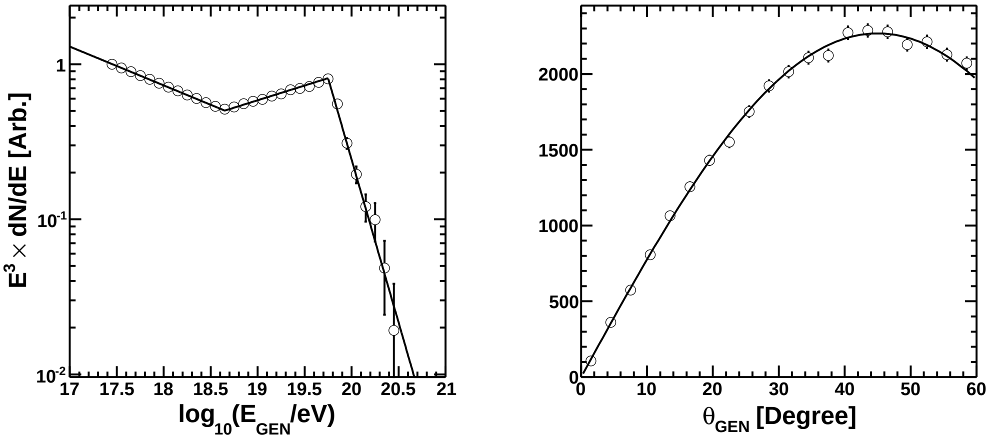

(a) Energy flux (normalized).

(b) Zenith angle.

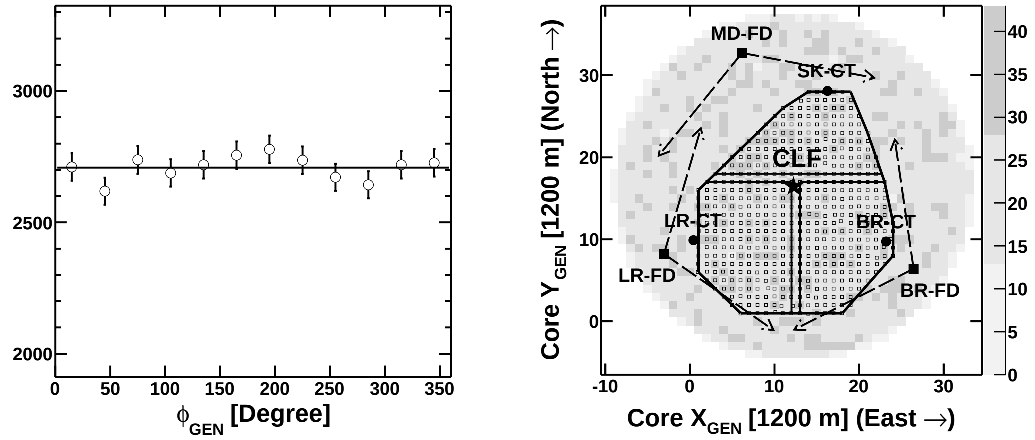

(c) Azimuthal angle.

(d) Position of the shower impact.

Figure 4.7: Distributions of generated shower parameters in the TA SD Monte-Carlo. In (a)-(c), points represent the samples and the solid lines correspond to the theoretical distributions from which the samples were drawn. A detailed description of the plots is provided in the text and in Table 4.2.

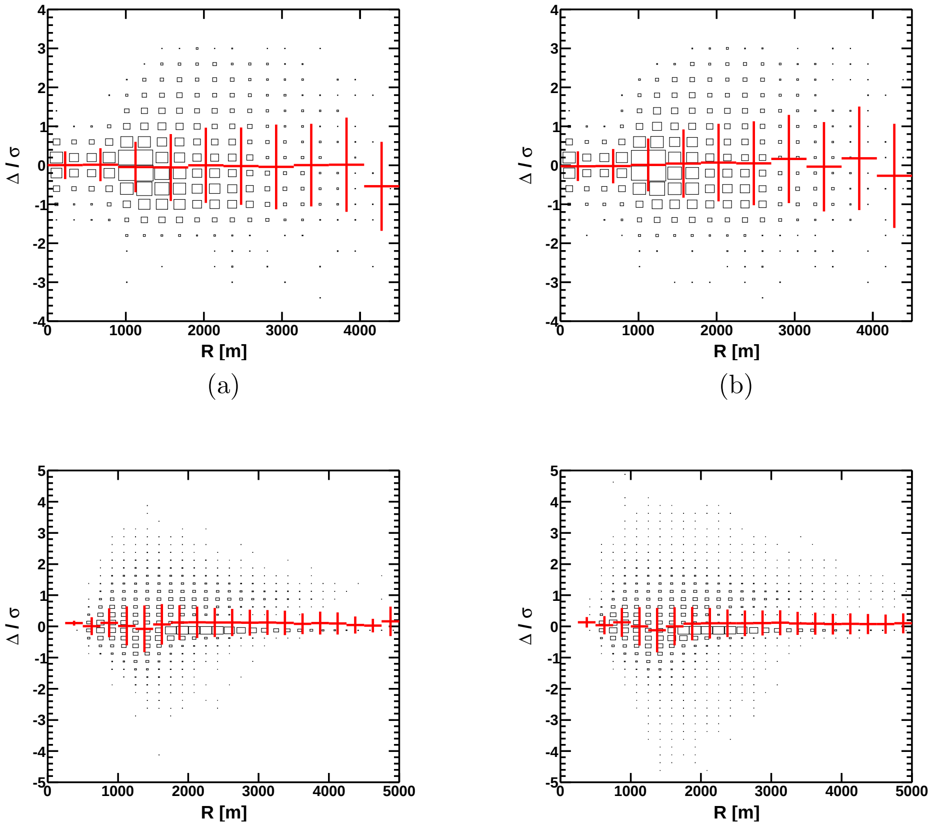

(a) (b)

(c) (d)

Figure 4.8: Comparison of the normalized fit residuals between the data and Monte-Carlo, where the residuals Δ/σ are plotted versus the counter distance from the shower axis R. Each entry represents a counter. The results are accumulated over all events in the data and MC sets. Points with error bars are the profile plots superimposed on top of the two-dimensional histograms. The profile points and error bars correspond to the mean and the RMS in each R slice, respectively. (a): Normalized time fit residuals of the data (Equation 4.1). (b): Normalized time fit residuals of the MC. (c): Normalized lateral distribution fit residuals of the data (Equation 4.2). (d): Normalized lateral distribution fit residuals of the MC.

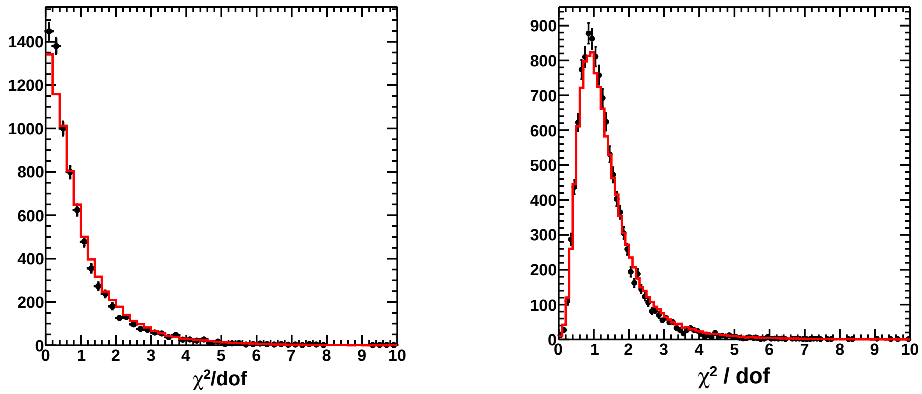

(a) χ^2/dof of the geometry fit.

(b) χ^2/dof of the lateral distribution fit.

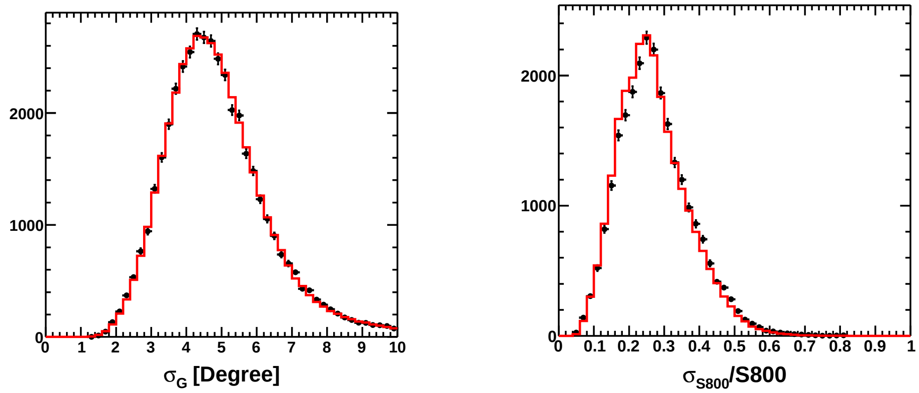

(c) Fit uncertainty of the event arrival direction.

(d) Fractional uncertainty on (fitted) signal size 800 m from the shower axis.

Figure 4.9: Data and Monte-Carlo comparison of the variables that describe the quality of the fits that determine the shower geometry and energy. Points with error bars are the data and solid lines are the MC histograms. The Monte-Carlo histograms have been normalized to have the same integrals (area) as the data. These variables are described in detail in Chapter 5.

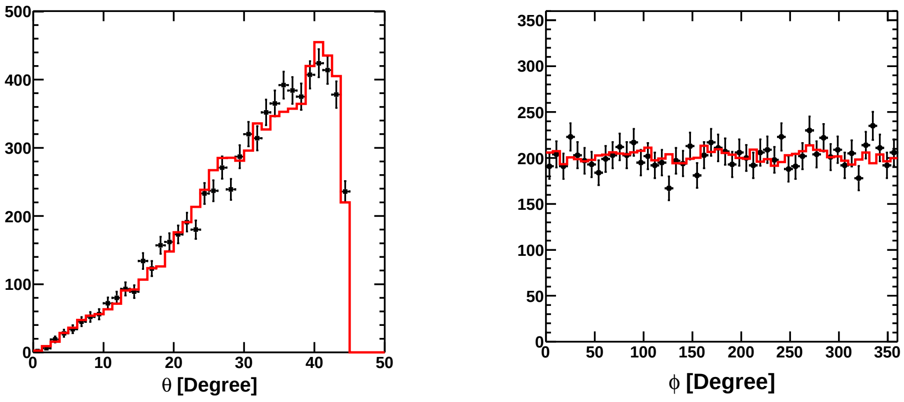

(a) Zenith angle. (b) Azimuthal angle.

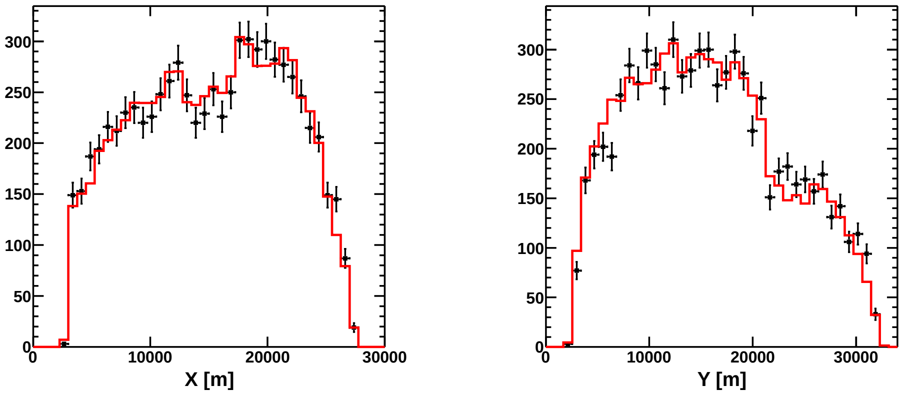

(c) East component of the shower impact. (d) North component of the shower impact.

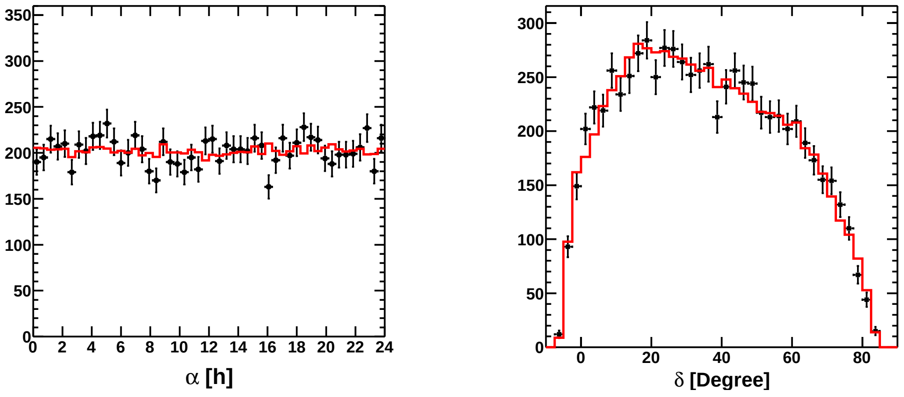

(e) Right ascension. (f) Declination.

Figure 4.10: Comparison of the data and Monte-Carlo histograms of the quantities related to the reconstruction of the shower geometry. Points with error bars represent the data and the solid lines correspond to the MC. The MC histograms are normalized to the data by area.

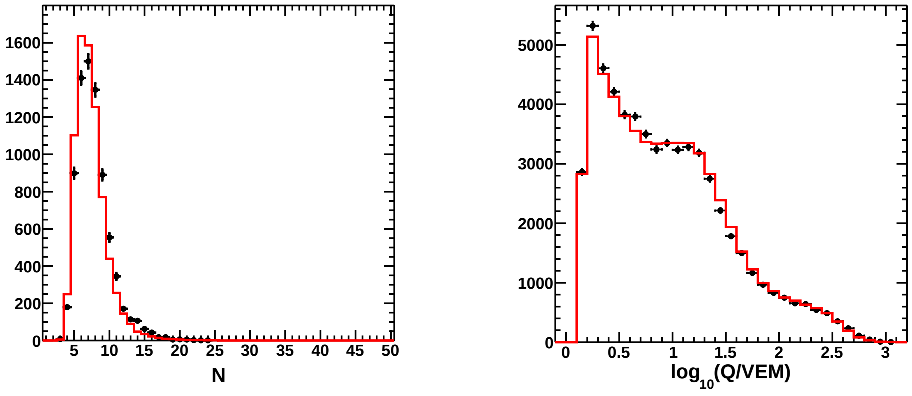

(a) Number of counters.

(b) Signal per counter.

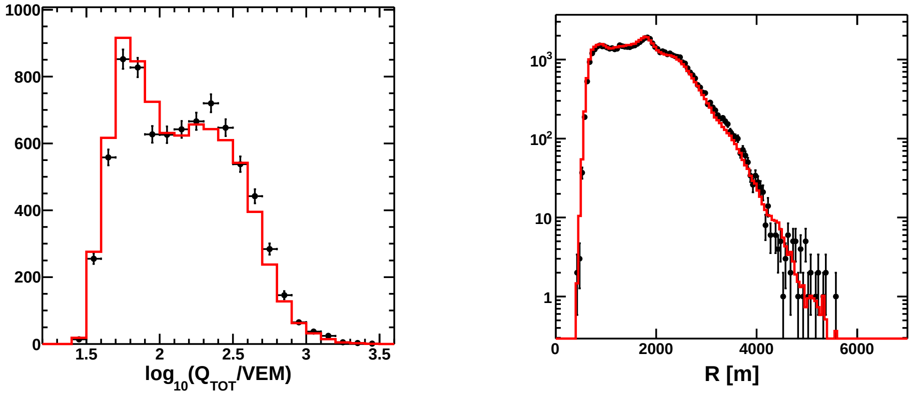

(c) Signal per event.

(d) Counter distance from the shower axis.

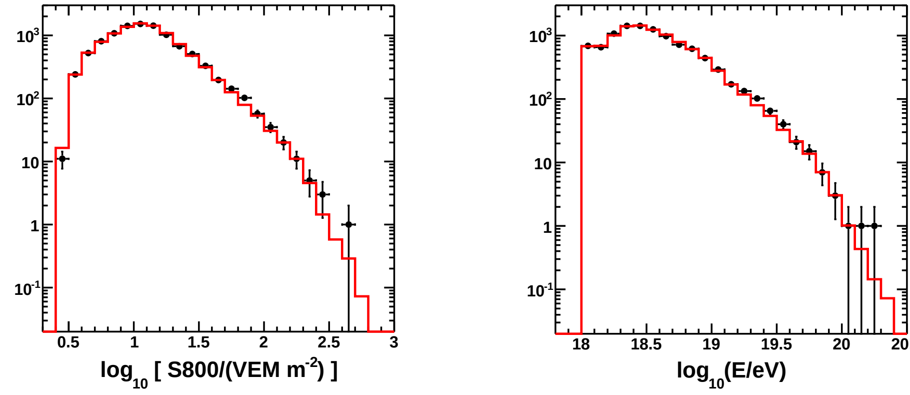

(e) Signal size 800 m from the shower axis.

(f) Energy.

Figure 4.11: Data and MC comparison of the lateral distribution quantities. Points with error bars represent the data and the solid lines are the MC histograms normalized to the same area as the data.

Chapter 5

TA SD Event Reconstruction

The surface detector event reconstruction is typically done in two major steps, which will be referred to as *pass1* and *pass2*. First, the event geometry is determined using the time of the arrival of the shower front particles measured by counters that triggered in the course of the event. Second, the pulse heights in these counters, along with the event geometry information, are used for determining the shower lateral distribution profile. Knowledge of the lateral distribution and the event geometry are sufficient for determining the event energy: event energy at a fixed zenith angle turns out to be proportional to the signal size at certain characteristic lateral distance from the shower axis. For a fixed energy, on the other hand, the signal size is attenuated with increasing secant of the zenith angle.

The basic TA SD event reconstruction, not including the event energy, is done in a model-independent way. The time delay and the lateral distribution functions have been determined by starting from the formulas used in the AGASA experiment [16, 99] and adjusting them to fit the TA SD data, until a self-consistency in the fitting results was achieved. Then a carefully tested Monte-Carlo set is used for determining the first estimate of the event energy from the geometry and the lateral distribution information. Finally, the event energy is calibrated to the fluorescence detector using the events seen in common by the TA SD and the TA FD (hybrid events). The details of these procedures will be described in the sections that follow.

5.1 Signal Selection and Pattern Recognition

The event reconstruction begins with determining the signal in each counter that comes from the shower. Figure 5.1 illustrates the signal selection process. An 80 nS sliding window (4 FADC time slices) is used for scanning the FADC traces (digitized signal versus time) of all waveforms in each counter. A 20 nS time slice, starting at which the digitized signal exceeds the pedestal by 5 σ (σ is the RMS of the pedestal per 20 nS time slice) in all 4 time slices of the sliding window, in upper and lower layers, represents the time of the signal (also called the *leading edge of the pulse*). The time slice where the signal is no longer greater than 5 σ above the pedestal, in all 4 time slices, is considered the signal end. This separation of the waveforms into the multiple (separable) pulses is a temporary measure, which is useful for identifying and excluding the signals from the random atmospheric muons, which occur at a rate of 700 Hz $\times$ 2 $\times$ 32 μS $\simeq$ 5% per counter during the event readout (which occurs over a ± 32 μS time window, as described in Chapter 3). While the random muon contribution is typically a small fraction of the counter integrated signal, a random muon signal occurring before the shower signal (Figure 5.1b) can lead to inaccuracies in the determination of the shower front time (which uses the leading edge of the pulse). An algorithm scans the signals in the counters for such occurrences and removes the early muons, if found. Lastly, all pulses (pulse areas) within 10 μS of the leading edge of the earliest pulse (that is a part of the shower) are summed. The end result of the signal processing procedure is that for every counter, there is one pulse height value in VEM units, averaged over the upper and lower layers and one time, which is the leading edge of the first pulse. The counter pulse height is calculated by integrating the FADC signals, subtracting the pedestal, and expressing the answer in VEM using the calibration constants (c.f. Chapter 3).

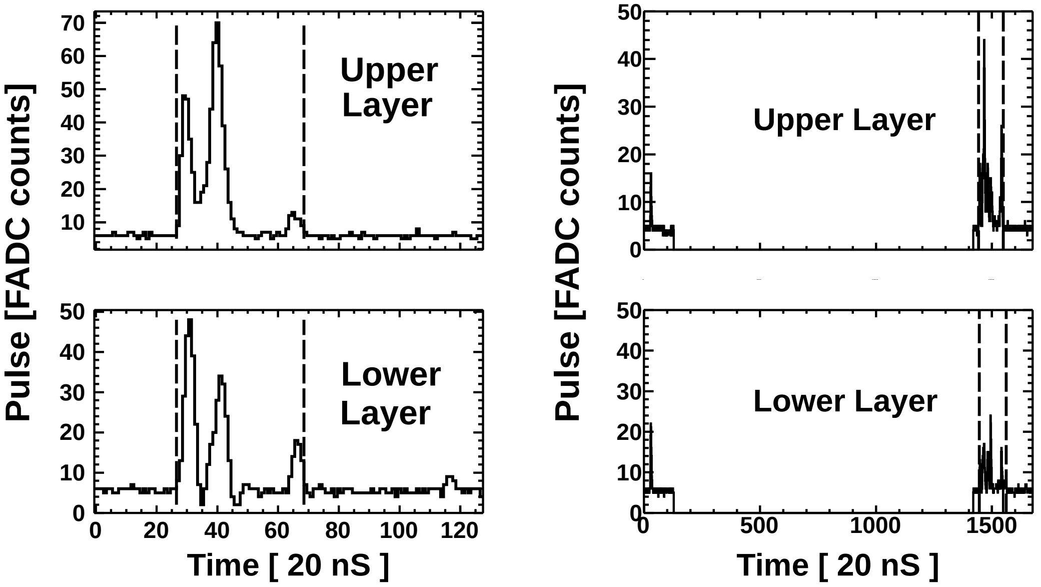

(a) (b)

Figure 5.1: Examples of the (processed) counter signals. Dashed lines show the signal selection. In both plots, the left dashed lines indicate the leading edges of the pulses, which define the counter time. (a): An example of a typical signal that is a part of the shower. (b): A signal from the shower (contained within the dashed lines) that was preceded by a random muon pulse, which occurred $\sim$25μ S earlier. Then the counter was silent for $\sim$25μ S (no Level-0 trigger), and finally, the counter triggered again due to the signal from the shower. The random muon pulse was excluded by the signal selection algorithm.

The next step is selecting the counters which belong to the event by determining the largest cluster of counters that are contiguous in space and time. A pair of counters is considered contiguous in space if their separation distance (on the square grid) does not exceed $\sqrt{2}$ counter spacing units. A pair of counters is considered contiguous in time if their time difference does not exceed their spatial separation (divided by the speed of light). The goal of this procedure is to exclude the counters that registered only the random atmospheric muons. Figure 5.2 shows a footprint of a typical high energy event after the pattern recognition.

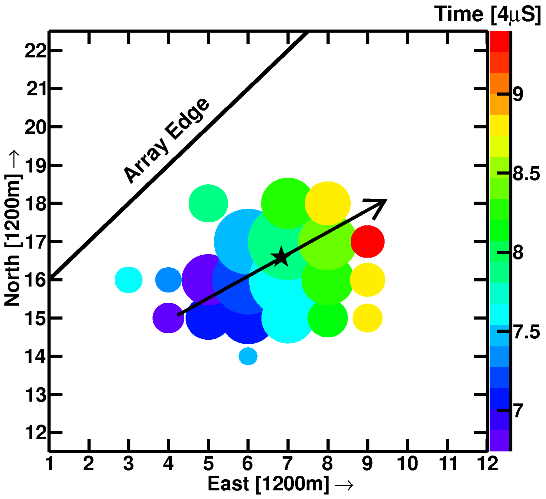

Figure 5.2: Event display picture of a typical TA SD event. Circle centers correspond to the counter positions, the circle areas are proportional to the logarithms of the counter pulse heights and the circle colors represents the counter times. The star shows the position of the shower core, and the arrow is the shower axis projected onto the ground, which is labeled by $\hat{\mathbf{u}}$.

5.2 Geometry Definitions and Starting Values

5.2.1 Geometry Definitions

The coordinate system used for reconstructing the showers is the central laser facility (CLF) frame (c.f. Chapters 2 and 3), where the X-axis points towards the East, Y-axis points towards the North, and the Z-axis points upwards. The event arrival direction represents the location on the local sky (unit vector) from where the event came. In these coordinates, the event zenith angle is the angle between the Z-axis and the event arrival direction and the event azimuthal angle is the angle of the X-Y projection of the event arrival direction, measured counterclockwise with respect to the X-axis.

Figure 5.3 shows the schematic view of the shower front at the time T_0, when the core of the shower hits the ground. The shower front is displayed as if it wasn't altered by the ground. Variables useful for describing the event geometry

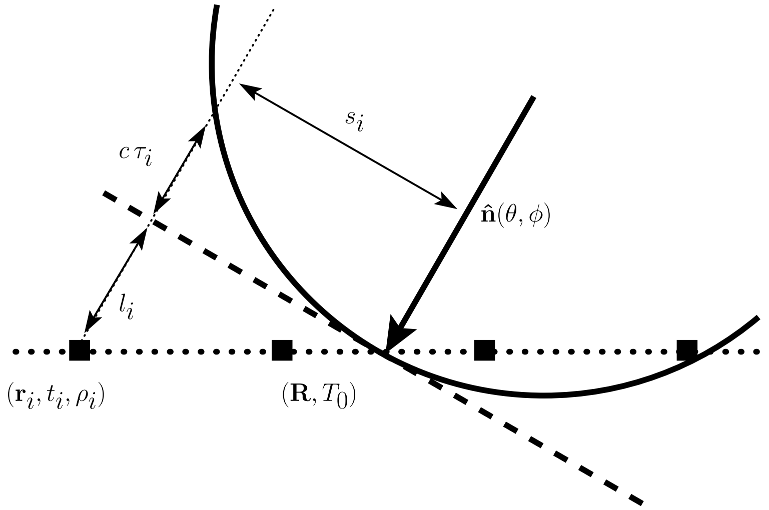
s_i
$c\tau_i$
$\hat{\mathbf{n}}(\theta,\phi)$
l_i
$(\mathbf{r}_i, t_i, \rho_i)$
$(\mathbf{R}, T_0)$

Figure 5.3: Schematic view of the shower front at the time T_0. The variables are described in the text.

are the event direction and the position of the shower impact point on the ground. Let $\hat{\mathbf{n}}(\theta,\phi)$ denote the (3 dimensional) unit vector along the direction of the shower propagation (opposite of the event arrival direction), $\hat{\mathbf{u}}(\phi)$ denote the (2 dimensional) unit vector of the projection of $\hat{\mathbf{n}}(\theta,\phi)$ on the ground, and θ, ϕ denote the shower zenith and azimuthal angles, so that the relations among the vectors and the angles are given by:

$$\begin{aligned} \hat{\mathbf{n}}(\theta,\phi) &= < -\sin(\theta)\cos(\phi), -\sin(\theta)\sin(\phi), -\cos(\theta) > \\ \hat{\mathbf{u}}(\phi) &= < -\cos(\phi), -\sin(\phi), 0 > \end{aligned} \tag{5.1}$$

Position of the shower impact point, called the *shower core*, is denoted by a two-component vector $\mathbf{R}$. It is *defined* to represent the point where the shower axis crosses the Z = 0 plane in the CLF frame, and the two components of $\mathbf{R}$ are the core X and Y coordinates.

The following variables are defined for an i^{th} counter that is a part of the event: s_i is the perpendicular distance from the shower axis, l_i is the distance from the shower core along the shower propagation axis, c is the speed of light, τ_i is the time delay due to the shower front curvature, and $\mathbf{r}_i, t_i, \rho_i$ are correspondingly the (3 dimensional) position, time, and the pulse height per unit area (in VEM/m^2).

5.2.2 Starting Values

Before reconstructing the event geometry using a time fit that requires minimizing a χ^2 function of many parameters, it is useful to obtain the initial estimates of the event geometry by simpler (but less accurate) means first.

The starting values for $\mathbf{R}$ in Figure 5.3 are approximated by $\mathbf{R}_{\mathrm{COG}}$, which is the center-of-gravity core position calculated from the first moments of the pulse height distribution ρ on the ground, measured by N counters:

$$(R_{\mathrm{COG}})_k = \frac{\sum_{i=1}^{N} \rho_i \, (r_i)_k}{\sum_{i=1}^{N} \rho_i}, \tag{5.2}$$

where $k = 1, 2$ values represent the x- and y- components of the vectors. The z- components of the counter positions, which are generally non-zero due to the curvature of the Earth and any unevenness of the ground, are neglected in approximating the starting values.

The starting value for the event $\hat{\mathbf{u}}(\phi)$ axis (up to a sign), is found by examining the 2^{nd} moments of the pulse height distribution ρ. Let M_{jk} denote the j, k component of the 2×2 matrix of the 2^{nd} moments of ρ:

$$M_{jk} = \frac{\sum_{i=1}^{N} \rho_i \left[(r_i)_j - (R_{\text{COG}})_j\right] \left[(r_i)_k - (R_{\text{COG}})_k\right]}{\sum_{i=1}^{N} \rho_i}, \tag{5.3}$$

Then the $\hat{\mathbf{u}}(\phi)$ axis lies approximately along the eigenvector of M_{jk} that corresponds to the larger eigenvalue (M_{jk} is symmetric by construction and it always has two eigenvalues). Geometrically, this amounts to finding the semi-major axis of the elliptical footprint of the shower (Figure 5.2). The event footprint is typically elliptical in shape for non-vertical showers and the method determines the shower $\hat{\mathbf{u}}(\phi)$ axis up to a sign (rotation by π). The correct sign is determined later, when one examines the time as well. For a vertical shower case ($\theta = 0$), the footprint on the ground is circular and the two eigenvalues of M_{jk} are equal. Although the $\hat{\mathbf{u}}(\phi)$ axis is not well-defined in such cases, it becomes irrelevant because the ϕ angle does not affect the event direction when $\theta = 0$.

Knowing (approximately) the shower core location and the $\hat{\mathbf{u}}$ axis (up to a sign) allows one to estimate the event zenith angle and determine the sign of the $\hat{\mathbf{u}}$ axis as well. Approximating the shower front by a plane ($\tau = 0$ approximation), the surface detector time can be expressed as:

$$t = T_0 + \frac{l}{c} = T_0 + [\sin(\theta)] \, \frac{(\mathbf{r} - \mathbf{R}) \cdot \hat{\mathbf{u}}}{c} \tag{5.4}$$

This linear relationship between the counter time and the distance from the core along the $\hat{\mathbf{u}}$ axis ($u_i = (\mathbf{r}_i - \mathbf{R}) \cdot \hat{\mathbf{u}}$) can be used for determining the approximate values of the sine of the event zenith angle $\sin(\theta)$ and the time of the shower core T_0 by a simple linear fit to the counter time t_i versus u_i. If the slope of the linear fit is negative ($\sin(\theta) < 0$), then one should reverse the $\hat{\mathbf{u}}$ axis and re-fit. This fixes the sign of the $\hat{\mathbf{u}}$ axis. Figure 5.4a shows the plot of the counter time versus counter distance from the core along the $\hat{\mathbf{u}}$ axis (the fit curves in the figure also include the shower front curvature effects). One can see from the Figure 5.4a that the t_i versus u_i (represented by points) relationship is roughly linear, and so the method of a simple linear fit to the equation 5.4 yields reasonable starting values for θ (typically within 10°).

5.3 Time Fit

All 5 shower geometry parameters T_0,R_x,R_y,θ,ϕ are varied while minimizing a function:

$$\chi^2_{\mathrm{G}} = \sum_{i=0}^{N} \frac{(t_i - t_i^{\mathrm{FIT}})^2}{\sigma^2_{t_i}} + \frac{(\mathbf{R} - \mathbf{R}_{\mathrm{COG}})^2}{\sigma^2_{\mathbf{R}_{\mathrm{COG}}}} \tag{5.5}$$

In equation 5.5, t_i^{FIT} is the time of the i^{th} counter as predicted by the fit function, which is of the form:

$$t^{\mathrm{FIT}} = T_0 + \frac{l}{c} + \tau \tag{5.6}$$

The uncertainty on the counter time consists of two components, added in quadrature:

$$\sigma_t = \sqrt{\sigma_e^2 + \sigma_\tau^2}\,, \tag{5.7}$$

where σ_τ is the uncertainty on time delay and σ_e is the uncertainty due to the electronics which, is 20 nS [82]. $\sigma_{\mathbf{R}_{\mathrm{COG}}} = 170\mathrm{m}$ is the corresponding uncertainty on core calculated by the center of gravity of pulse height distribution. We then fit to a modified Linsley time delay function [100, 99] with the shower front curvature parametrized as a function of zenith angle:

$$\begin{aligned} \tau &= (8\ \times 10^{-4}\mu\mathrm{S})\, a(\theta) \left(1.0 + \frac{s}{30\mathrm{m}}\right)^{1.5} \rho^{-0.5} \\ \sigma_\tau &= (7\ \times 10^{-4}\mu\mathrm{S})\, a(\theta) \left(1.0 + \frac{s}{30\mathrm{m}}\right)^{1.5} \rho^{-0.3} \\ a(\theta) &= \begin{cases} 3.38 - 0.018\,\theta & \theta < 25^o \\ 6.5 \times 10^{-5}\,\theta^3 + 8.8 \times 10^{-3}\,\theta^2 + 0.30\,\theta + 0.078 & 25^o \leq \theta < 35^o \\ \exp(-3.2 \times 10^{-2}\,\theta + 2.0) & \theta > 35^o \end{cases} \end{aligned} \tag{5.8}$$

which we adjusted by an iterative process using the TA SD data. To get the final values for the event geometry, we fit to a modified Linsley function in which the curvature parameter a becomes a fit parameter and is also allowed to vary (the χ^2 expression is the same as the Equation 5.5):

$$\tau = a\left(1-\frac{l}{12\times10^3\mathrm{m}}\right)^{1.05}\left(1.0+\frac{s}{30\mathrm{m}}\right)^{1.35}\rho^{-0.5} \tag{5.9}$$
$$\sigma_\tau = (1.56\times10^{-3})\left(1.0-\frac{l}{12\times10^3\mathrm{m}}\right)^{1.05}\left(1.0+\frac{s}{30\mathrm{m}}\right)^{1.5}\rho^{-0.3}$$

The additional factor of $(1-\frac{l}{12\times10^3\mathrm{m}})^{1.05}$ describes an additional "curvature development" effect, which was derived from the data. Figure 5.4a shows an example of the event time fit.

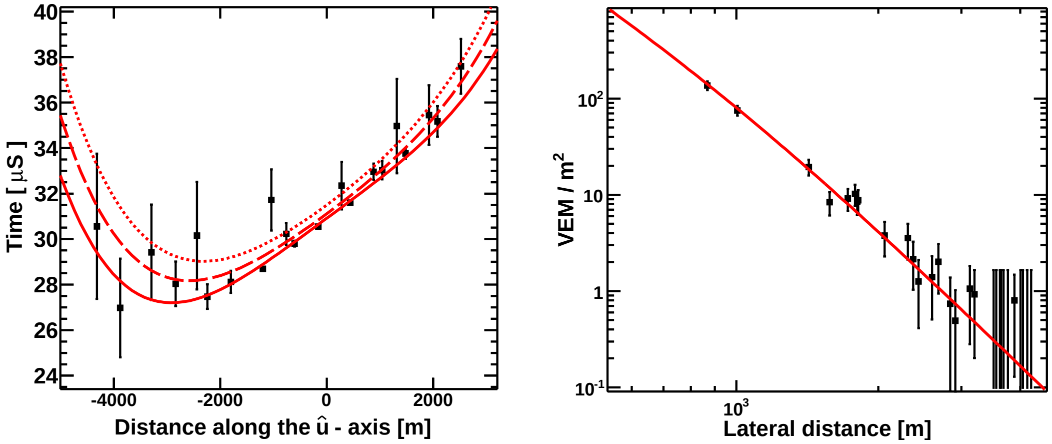

(a) (b)

Figure 5.4: Two fits for determining the SD event geometry and $S800$. (a): An illustration of the SD time fit. Counter time is plotted versus distance along the $\hat{\mathbf{u}}$-axis (points). Solid line represents the fit expectation time for counters that would lie directly on the $\hat{\mathbf{u}}$-axis, dashed and dotted lines are the fit expectation times for counters that are 1 km and 2 km off the $\hat{\mathbf{u}}$-axis, respectively. (b): Lateral distribution fit to the AGASA function. Counter pulse height is plotted versus the perpendicular (lateral) distance from the shower axis. Solid line represents the fit curve. Error bars with no points represent the silent counters (working counters which did not register any signal).

5.4 Lateral Distribution Fit

We use the same lateral distribution function (LDF) as the AGASA experiment [16] to fit the event lateral profile on the ground:

$$\rho = A\left(\frac{s}{91.6\text{m}}\right)^{-1.2}\left(1+\frac{s}{91.6\text{m}}\right)^{-(\eta(\theta)-1.2)}\left(1+\left[\frac{s}{1000\text{m}}\right]^2\right)^{-0.6} \tag{5.10}$$
$$\eta(\theta) = 3.97 - 1.79\left[\sec(\theta)-1\right]$$

The uncertainties [99] on the pulse height density are adjusted to fit the TA SD data:

$$\sigma_\rho = \sqrt{0.56\,\rho + 6.3\times10^{-3}\,\rho^2} \tag{5.11}$$

We minimize the function of the form:

$$\chi^2_{\text{LDF}} = \sum_{i=0}^{N}\frac{(\rho_i - \rho_i^{\text{FIT}})^2}{\sigma^2_{\rho_i}} + \frac{(\mathbf{R}-\mathbf{R}_{\text{COG}})^2}{\sigma^2_{\mathbf{R}_{\text{COG}}}} \tag{5.12}$$

The fit parameters are the core position **R** and the scaling factor A in front of the (AGASA) LDF function. Figure 5.4b shows a typical TA SD lateral distribution fit.

Counters closest to the shower core are removed from the lateral distribution fits (but not from the geometry fits) due to the saturation of their photomultiplier tubes, which occurs (in a typical counter) whenever the signal exceeds ∼50 VEM in a 20 nS time interval. Typically, one has 1 saturated counter per event.

5.5 First Energy Estimation

After successful geometry and LDF fits, we determine the signal size 800 meters [101] from the shower axis $S800 \equiv \rho(800\text{m})$ using equation 5.10 and use it along with the *reconstructed* $\sec(\theta)$ to determine the event energy from a carefully tested MC. To do this, we use a large statistics MC set to construct the energy estimation table. Figure 5.5 shows the energy as a function of reconstructed S800 and $\sec(\theta)$, where we plot the reconstructed values of $S800$ vs $\sec(\theta)$ lines for each value of true energy and the table made from the MC which shares all characteristics of the real data and has been processed by the same reconstruction programs as the real data. Color represents the true values of energy. We then reconstruct both real data and the MC events from $S800$, $\sec(\theta)$ using this energy function. This procedure is called the *first energy estimation* because the reconstructed energy obtained from the CORSIKA surface detector Monte-Carlo is not final: the energy is then rescaled to that of the fluorescence detector using a proportionality relationship described below.

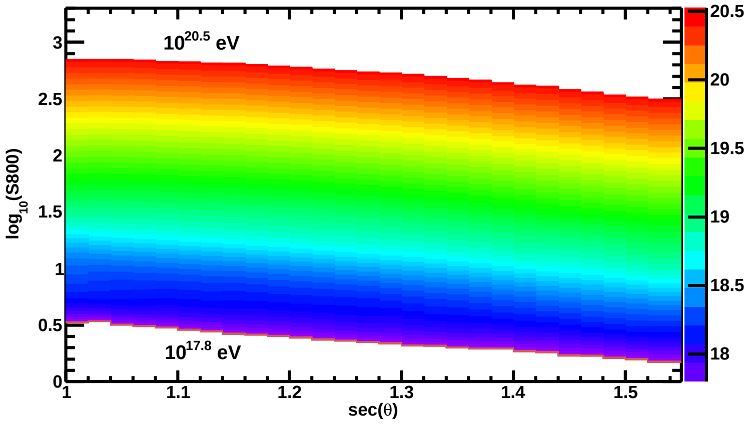

Figure 5.5: TA SD Energy Estimation Table

5.6 Energy Scale

To reduce the model dependence of the TA SD energy scale, the energy values obtained from the energy estimation table (Figure 5.5) are calibrated against the TA fluorescence detector using events that are seen in common by both TA SD and FD and are well reconstructed by each detector separately. In order to match the TA FD energy, the TA SD energies determined from the energy estimation table (Figure 5.5) need to be reduced by a factor 0.787. In other words, when the energy estimation procedure derived from the CORSIKA surface detector Monte-Carlo is applied to the real data, the predicted event energies are on average 27% higher than those of the fluorescence detector:

$$E_{\text{CORSIKA,SD}} = 1.27 \times E_{\text{FD}} \tag{5.13}$$

Figure 5.6a shows the energy of the TA SD plotted versus the energy of the TA FD, after the TA SD energy has been reduced by a factor of 1.27. Since the is a log-log plot, the symmetry around the $Y = X$ line indicates that the events energies are matching on the average. Also, Figure 5.6b shows the corresponding energy ratio histogram, indicating that the energies are well matched, on the average. The spread (RMS) of the histogram is 35%, which is consistent with the number one gets when the resolutions of the TA SD and the TA FD are added in quadrature.

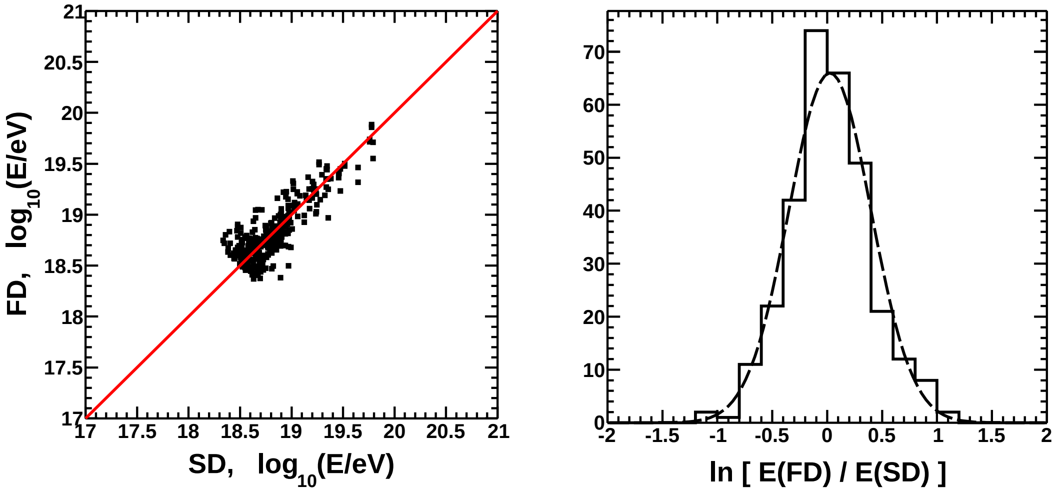

(a) (b)

Figure 5.6: TA SD and TA FD energy comparison plots. Well reconstructed events seen in common by the TA SD and the 3 TA FDs (BR, LR, MD) are compared simultaneously. The TA SD CORSIKA-derived energy has been reduced by a factor of 1/1.27 before making these comparisons. (a) is the scatter plot of E_{FD} versus E_{SD}. Solid line represents the $E_{FD} = E_{SD}$ case. (b) is the logarithm of the ratio of E_{FD} and E_{SD} represented by a 1-dimensional histogram. Dashed line is a fit to a Gaussian.

5.7 Quality Cuts and Resolution

After the fits are made and the event geometry and energy are determined, it is important to exclude poorly reconstructed events before calculating any physics results. The steeply falling spectrum and the 3-counter event trigger criteria (c.f. Chapter 2) mean that the lower energy events dominate the data sample. The low energy events are also the ones which hit fewer counters, have smaller numbers of particles, and have large upward fluctuations of their energy deposition into the scintillation counters. Such events, if not excluded from the data sample, will contaminate the high energy measurements and as a result, one may not be able to resolve the true energy spectrum features. While the quality cuts have been designed to optimize the energy resolution, it will be also shown that they yield a good angular resolution as well. In what follows, 6 quality cuts will be described, their impact on the energy resolution will be demonstrated, and the efficiency of each cut will be quoted using three different energy threshold values: $E > 10^{18.0}$, $E > 10^{18.5}$, and $E > 10^{19.0}$ eV.

5.7.1 Minimum Number of Counters Cut

Events with 5 or more counters are selected: $N_{\mathrm{SD}} \geq 5$, where N_{SD} is the number of counters that are part of the event, according to the space and time pattern recognition described above. Figure 5.7b shows the impact of this cut on the energy resolution. At this stage, the differences before the cut and after the cut is best illustrated by a two dimensional histogram of reconstructed energy versus the Monte-Carlo generated energy (using the spectral set). The majority of the resolution outliers is caused by the upward fluctuation of the energy deposition by the low energy events (the TA SD triggers at a minimum of only 3 counters), which are regarded as the noise triggers in this analysis. When the number of counters is large (5 or more), the effects of the upward fluctuations are reduced, as the probability of a consistent upward fluctuation in multiple counters is smaller. Hence the improvement in the energy resolution.

5.7.2 Zenith Angle Cut

The next important cut is than on the maximum event zenith angle. Events with zenith angle $\theta < 45^\circ$ are selected. Figure 5.7c shows the effects of adding this cut. There are two reasons for this cut. First, events with zenith angle greater than 60° are difficult to reconstruct because the particles pass through a large amount of the material ($\propto \sec(\theta)$), producing a small signal on the ground with larger fluctuations, and resulting in a poor resolution. The second reason is that the current TA SD MC describes the data well only up to 45° in (reconstructed) zenith angle. Extension of the maximum zenith angle cut to 55° is currently an on-going study of the TA SD MC.

5.7.3 Border Cut

For events that occur near the boundary, valuable information needed for successful reconstruction of the event $S800$ is lost, and as a result, the event energy is often underestimated. Events are therefore selected with reconstructed core position of at least 1200 m away from the edge of the array: $D_{\mathrm{Border}} \geq 1200$ m. Given that the TA SD counter spacing is 1200 m also, this cut ensures that on average, 1 counter is expected to be present between the shower core position and the edge of the array. Figure 5.7d demonstrates the effects of the cut: most events with underestimated energies are removed.

In Chapter 3, an additional boundary, called the T-shape boundary, was introduced for describing the logical sub-division of the SD array into the three parts. Because for the data before November 10, 2008 the 3 sub-arrays were triggering independently, a separate $D_{\mathrm{Border}} \geq 1200$ m cut is applied with respect to the

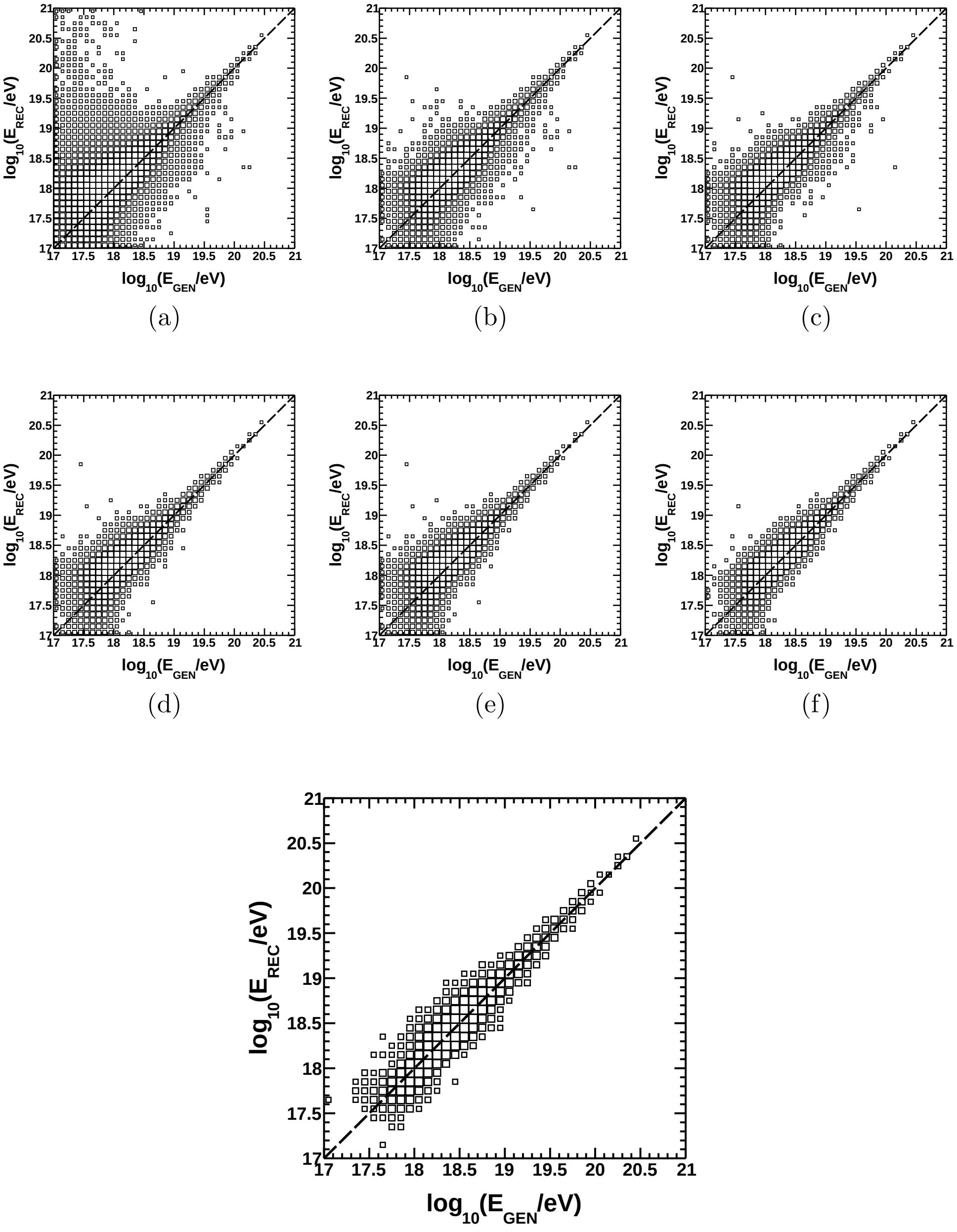

(a) (b) (c)

(d) (e) (f)

(g)

Figure 5.7: Effect of the quality cuts (added incrementally) on the energy resolution. Two dimensional histograms of reconstructed energy (E_{REC}) versus the MC generated energy (E_{GEN}) are plotted in all cases. Box size is proportional to the logarithm of the numbers of events in each (two dimensional) bin, and the dashed line represents the $E_{REC} = E_{GEN}$ case. (a): no cuts, (b): $N_{SD} \geq 5$, (c): $\theta < 45°$, (d): $D_{\text{Border}} > 1200$ m, (e): $\chi^2/\text{dof} < 4$, (f): $\sqrt{\sigma_\theta^2 + \sin^2(\theta)\sigma_\phi^2} < 5°$, (g): $\sigma_{S800}/S800 < 0.25$. This also describes the final case, where all of the 6 cuts have been applied.

T-shape boundary for events with dates before (and on) the November 10, 2008. Figure 5.8 shows the event core position scatter plot (core Y versus core X) with the border cuts. The T-shape boundary is irrelevant for the data after November 10, 2008 because since then, the TA SD is triggering as a single unit.

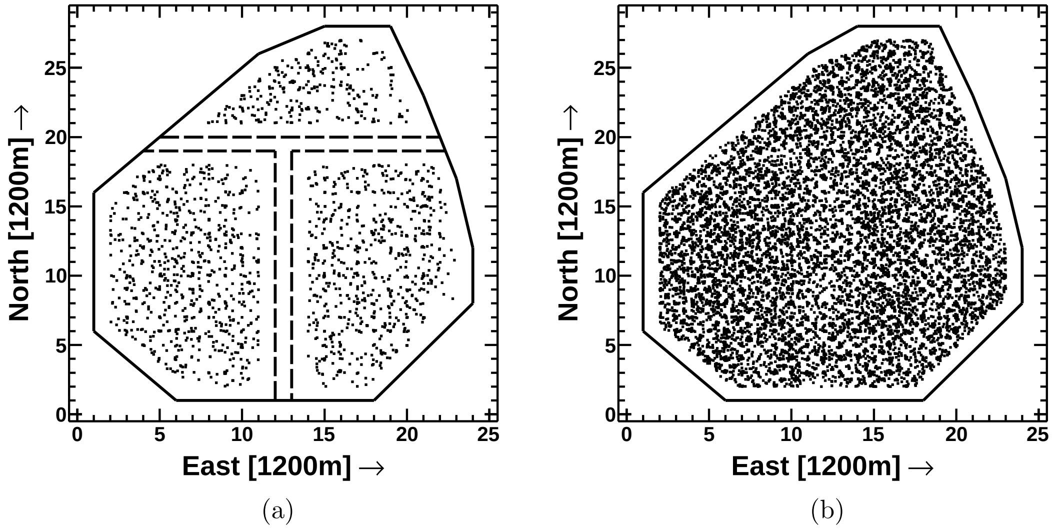

(a) (b)

Figure 5.8: Reconstructed event core position after the $D_{\text{Border}} \geq 1200$ m cut: (a) for 2008/05/11 - 2008/11/10 range, (b): for 2008/05/11 - 2011/04/25 range. Solid line represents the edge of the array and the dashed line represents the T-shape boundary (applicable only for 2008/05/11- 2008/11/10 data).

5.7.4 χ^2/d.o.f. cuts

Events are selected with χ^2_{G}/d.o.f. < 4 and χ^2_{LDF}/d.o.f. < 4, where χ^2_{G}/d.o.f. and χ^2_{LDF}/d.o.f. are the reduced χ^2 (per degree of freedom) values of the geometry and the lateral distribution fits. Figure 5.7e shows the effect of these cuts.

5.7.5 Pointing Direction Uncertainty Cut

The geometry fit is made by minimizing the χ^2_{G} function (Equation 5.5) using the MINUIT package [102], which also provides the uncertainties on the fit parameters. The uncertainties of θ (zenith angle) and ϕ (azimuthal angle), labeled by σ_θ and σ_ϕ, respectively, are combined to form the overall pointing direction uncertainty σ_{G}:

$$\sigma_{\mathrm{G}} = \sqrt{\sigma_\theta^2 + \sin^2\theta\,\sigma_\phi^2} \tag{5.14}$$

Events with well reconstructed geometries are then selected by requiring $\sigma_{\mathrm{G}} < 5°$. This cut improves the energy resolution also, as Figure 5.7f shows.

5.7.6 Fractional S800 Uncertainty Cut

Normalization constant in front of the AGASA lateral distribution function (denoted by A) is a fit parameter which is proportional to the S800 (signal size at a lateral distance of 800 m). The fractional uncertainty on S800 is simply obtained by:

$$\sigma_{\mathrm{S800}}/\mathrm{S800} = \sigma_A/A, \tag{5.15}$$

where σ_A is the fit parameter uncertainty provided by MINUIT [102] when the χ^2 function in equation 5.12 is minimized. Events with $\sigma_{\mathrm{S800}}/\mathrm{S800} < 0.25$ are selected, and Figure 5.7g shows the result of applying this cut. This is the final cut which leads to improved energy resolution: background due to the low energy events reconstructing much higher that the true energy is eliminated.

5.7.7 Efficiency of the Quality Cuts

In this discussion, the efficiency of a quality cut represents the fraction of events *retained* after (incrementally) imposing the cut. Table 5.1 summarizes the efficiencies of all 6 quality cuts described above, using 3 different (MC generated) energy thresholds. In the study of cuts, a MC spectral set (c.f. Chapter 4) was used with maximum (generated) zenith angle of 60°. Final efficiency (due to all quality cuts combined) is also quoted. Only the MC events that triggered the array were used in producing Table 5.1.

Quality cut	Efficiency, $E > 10^{18}$ eV	Efficiency, $E > 10^{18.5}$ eV	Efficiency, $E > 10^{19}$ eV
$N_{\text{SD}} \geq 5$	0.674	0.931	0.973
$\theta < 45^{\circ}$	0.741	0.702	0.677
$D_{\text{Border}} \geq 1200$ m	0.865	0.814	0.748
$\chi^2_{\text{G}}/\text{d.o.f.} < 4$, $\chi^2_{\text{LDF}}/\text{d.o.f.} < 4$	0.928	0.938	0.981
$(\sigma_\theta^2 + \sin^2\theta\,\sigma_\phi^2)^{1/2} < 5^{\circ}$	0.656	0.925	0.995
$\sigma_{\text{S800}}/\text{S800} < 0.25$	0.534	0.887	0.995
All cuts combined	0.14	0.41	0.48

Table 5.1: Efficiency of the quality cuts

As can be seen from the Table 5.1, the most inefficient cuts at the high energies are the maximum zenith angle, and the border cuts, while the effects of cutting on the number of counters and fitting uncertainties are relatively small. For the low energy events, on the other hand, the situation is different: low energy events hit fewer counters, deposit smaller amounts of energy, and consequently, their geometry and energy are more difficult to determine, which are the reasons for large inefficiencies due to the fit uncertainties and the number of counter cuts.

5.7.8 Resolution

The TA SD resolution is determined using the Monte-Carlo spectral sets (c.f. Chapter 4), which are always processed with the same reconstruction programs as the data and use the same quality cuts as the data. In addition, the TA surface detector MC separately saves the true (generated) variables, which are accessed only after the event reconstruction and the quality cuts have been applied.

The angular resolution is best characterized by considering a cumulative histogram of the opening angle between the reconstructed event direction $\hat{\mathbf{n}}_{\text{REC}}$ and the true (MC generated) direction $\hat{\mathbf{n}}_{\text{GEN}}$:

$$\delta = \cos^{-1}(\hat{\mathbf{n}}_{\text{REC}} \cdot \hat{\mathbf{n}}_{\text{GEN}}) \tag{5.16}$$

The unit vectors $\hat{\mathbf{n}}_{\mathrm{REC}}$ and $\hat{\mathbf{n}}_{\mathrm{GEN}}$ are obtained from the event zenith and azimuthal angles (reconstructed and generated) by using equation 5.1. Figure 5.9 shows the angular resolution of the TA SD evaluated from a Monte-Carlo spectral set using three energy ranges. Choosing the 68% confidence limits for quoting the answers, the TA SD angular resolution values are: 2.4^o for $10^{18.0}\mathrm{eV} < E < 10^{18.5}\mathrm{eV}$, 2.1^o for $10^{18.5}\mathrm{eV} < E < 10^{19.0}\mathrm{eV}$, and 1.4^o for $E > 10^{19.0}\mathrm{eV}$.

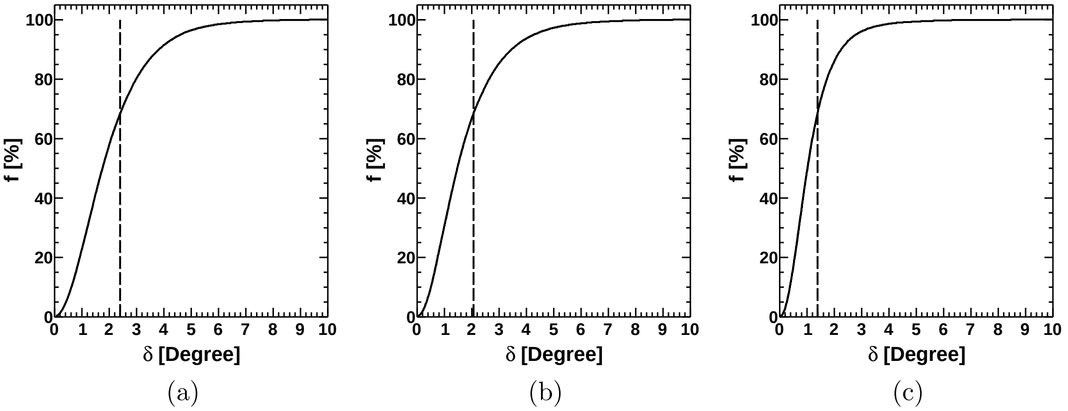

Figure 5.9: The TA SD angular resolution evaluated using a Monte-Carlo spectral set. Cumulative histograms of the opening angle between the reconstructed and the true (MC generated) event directions are shown using three energy slices: (a) $10^{18.0}\mathrm{eV} < E < 10^{18.5}\mathrm{eV}$, (b) $10^{18.5}\mathrm{eV} < E < 10^{19.0}\mathrm{eV}$, (c) $E > 10^{19.0}\mathrm{eV}$. X axis represents the opening angle δ and the Y axis represents the fraction f of events (in percent), reconstructing within a given opening angle with respect to their true directions. Dashed lines represents the 68% confidence limits, which are the values of δ containing 68% of all reconstructed events in the given energy ranges.

The energy resolution is most readily characterized by the root-mean-square (RMS) of the reconstructed (E_{REC}) to the generated (E_{GEN}) energy ratio distribution. It is advantageous to take the natural logarithm of the energy ratio before producing the histogram and evaluating the RMS because the logarithm treats the under-reconstructing and over-reconstructing events in a symmetric way. In contrast, a histogram of ratios would not properly account for the under-reconstructing events, which can lead to smaller RMS values and an overstated resolution. The RMS $\sigma_{\ln E}$ of the (natural) logarithm of the $E_{\mathrm{REC}}/E_{\mathrm{GEN}}$ ratio distribution can also be interpreted as a fraction σ_E of the true energy using:

$$\sigma_E = \exp(\sigma_{\ln E}) - 1 \tag{5.17}$$

Figure 5.10 shows the energy resolution of the TA SD for three (MC generated) energy ranges. The histograms were produced using the MC spectral sets with varying statistics (10 to 40 times that of the real data) to yield similar numbers of events in the histograms. Using the RMS values of the $E_{\mathrm{REC}}/E_{\mathrm{GEN}}$ distributions and equation 5.17, one arrives at the following answers for the TA SD energy resolution (in percents of the true energy): 36% for $10^{18.0}\mathrm{eV} < E_{\mathrm{GEN}} < 10^{18.5}\mathrm{eV}$, 29% for $10^{18.5}\mathrm{eV} < E_{\mathrm{GEN}} < 10^{19.0}\mathrm{eV}$, and 19% for $E_{\mathrm{GEN}} > 10^{19.0}\mathrm{eV}$.

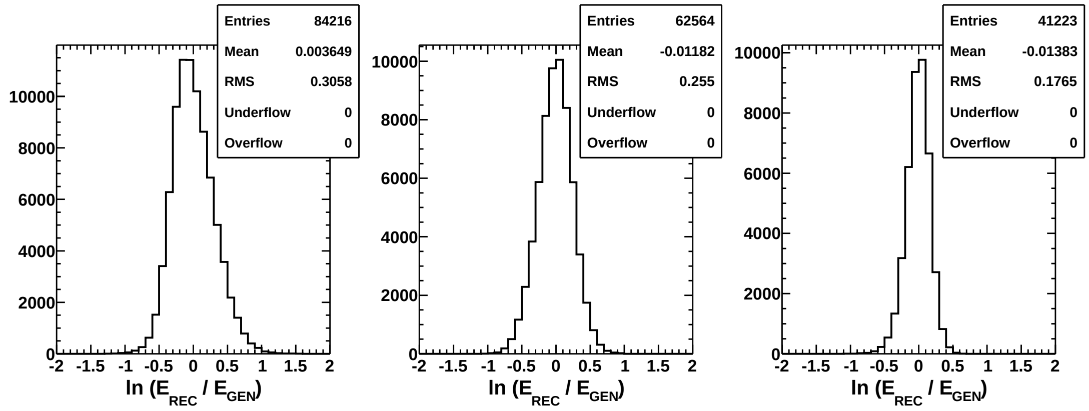

(a) (b) (c)

Figure 5.10: The TA SD energy resolution evaluated using the Monte-Carlo spectral sets. Energy resolution is shown for three energy slices (in MC generated energy): (a) $10^{18.0}\mathrm{eV} < E_{\mathrm{GEN}} < 10^{18.5}\mathrm{eV}$, (b) $10^{18.5}\mathrm{eV} < E_{\mathrm{GEN}} < 10^{19.0}\mathrm{eV}$, (c) $E_{\mathrm{GEN}} > 10^{19.0}\mathrm{eV}$. Natural logarithm of the ratio of the reconstructed energy divided by the MC generated energy was used for producing the histograms.

5.8 Analysis Structure

Figure 5.11 summarizes the event reconstruction process, which is the same for both data and the Monte-Carlo. Pass1 and pass2 analyses are performed by *rufptn* and *rufldf* programs, respectively. Both programs have been developed

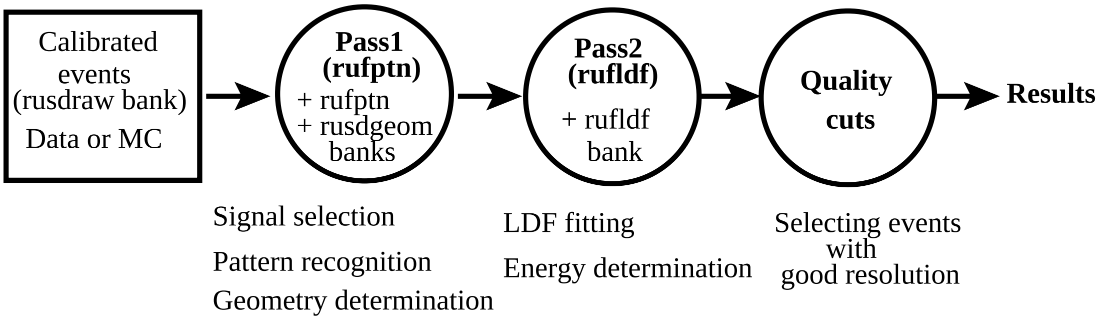
Calibrated events (rusdraw bank) Data or MC
Pass1 (rufptn)
+ rufptn + rusdgeom banks
Pass2 (rufldf)
+ rufldf bank
Quality cuts
Results
Signal selection
Pattern recognition
Geometry determination
LDF fitting
Energy determination
Selecting events with good resolution

Figure 5.11: Event reconstruction analysis chain, which is the same for both data and the Monte-Carlo. Pass1 analysis, done by a program called "rufptn", adds two DST banks for each event: "rufptn" (intermediate variables) and "rusdgeom" (geometry results). Pass2 analysis, done by a program called "rufldf", adds a DST bank called "rufldf", which stores the results of the fit to the AGASA lateral distribution function (LDF) and the (reconstructed) event energy.

at Rutgers and are a part of this work. These analysis programs add new DST banks (c.f. Chapter 3) with reconstruction information for each SD event. The important variables of the DST banks are summarized in the Tables 5.2, 5.3, and 5.4. The reconstruction programs do not remove any events: the quality cuts are applied *after* the pass1 and pass2 analyses, prior to the calculation of the physics results which will be described in the next chapter.

Variable	Description
tyro_xymoments	1^{st} and 2^{nd} moments of pulse heights (equations 5.2 and 5.3).
tyro_xypmoments	Eigenvalues of the matrix in the equation 5.3.
tyro_u	Initial estimate of the event $\hat{\mathbf{u}}(\phi)$ axis (equation 5.1).
tyro_theta	Initial estimate of the event zenith angle.
tyro_phi	Initial estimate of the event azimuthal angle.
nhits	Number of processed signals (*hits*).
nsclust	Number of hits (in the largest cluster) contiguous in space.
nstclust	Number of counters (in the largest cluster) contiguous in space-time.
nborder	Number of counters that lie on the border of the array.
tearliest	A reference time common to all signals.

The following variables describe the processed signals:

Variable	Description
isgood	A flag that describes the signal as follows: 0 - the counter was not working 1,2 - the signal corresponds to the random muon 3,4 - the signal is a part of the event. 5 - the signal is a part of the event and it saturates the counter.
xxyy	Logical ID number of the counter.
xyzclf	X, Y, and Z coordinates of the counter (in CLF frame).
nfold	Number of 128 FADC time slice waveforms involved in determining the signal.
sstart	FADC time slices that corresponds to the leading edge of the pulse.
sstop	FADC time slice where the signal stopped.
reltime	Signal time with respect to the common reference time.
fadcpa	Signal size (area, pedestal subtracted), in FADC counts.
pulsa	Signal size (area, pedestal subtracted), in VEM units.
ped	Pedestal value used in processing the signal.
pederr	RMS of the pedestal used in processing the signal.
vem	FADC counts per VEM used in processing the signal.

Table 5.2: Summary of the rufptn bank.

Variable	Description
xcore	Shower core X position.
dxcore	Fit uncertainty of the shower core X.
ycore	Shower core Y position.
dycore	Fit uncertainty of the shower core Y.
theta	Event zenith angle.
dtheta	Fit uncertainty of the event zenith angle.
phi	Event azimuthal angle.
dphi	Fit uncertainty of the event azimuthal angle.
a	Shower curvature (fitted) (equation 5.9).
da	Uncertainty of the fitted curvature.
t0	Time of the core hitting the ground.
dt0	Fit uncertainty of the core time.
chi2	χ^2 of the fit.
ndof	Number of degrees of freedom in the fit.
tearliest	Common reference time.

The following variables describe the counters:

Variable	Description
igsd	A flag that describes the counter as follows: 0 - the counter was not working 1 - the counter registers only the random muon hits 2 - the counter is a part of the shower 3 - the counter is a part of the shower and it is saturated.
xxyy	Logical ID number of the counter.
xyzclf	X, Y, and Z coordinates of the counter (in CLF frame).
pulsa	Counter pulse height, calibrated in VEM.
sdtime	Counter time with respect to the common reference time.

Table 5.3: Summary of the rusdgeom bank.

Variable	Description
xcore	Shower core X position from the LDF fit
dxcore	Fit uncertainty of the shower core X.
ycore	Shower core Y position from the LDF fit.
dycore	Fit uncertainty of the shower core Y.
sc	Scaling factor in front of the AGASA LDF (equation 5.10).
dsc	Fit uncertainty on the LDF scaling factor.
chi2	χ^2 of the LDF fit (equation 5.12).
ndof	Number of degrees of freedom in the LDF fit.
bdist	Distance of the shower core from the edge of the SD array.
tdistbr	Distance of the shower core from the edge of the BR sub-array.
tdistlr	Distance of the shower core from the edge of the LR sub-array.
tdistsk	Distance of the shower core from the edge of the SK sub-array.

Table 5.4: Summary of the rufldf bank.

Chapter 6

TA SD Energy Spectrum

The subject of this chapter is the determination of cosmic ray flux as a function of energy above 10^{18} eV using the Telescope Array surface detector data. First, the measurement procedures are described. Next, a calculation of the detector aperture and the exposure using the Monte-Carlo method is provided. Finally, the TA SD energy spectrum is produced and the systematic uncertainties are evaluated. While the official measurement of the TA SD spectrum, a result of this work which has been presented in conferences [103] and which is expected to appear in [104], starts at $10^{18.2}$ eV, it will be shown here that the systematic uncertainties below $10^{18.2}$ eV can be controlled and the measurement can be extended further down to $E = 10^{18}$ eV.

In the discussions below, the following definition of the differential cosmic ray flux J is used:

$$J = \frac{\mathrm{d}^4 N}{\mathrm{d}E\,\mathrm{d}A\,\mathrm{d}\Omega\,\mathrm{d}t}\,, \tag{6.1}$$

where $\mathrm{d}N$ is the number of particles in the energy range $\mathrm{d}E$, passing through an area and solid angle elements $\mathrm{d}A$ and $\mathrm{d}\Omega$ in a time interval $\mathrm{d}t$, in the reference frame of the Telescope Array experiment. Another useful quantity, which will be necessary for discussing the astrophysical aspects of the measurement in the next chapter, is the integral flux $J_{>}$, which is obtained from J by the following integration:

$$J_{>} = \int_{E}^{\infty} \mathrm{d}E'\,J(E') \tag{6.2}$$

6.1 Measurement Procedures

A simplifying assumption of the measurement is that the *true* cosmic ray flux is isotropic in the local sky coordinates, i.e. $J(E)$ is a function of the event energy only and doesn't depend on the event zenith and azimuthal angles θ and ϕ. No significant anisotropies above 10^{17} eV have been reported by cosmic ray experiments to date.

For a moment, suppose that the events are detected with a 100 % efficiency and their energies are measured with an arbitrary accuracy. Then it is straightforward to calculate the flux from the event rate, a quantity that is measured by the detector. Let A and Ω denote the detection area and solid angle (it is often convenient to combine the area and solid angle into one geometric factor $A\,\Omega$, which we call the *geometric aperture*), T denote the time period of the observation, and N_i be the histogram of measured event energies. Here, i labels the $\log_{10}E$ bins with (logarithmic) bin sizes b_i, and N_i represents the numbers of events in these bins. Also, let E_i denote the (linear) value of the energy that corresponds to the bin center. Then the flux (Equation 6.1) in the i^{th} bin is expressed as:

$$J_i^{\mathrm{IDEAL}} = \frac{N_i/\Delta E_i}{A\,\Omega\,T}, \tag{6.3}$$

where ΔE_i is the energy interval covered by the i^{th} bin:

$$\Delta E_i = E_i\,(10^{b_i/2} - 10^{-b_i/2}) \tag{6.4}$$

A real detector has a finite resolution and an efficiency that depends on energy. Below the efficiency plateau energy $E_{\mathrm{C}} = 10^{18.9}$ eV in Figure 6.1a, the TA SD acceptance also depends on the zenith angle: inclined events trigger more counters and thus are more likely to be included in the data sample, as Figure 6.1b shows. A quantity $\sin^2\theta$ is plotted in Figure 6.1b to account for the zenith angle dependence of the solid angle seen by the ground array: $\mathrm{d}\Omega/\mathrm{d}\theta \propto \sin\theta\cos\theta$, so that $\Omega \propto \sin^2\theta$, which means that the equal-size bins in $\sin^2\theta$ correspond to the equal-size bins

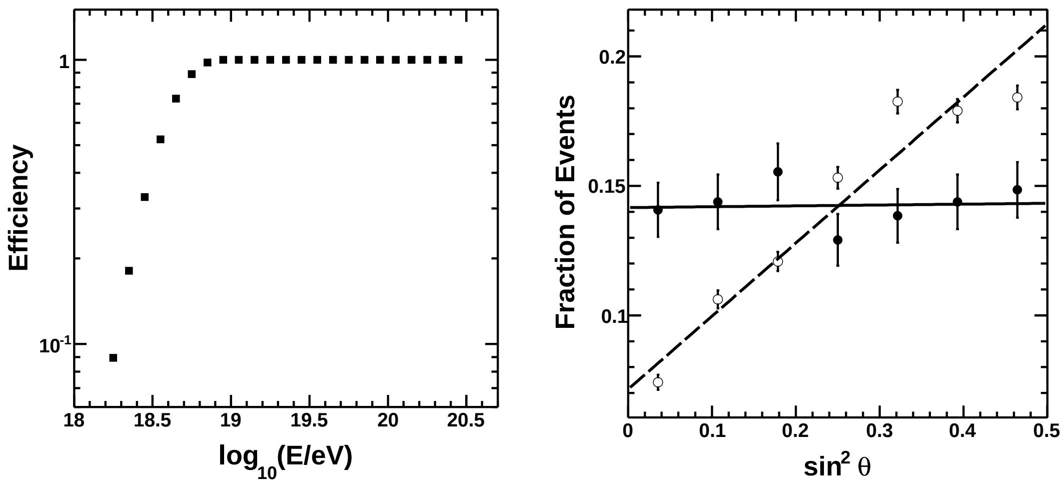

(a) (b)

Figure 6.1: (a): TA SD Reconstruction efficiency. 100% efficiency plateau ($E > 10^{18.9}$ eV) corresponds to the (geometric) aperture value $A\,\Omega = 890$ km^2 sr. (b): Normalized distributions of the event $\sin^2\theta$ for $E < 10^{18.9}$ eV (open circles) and $E > 10^{18.9}$ eV (filled circles). Dashed and solid lines show linear fits to these distributions. Above the $10^{18.9}$ eV threshold, the acceptance does not depend on the zenith angle: the slope of the solid line is 0.003 ± 0.03.

in solid angle. In summary, Figure 6.1 demonstrates that Equation 6.3 does not apply below the efficiency plateau energy E_{C}.

Even above the critical energy E_{C}, the detector has a finite energy resolution (19%, as shown in Chapter 5), which has non-negligible effects on the measurement. Because the flux is (approximately) a steeply falling power law, the bin-to-bin migration effects caused by the resolution will shift the result in a systematic way. Let E_T denote the true energy, E_M denote the measured (reconstructed) energy, and suppose that the flux is calculated as a function of $\log_{10}E$. If the differential flux distribution is $\propto E_T^{-\gamma}$, then the quantity $X_T = \log_{10}(E_T)$ is distributed as $N_T = F\,E_T^{-(\gamma-1)}$, for some normalization constant F. Let σ_X denote the resolution of $\log_{10}E$. Then the distribution of the measured quantity $X_M = \log_{10}(E_M)$ can be approximated by the convolution of the true distribution and the (Gaussian) resolution smearing function:

$$\begin{aligned}
N_M &= \frac{F}{\sigma_X \sqrt{2\,\pi}} \int_{-\infty}^{+\infty} \mathrm{d}X_T \, E_T^{-(\gamma-1)} \exp\left[-\frac{(X_M - X_T)^2}{2\,\sigma_X^2}\right] \\
&= \frac{F}{\sigma_X \sqrt{2\,\pi}} \int_{-\infty}^{+\infty} \mathrm{d}X_T \exp\left[-\mathrm{ln}10\,(\gamma-1)\,X_T - \frac{(X_M - X_T)^2}{2\,\sigma_X^2}\right] \\
&= F\,E_M^{-(\gamma-1)} \exp\left[(\gamma-1)^2\,(\mathrm{ln}10\,\sigma_X)^2/2\right] \qquad (6.5) \\
&= F\,E_M^{-(\gamma-1)} \exp\left[(\gamma-1)^2\,\sigma_{\mathrm{ln}E}^2/2\right] \; ,
\end{aligned}$$

where $\sigma_{\mathrm{ln}E} = \mathrm{ln}10\,\sigma_X$ is now the resolution of the natural logarithm of energy, discussed and quoted for the TA SD in 5.7 (see the energy resolution figures). The effect of the resolution on the (measured) $\log_{10}E$ histogram is then expressed as:

$$\frac{N_M(E)}{N_T(E)} - 1 = \exp\left[\frac{(\gamma-1)^2\,\sigma_{\mathrm{ln}E}^2}{2}\right] - 1 \qquad (6.6)$$

For example, substituting $\sigma_{\mathrm{ln}E} = 0.18$ for $E > 10^{19}$ eV (from Chapter 5) and $\gamma = 3$ into Equation 6.6, gives a 6.7 % effect on the flux measurement, just above E_C. This does not hold for the entire $E > E_C$ range because the spectral index γ also changes at the highest energies, as will be shown later in this chapter. Clearly, Equation 6.3 needs to be modified for $E > E_C$ case as well, to include, or *fold-in*, the effects of the resolution.

6.1.1 Unfolding the Flux

The process of extracting the true distribution from the measured one is called *unfolding* (cosmic ray flux is related to the distribution of event energies by Equation 6.3). To this effect, we use a standard technique, called the *method of correction factors* [105]. The method is applied to the TA SD data in the same way as it was done by the HiRes experiment [88] for a fluorescence detector, which consists of modifying the ideal measurement formula (Equation 6.3) to fold-in the energy and zenith angle dependence of the detector acceptance, as well as the effects of the detector resolution:

$$J_i = \frac{(N_{\text{REC}}^{\text{DATA}})_i / \Delta E_i}{\frac{(N_{\text{REC}}^{\text{MC}})_i}{(N_{\text{GEN}}^{\text{MC}})_i} A_{\text{GEN}}\, \Omega_{\text{GEN}}\, T}, \tag{6.7}$$

where $(N_{\text{REC}}^{\text{DATA}})_i$ and $(N_{\text{REC}}^{\text{MC}})_i$ are the numbers of the data and the MC events reconstructing in the i^{th} $\log_{10}E$ bin, $(N_{\text{GEN}}^{\text{MC}})_i$ is the number of generated Monte-Carlo events, $A_{\text{GEN}}\, \Omega_{\text{GEN}}$ is the geometric aperture in which the Monte-Carlo events are generated, and T is the detector on-time. It should be emphasized that $(N_{\text{REC}}^{\text{DATA}})_i$ and $(N_{\text{REC}}^{\text{MC}})_i$ are evaluated using the *reconstructed* event energies, while $(N_{\text{GEN}}^{\text{MC}})_i$ are evaluated using the MC *generated* (true) energies. The Monte-Carlo describes all known characteristics of the data (see Chapter 4 for the data and MC comparisons) and it is reconstructed by the same analysis tools as the data, including the quality cuts (c.f. Chapter 5). Finally, we note that the Monte-Carlo is generated into a larger geometric aperture $A_{\text{GEN}}\, \Omega_{\text{GEN}}$ than that of the measurement $A\,\Omega$ to account for the boundary effects (in the event core position and zenith angle) and Equation 6.7 is equivalent to

$$J_i = \frac{(N_{\text{REC}}^{\text{DATA}})_i / \Delta E_i}{\frac{A_{\text{GEN}}\, \Omega_{\text{GEN}}}{A\,\Omega} \frac{(N_{\text{REC}}^{\text{MC}})_i}{(N_{\text{GEN}}^{\text{MC}})_i} A\,\Omega\, T} = C_i\, J_i^{\text{IDEAL}}\,, \tag{6.8}$$

where J_i^{IDEAL} is the expression for the flux under ideal measurement conditions (Equation 6.3) and $C_i = \frac{A\,\Omega}{A_{\text{GEN}}\, \Omega_{\text{GEN}}} \frac{(N_{\text{GEN}}^{\text{MC}})_i}{(N_{\text{REC}}^{\text{MC}})_i}$ are the correction factors.

6.1.2 Aperture and Exposure

The quantities

$$\begin{aligned} \alpha_i &= A_{\text{GEN}}\, \Omega_{\text{GEN}}\, (N_{\text{REC}}^{\text{MC}})_i / (N_{\text{GEN}}^{\text{MC}})_i \\ \lambda_i &= \alpha_i\, T \end{aligned} \tag{6.9}$$

appearing in Equation 6.7 are interpreted as the generalized aperture and exposure, respectively. As described in Chapter 4, the TA SD Monte-Carlo was generated with the shower impact position randomly distributed inside a 25 km circle, zenith angle sampled from a $\sin\theta\cos\theta$ distribution for θ going from 0 to $\pi/3$, and the azimuthal angle distributed randomly in a 0 to 2π interval. Therefore, the geometric aperture of the Monte-Carlo is calculated as:

$$\begin{aligned} A_{\mathrm{GEN}} &= \pi\,(25\ \mathrm{km})^2 \\ \Omega_{\mathrm{GEN}} &= \int_0^{2\pi} \mathrm{d}\phi \int_0^{\pi/3} \mathrm{d}\theta \sin\theta\cos\theta = \pi\sin^2\theta\Big|_0^{\pi/3} = \frac{3\,\pi}{4} \\ A_{\mathrm{GEN}}\,\Omega_{\mathrm{GEN}} &\approx 4626\ \mathrm{km}^2\ \mathrm{sr} \end{aligned} \tag{6.10}$$

In the present work, the TA SD data from May 11, 2008 until April 25, 2011 is used, so that $T = 1080$ days. Any detector off-time (a $\sim$1% effect) occurring in this time period (e.g. due to the maintenance) is included in the Monte-Carlo simulation and it is automatically accounted for by the quantity $(N_{\mathrm{REC}}^{\mathrm{MC}})_i/(N_{\mathrm{GEN}}^{\mathrm{MC}})_i$, which enters the generalized aperture and exposure calculations in Equation 6.10. Figure 6.2 shows the results plotted versus the (base-10 logarithm of) energy. It can be seen from the figures that both aperture and the exposure level off near $E_C = 10^{18.9}$ eV and become nearly geometric. The values of the aperture and exposure for the cosmic ray energies $E > E_C$ are:

$$\begin{aligned} A\,\Omega &\approx 890\ \mathrm{km}^2\,\mathrm{sr} \\ A\,\Omega\,T &\approx 2640\ \mathrm{km}^2\,\mathrm{sr}\,\mathrm{yr}\,. \end{aligned} \tag{6.11}$$

It should be emphasized that $A\,\Omega$ represents the actual (nearly geometric) aperture of the measurement, when one uses (purely geometrical) cuts $D_{\mathrm{Border}} > 1200$ m and $\theta < 45°$ (c.f. Chapter 5), while $A_{\mathrm{GEN}}\,\Omega_{\mathrm{GEN}}$ corresponds to the simulation, which is much larger than $A\,\Omega$ to properly account for the effects of the boundary.

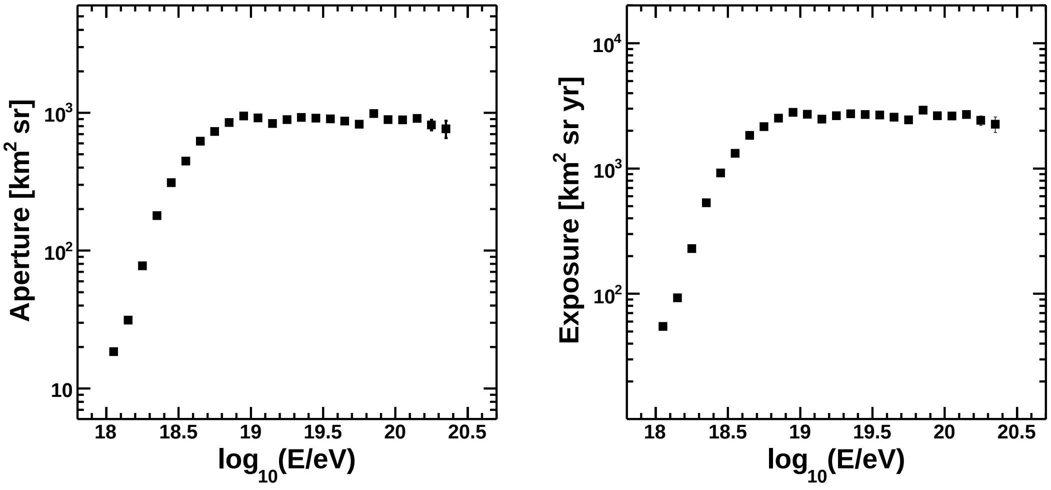

(a) (b)

Figure 6.2: Generalized TA SD aperture and exposure calculated by the Monte-Carlo method (Equation 6.10). Small-scale features in these quantities seen at $E \sim 10^{19}$ eV and $E \sim 10^{19.8}$ eV are caused by rapid changes in the detector efficiency and the power law of the (MC) input energy spectrum, respectively. (a): Generalized TA SD aperture. For $E > 10^{18.9}$ eV, the aperture becomes ~ 890 km^2 sr. (b): Generalized TA SD exposure over 1080 days of data. Above $10^{18.9}$ eV, the exposure is ~ 2640 km^2 sr. Both (generalized) aperture and exposure include the detector efficiency and the effects of the resolution.

6.2 Measured Flux

The cosmic ray flux as a function of event energy is calculated from the event energy histogram using Equation 6.7. Figure 6.3 shows the results. The statistical uncertainties of the flux points are dominated by the statistics of the data. The 68% confidence limits shown as error bars in Figure 6.3b were determined using Feldman-Cousins calculation [106] (uncertainties on small numbers of events listed in Table II of the publication). To be able to see the features in the energy (flux) spectrum clearly, it is advantageous to display the result in a different form. Since the flux generally falls off like $\sim E^{-3}$, we multiply the flux in each bin by E_i^3, where E_i is the energy that corresponds to the center of the i^{th} bin. The result is shown in Figure 6.4.

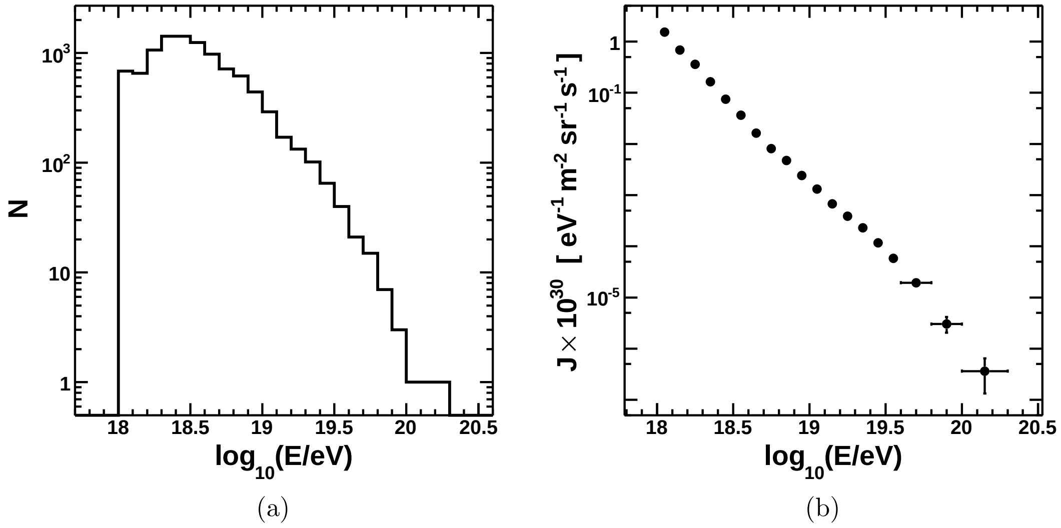

(a)

(b)

Figure 6.3: (a): Histogram of reconstructed event energies of the TA SD data in 2008/05/11 - 2011/04/25 range, using 0.1 $\log_{10}E$ binning. (b): Differential cosmic ray flux as a function of event energy calculated from the TA SD energy histogram in (a) using Equation 6.7. The sizes of the last three (highest energy) bins are 0.2, 0.2, and 0.3 in $\log_{10}E$. Error bars show the statistical uncertainties on the flux (68% confidence limits).

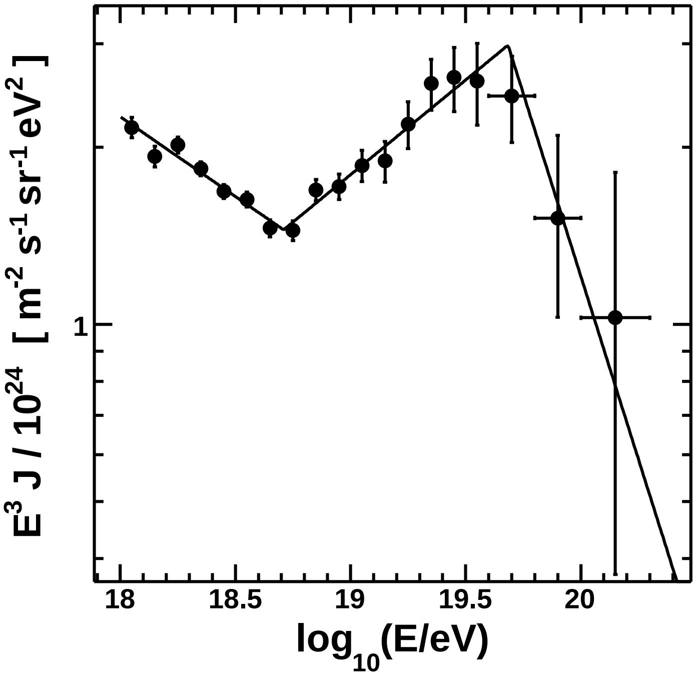

Figure 6.4: Cosmic ray flux measured by the TA SD plotted versus energy. The flux has been multiplied by E^3. The following features are now clearly visible: an ankle (change in the power law) at $E = 10^{18.7}$ eV and a suppression, which begins at $E = 10^{19.7}$ eV. Solid line shows the fit to the broken power law function (Equation 6.12) which is obtained by the fitting procedure described in Equation 6.14.

6.2.1 Broken Power Law Fit

While the physical interpretation of the result displayed in Figures 6.3b and 6.4 are a subject of the next chapter, it should be noted here that the flux has two important features: a change in the power law near $10^{18.7}$ eV that forms an ankle and a suppression starting at $\sim 10^{19.7}$ eV. Due to these features, the flux follows the shape of a broken power law (BPL) function:

$$\begin{aligned} J_{\mathrm{BPL}}(E) = K \Big[& h(E_1 - E)\, E^k + h(E - E_1) h(E_2 - E)\, E_1^{k-l} E^l \\ & + h(E - E_2) E_1^{k-l} E_2^{l-m}\, E^m \Big] , \end{aligned} \tag{6.12}$$

where h is the step function defined as:

$$h(x) = \begin{cases} 0, & x < 0 \\ 1, & x \geq 0 \end{cases} \tag{6.13}$$

In Equation 6.12, K is the overall normalization constant, E_1 is the energy where the 1^{st} break (ankle) occurs, E_2 is the energy where the suppression begins, and k, l, m are the spectral indices.

The measurement is fitted into the BPL function (Equation 6.12) using the binned likelihood method [47]. The following function is minimized:

$$\begin{aligned} \chi^2 &= -2 \sum_i \frac{\ln[P(N_i, N_{\mathrm{BPL}}(E_i))]}{\ln[P(N_i, N_i)]} \\ &= 2 \sum_i \left\{ N_{\mathrm{BPL}}(E_i) - N_i + N_i \ln[N_i / N_{\mathrm{BPL}}(E_i)] \right\} , \end{aligned} \tag{6.14}$$

where $P(N_i, N_{\mathrm{BPL}}(E_i))$ is the Poisson function of N_i (number of events in the i^{th} energy bin) with the mean (expectation) value $N_{\mathrm{BPL}}(E_i)$, which represents the number of events in the i^{th} energy bin given by the BPL function. If the numbers of events in each bin were large, then the fitting procedure would be equivalent to the usual χ^2 minimization [47], hence the choice of the variable name in Equation 6.14. The fit values in each bin are calculated as follows:

$$N_{\mathrm{BPL}}(E_i) = \lambda_i \, J_{\mathrm{BPL}}(E_i) , \tag{6.15}$$

where λ_i is the exposure calculated from Equation 6.10 and $J_{\mathrm{BPL}}(E_i)$ is the BPL function (Equation 6.12) evaluated at E_i, which is the energy that corresponds to the center of the i^{th} bin.

Figure 6.5 shows the result of applying the fitting procedure (using 0.1 $\log_{10} E$ binning) in $[10^{18.0}, 10^{20.5}]$ eV energy range, where the function in Equation 6.14 is minimized with respect to the 6 fit parameters K, E_1, E_2, k, l, m (c.f. Equation 6.12) using the MINUIT [102] software package. Also, the broken power law function that results from this fit has been superimposed on top of the data points in Figure 6.4. Finally, Table 6.1 lists the BPL fit parameters and their uncertainties. Defining the goodness of the fit by the χ^2 expression in Equation 6.14 divided

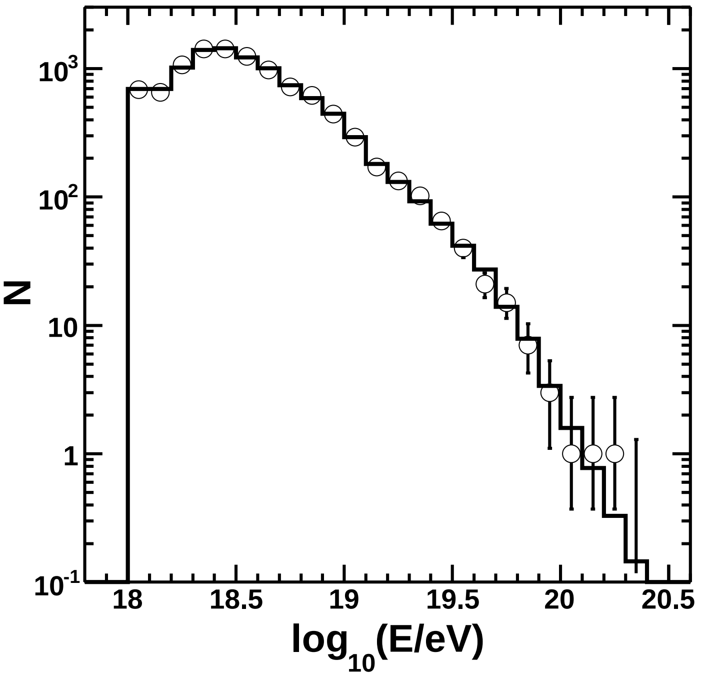

Figure 6.5: Energy histogram fitted into the broken power law function (Equation 6.12) using the minimization procedure defined by Equation 6.14. Open circles represent N_i and the solid line represents the fit values $N_{\mathrm{BPL}}(E_i)$. Feldman-Cousins 68% confidence limit error bars are attached to the data points N_i for illustration purpose only. Last bin with zero events (shown as an error bar without the data point) is included in the fit. See the text for more details.

by the number of degrees of freedom NDOF (number of bins minus the number of the fit parameters), the following value is obtained: $\chi^2/\mathrm{NDOF} = 14.2/18 \approx 0.79$. If this quantity is recalculated using only $N_i \geq 7$ bins (without changing the fit parameters), then $\chi^2/\mathrm{NDOF} = 12.6/13 \approx 0.97$.

Parameter	Value
K	$2.25 \pm 0.06 \times 10^{-30}$ $\mathrm{eV}^{-1}\mathrm{m}^{-2}\mathrm{s}^{-1}\mathrm{sr}^{-1}$
E_1	$10^{18.70\pm0.03}$ eV
E_2	$10^{19.68\pm0.09}$ eV
k	-3.27 ± 0.03
l	-2.68 ± 0.04
m	-4.2 ± 0.7

Table 6.1: Results of fitting the TA SD spectrum to a broken power law function (Equation 6.12).

6.3 Systematic Uncertainties of the Flux

6.3.1 Energy Scale

The largest source of the systematic uncertainty comes from the energy scale of the experiment. In Chapter 5, the surface detector energy obtained from the CORSIKA-based simulation was rescaled to that of the TA fluorescence detector to remove the systematic uncertainty due to the hadronic model [46] used by CORSIKA [56]. The fluorescence detector energy, however, also has a non-negligible systematic uncertainty (albeit smaller and better experimentally constrained than that of the hadronic models at energies $E > 10^{18}$ eV). Currently, the systematic uncertainty of the TA FD energy is estimated to be $\sigma_E^{\mathrm{SYS}}/E = 21\%$ [107, 108].

The uncertainty of the energy scale is propagated into the flux measurement (to a 1^{st} order) by the following argument [109, 97]. According to Equation 6.7, the dependence on the real data energy (which contains the 21 % systematic uncertainty) comes only from the N_i term. The rest of the terms, such as the bin sizes ΔE_i and the generalized exposure (Equation 6.10) are fixed *a priori* and do not depend on the data. Therefore, the fractional systematic uncertainties due to the energy scale are the same for J_i and N_i. For the (differential) flux of the form $J \propto E^{-\gamma}$, the number of events in any energy bin is given by $N = C\,E^{-(\gamma-1)}$ for some constant C, which depends only on the absolute normalization of the flux and the choice of binning. Because the energy dependence of the number of events is now contained in the $E^{-(\gamma-1)}$ term, the systematic uncertainty is propagated as:

$$\frac{\sigma_J^{\mathrm{SYS},E}}{J} = \frac{\sigma_N^{\mathrm{SYS},E}}{N} = \frac{\left|\mathrm{d}N/\mathrm{d}E\right|}{N}\sigma_E^{\mathrm{SYS}} = |\gamma - 1|\,\frac{\sigma_E^{\mathrm{SYS}}}{E} \tag{6.16}$$

Using the values in Table 6.1, the following answers are obtained: $\sigma_J^{\mathrm{SYS},E}/J \approx 49\%$, for $E < 10^{18.7}$ eV, $\sigma_J^{\mathrm{SYS},E}/J \approx 35\%$, for $10^{18.7}$ eV $< E < 10^{19.68}$ eV, and $\sigma_J^{\mathrm{SYS},E}/J \approx 67\%$, for $E > 10^{19.68}$ eV.

6.3.2 Resolution Unfolding

A systematic uncertainty due to the resolution unfolding procedure (Equations 6.7 and 6.8) occurs whenever the input distribution does not match the measured one exactly [105]. In the most general case, the (fractional) bias due to the use of the method of correction factors is evaluated as [105]:

$$\frac{b_i}{\nu_i} = \left(\frac{\mu_i^{\mathrm{MC}}}{\nu_i^{\mathrm{MC}}} - \frac{\mu_i}{\nu_i}\right), \tag{6.17}$$

where ν_i is the true number of events in the i^{th} bin for the data, μ_i is the measured number of (data) events, and ν_i^{MC} and μ_i^{MC} are the generated and measured numbers of events for the Monte-Carlo. Of course, the true numbers of evens ν_i are not known *a priori* and according to the prescription in [105], one has to generate different Monte-Carlo sets with varying assumptions on ν_i (different spectral indices in the case of the cosmic ray flux) and then estimate the systematic uncertainty using Equation 6.17, where a Monte-Carlo set with different spectral index assumptions is used in place of ν_i and μ_i.

In the case of the cosmic ray flux measurement, however, the effect of resolution (as a function of the spectral index and the energy resolution) can be evaluated directly by using Equation 6.6. The systematic uncertainty due to the resolution unfolding is estimated as follows. The spectral index of the input flux above the ankle is $\gamma_{\mathrm{INPUT}} = 2.81$ (c.f. Chapter 4), while the measured index is $\gamma_{\mathrm{MEAS}} = 2.68$ (Table 6.1). The energy resolution above the ankle is $\sigma_{\ln E} = 0.255$ (c.f. Chapter 5). Plugging these numbers into Equation 6.6, one obtains the following results for the correction due to the resolution: $C_{\mathrm{INPUT}} \approx 1.11$ (in the case of the input spectrum used by the TA SD Monte-Carlo), and $C_{\mathrm{MEAS}} \approx 1.1$ (if the TA SD Monte-Carlo were generated using the measured TA SD spectral index). It is now clear that systematic uncertainty due to the resolution unfolding is on the order of 1% in the region above the ankle ($E_1 = 10^{18.69}$ eV). Likewise, for the region below the ankle, $\gamma_{\mathrm{INPUT}} = 3.25$, $\gamma_{\mathrm{MEAS}} = 3.27$, and $\sigma_{\ln E} = 0.306$, which results in an uncertainty less than 1%. These uncertainties are negligible in comparison with that of the energy scale. For the last energy domain, $E > E_2$, the spectral index has not been measured by the TA SD accurately enough at this time (more statistics in needed). It can be speculated (using Equation 6.6) that the systematic uncertainty due to the unfolding (based on current measurement) could be on the order of 10% for $E > E_2$. If the finding ($m = -4.2$) is confirmed with more statistics in the future, then the TA SD Monte-Carlo should be re-generated using updated spectral indices.

6.3.3 Acceptance

The acceptance biases occur if there are disagreements between the data and the Monte-Carlo in quantities that are used for making the quality cuts. While most quantities in Chapter 4 agree on a $\sim 1\%$ level (the answer is obtained by counting the differences in the numbers of events between the data and MC in each bin and dividing that by the total number of events), there are important exceptions, where the peaks of the data and MC histograms do not match exactly, i.e. data and MC histograms are slightly shifted with respect to each other and simply counting the event differences in bins does not work. Two such quantities have been identified: number of good counters (counters that are a part of the event) and the fractional uncertainty on $S800$. Both of these quantities are used for making the quality cuts: $N_{\mathrm{SD}} \geq 5$ and $\sigma_{\mathrm{S800}}/S800 < 0.25$ (c.f. Chapter 5). The systematic uncertainties due to these cuts are evaluated as follows. According to Equation 6.7, the dependence on the reconstruction and quality cuts comes from the term:

$$R_i = \frac{(N_{\mathrm{REC}}^{\mathrm{DATA}})_i}{(N_{\mathrm{REC}}^{\mathrm{MC}})_i} \,. \tag{6.18}$$

The term $(N_{\mathrm{GEN}}^{\mathrm{MC}})_i$ is fixed after the MC generation and does not depend on reconstruction and cuts. Therefore, the systematic uncertainty can be readily estimated by calculating R_i with the cut (R_i^{CUT}) and without the cut ($R_i^{\mathrm{NO\,CUT}}$) and evaluating the fractional difference:

$$B_i = R_i^{\mathrm{NO\,CUT}} / R_i^{\mathrm{WITH\,CUT}} - 1 \tag{6.19}$$

Figure 6.6 shows B_i evaluated separately for the cuts on $\sigma_{S800}/S800$ and N_{SD}. As Figure 6.6a shows, the systematic change due to $\sigma_{S800}/S800$ cut is $\sim 2\%$ for $E > 10^{18.2}$ eV, and for $10^{18.0}$ eV $< E < 10^{18.2}$ eV, it is $\sim 20\%$. In the case of N_{SD} cut (Figure 6.6b), the systematic change is $\sim 6\%$ for $10^{18.0}$ eV $< E < 10^{18.1}$ eV, while for the rest of the energies, it is within $\sim 2\%$.

The systematic uncertainties due to the acceptance become larger for $E < 10^{18.2}$ eV, which is the reason for setting the minimum energy limit at $10^{18.2}$ eV in the official TA SD spectrum result [103]. Removing the $\sigma_{S800}/S800$ cut completely, however, is a large change in the acceptance at low energies. To estimate

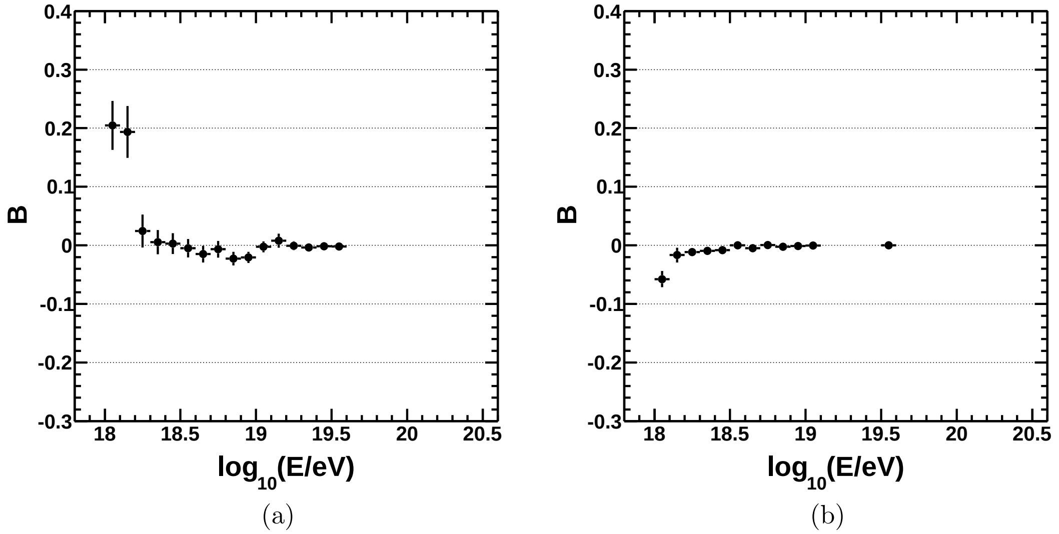

(a) (b)

Figure 6.6: Fractional change in the flux after eliminating either $\sigma_{S800}/S800 < 0.25$ or $N_{\rm SD} \geq 5$ cuts (estimated using Equation 6.19) plotted versus the (reconstructed) event energy. For $E > 10^{18.2}$ eV, the variation is within $\sim 2\%$. (a): Change in the flux when the cut on $\sigma_{S800}/S800$ is removed. (b): Change in the flux when $N_{\rm SD}$ cut is removed.

the systematic uncertainties that correspond to the 68% confidence level (C.L.), the following procedure is applied:

- Determine the values of $\sigma_{S800}/S800$ cut which reduce the numbers of accepted MC events $(N^{\rm MC}_{\rm REC})_i$ by 68% of the original (separately) in $10^{18.0}$ eV $< E < 10^{18.1}$ eV and $10^{18.1}$ eV $< E < 10^{18.2}$ eV bins.
- Determine the values of $\sigma_{S800}/S800$ cut which increase $(N^{\rm MC}_{\rm REC})_i$ by 68% of the original in $10^{18.0}$ eV $< E < 10^{18.1}$ eV and $10^{18.1}$ eV $< E < 10^{18.2}$ eV bins.
- Re-evaluate the uncertainties in the two energy bins using those values of $\sigma_{S800}/S800$ cuts (Equation 6.19) instead of removing the cut on $\sigma_{S800}/S800$ completely.

Table 6.2 shows that the 68% C.L. systematic uncertainties due to the $\sigma_{S800}/S800$ cut estimated by this procedure are 12% for $10^{18.0}$ eV $< E < 10^{18.1}$ eV and 11%

for $10^{18.1}$ eV $< E < 10^{18.2}$ eV (quoting the largest 68% C.L. uncertainties found in each energy bin). The $N_{\text{SD}} \geq 5$ cut, on the other hand, removes only 20% of

$\sigma_{S800}/S800$ cut	Energy bin	$(N^{\text{MC}}_{\text{REC}})_i$	Systematic uncertainty (68% C.L.)
0.250	$10^{18.0}$ eV $< E < 10^{18.1}$ eV	9502	-
0.324	$10^{18.0}$ eV $< E < 10^{18.1}$ eV	16015	12%
0.189	$10^{18.0}$ eV $< E < 10^{18.1}$ eV	5679	7%
0.250	$10^{18.1}$ eV $< E < 10^{18.2}$ eV	9281	-
0.277	$10^{18.1}$ eV $< E < 10^{18.2}$ eV	15685	11%
0.174	$10^{18.1}$ eV $< E < 10^{18.2}$ eV	5539	4%

Table 6.2: Estimation of the systematic uncertainty of the flux due to the $\sigma_{S800}/S800$ cut. Cuts on $\sigma_{S800}/S800$ are changed from their base value of 0.25 to induce a ~68% change in the numbers of accepted events in the two energy bins. The results are then estimated using Equation 6.19.

events when the rest of the cuts are in place. Therefore, it is appropriate to take the results of Figure 6.6b in this case.

6.4 Final Result

Table 6.3 quotes the answers for the cosmic ray flux measured by the Telescope Array surface detector, where the statistical and systematic uncertainties are evaluated separately for each bin. Feldman-Cousins method [106] is used for determining the statistical uncertainties (68% C.L.) and the systematic uncertainties are evaluated by the procedure described in the previous section. The individual contributions to the systematic uncertainty are added up in quadratures, for each energy bin:

$$\sigma_{\text{SYS}} = \sqrt{\sigma^2_{\text{UNF}} + \sigma^2_{\text{ACC}}}\,, \tag{6.20}$$

where σ_{SYS} is the combined systematic uncertainty on the flux bins (excluding that of the energy scale), σ_{UNF} is the systematic uncertainty due to the unfolding of the resolution, and σ_{ACC} is the systematic uncertainty due to the acceptance.

$\log_{10}(E/\text{eV})$	b	N	J	$\sigma^{\text{STAT}}_{\text{LOWER}}$	$\sigma^{\text{STAT}}_{\text{UPPER}}$	σ^{SYS}
18.05	0.1	685	1.53E-30	2.15E-31	2.15E-31	2.06E-31
18.15	0.1	653	6.85E-31	8.17E-32	8.17E-32	7.69E-32
18.25	0.1	1067	3.59E-31	1.57E-32	1.57E-32	1.08E-32
18.35	0.1	1421	1.64E-31	6.67E-33	6.67E-33	4.92E-33
18.45	0.1	1422	7.51E-32	3.06E-33	3.06E-33	2.25E-33
18.55	0.1	1246	3.65E-32	1.54E-33	1.54E-33	1.10E-33
18.65	0.1	977	1.64E-32	7.32E-34	7.32E-34	4.91E-34
18.75	0.1	718	8.12E-33	3.98E-34	3.98E-34	2.44E-34
18.85	0.1	619	4.77E-33	2.46E-34	2.46E-34	1.43E-34
18.95	0.1	441	2.42E-33	1.41E-34	1.41E-34	7.27E-35
19.05	0.1	292	1.32E-33	8.97E-35	8.97E-35	3.95E-35
19.15	0.1	171	6.73E-34	5.73E-35	5.73E-35	2.02E-35
19.25	0.1	133	3.89E-34	3.72E-35	3.72E-35	1.17E-35
19.35	0.1	102	2.29E-34	2.38E-35	2.38E-35	6.86E-36
19.45	0.1	65	1.17E-34	1.51E-35	1.51E-35	3.52E-36
19.55	0.1	40	5.80E-35	9.37E-36	9.37E-36	1.74E-36
19.70	0.2	36	1.94E-35	3.83E-36	3.83E-36	2.02E-36
19.90	0.2	10	3.03E-36	1.02E-36	1.19E-36	3.14E-37
20.15	0.3	3	3.64E-37	2.34E-37	2.82E-37	3.78E-38

Table 6.3: Cosmic ray flux measured by the TA surface detector. For each bin in $\log_{10}E$, the following quantities are tabulated: $\log_{10}(E/\text{eV})$ is the energy of the bin center, b is the bin size, N is the number of events, J is the flux in $[\text{eV}^{-1}\,\text{s}^{-1}\,\text{m}^{-2}\,\text{sr}^{-1}]$, $\sigma^{\text{STAT}}_{\text{LOWER}}$ and $\sigma^{\text{STAT}}_{\text{UPPER}}$ are the statistical uncertainties on the flux that correspond to the lower and upper 68% confidence limits, and σ^{SYS} is the estimated systematic uncertainty of each bin. All uncertainties are in $[\text{eV}^{-1}\,\text{s}^{-1}\,\text{m}^{-2}\,\text{sr}^{-1}]$.

Chapter 7

Conclusions

7.1 Comparison with Other Experiments

7.1.1 Comparison with the High Resolution Fly's Eye

Figure 7.1 shows the comparison of the cosmic ray energy spectra between the Telescope Array surface detector (Chapter 6) and the High Resolution Fly's Eye results [11]. The agreement between these results, which have been produced by different detection techniques, is unprecedented. The HiRes experiment uses fluorescence measurements made in monocular mode, which consist of sampling the atmospheric fluorescence light profile of the showers, while the TA SD samples the shower front particles on the ground by the scintillator counters. In fact, if the TA SD flux is compared with the broken power law function (Equation 6.12) reported by HiRes (using the fit parameters from [11]), then even without changing the overall normalization constant K, the reduced χ^2 of the comparison is $25.6/19 \approx 1.3$, in $E > 10^{18}$ eV range (Figure 7.2). Both experiments clearly see an ankle feature near $E_1 \simeq 10^{18.7}$ eV and a suppression near $E_2 \simeq 10^{19.7}$ eV. Actual values of the broken power law fit parameters are quoted for each experiment in Table 7.1, from which it can be seen that the HiRes and TA SD results are well within their (statistical) uncertainties.

It should be noted that important similarities exist between the TA SD and HiRes measurement techniques. One such similarity is that both experiments are using the energy scale determined by the fluorescence detector measurements

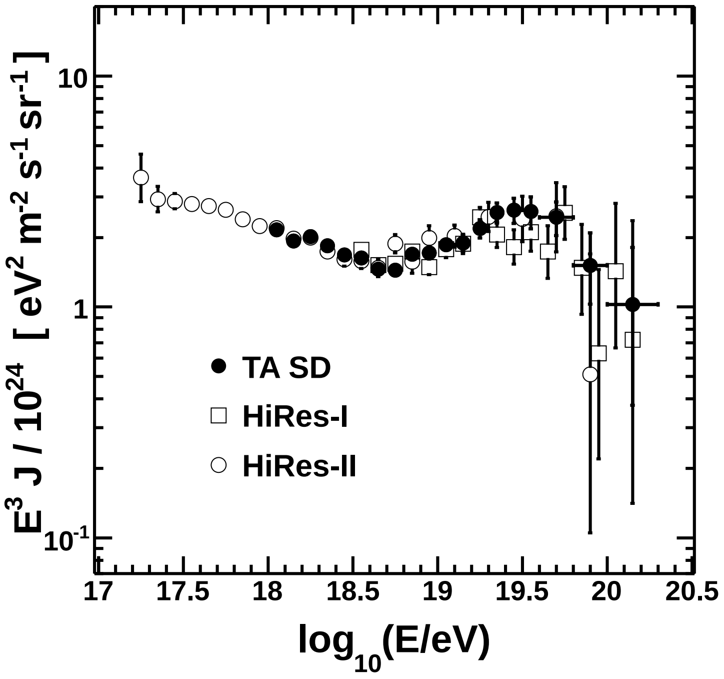

Figure 7.1: Comparison of the TA SD (Chapter 6) and HiRes [11] cosmic ray flux results. The results are multiplied by E^3 to emphasize the spectral features.

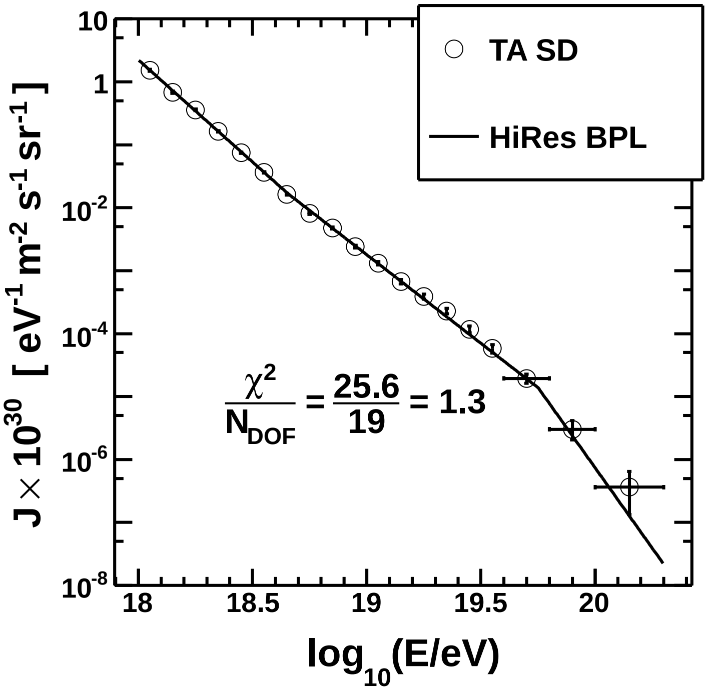

Figure 7.2: χ^2 (per degree of freedom) comparison of the TA SD flux (open circles) and the broken power law function (BPL) fit result reported by HiRes in [11] (solid line).

rather than hadronic models. In the case of the TA SD, the energy scale (c.f. Chapter 5) normalization constant was established by simultaneously comparing the energies of well reconstructed SD events with the TA Middle Drum [110] and the TA Black Rock Mesa and Long Ridge [107, 108] fluorescence detectors, *before* the TA SD energy spectrum was produced. All three fluorescence detectors of TA are in a good agreement among each other, and at the same time it has also been demonstrated that the TA Middle Drum energy scale is in a good agreement with that of the HiRes experiment [110]. Another similarity is that both HiRes and the TA SD use detailed Monte-Carlo methods for determining the detector acceptance as well as unfolding the effects of the resolution.

The consistency seen in the two measurements proves the reliability of the cosmic ray energy spectrum result in $E > 10^{18}$ eV domain and confirms the existence of the suppression near $E \sim 10^{19.7}$ eV.

7.1.2 Comparison with the Akeno Giant Air Shower Array

Figure 7.3a shows the comparison of the TA SD spectrum with the Akeno Giant Air Shower Array (AGASA) result [16]. The two results results generally do not agree. First, there is a clear shift in the overall normalization of the flux, which may be attributed to the energy scale difference between the experiments, and second, most importantly, the TA SD is reporting the suppression at $E \sim 10^{19.7}$ eV, while the AGASA flux continues like E^{-3} beyond this point with no visible break. The former difference can be remedied for by matching the energy scales of the two experiments. Following the suggestion to use the region near the ankle (E_1 in Equation 6.12) as the calibration point for the experiments [13], we find that this can be achieved if the AGASA energy scale were reduced by $\sim 28\%$. The $E^3\,J$ plot of the AGASA experiment can be rescaled (in a simple way, without taking into account the exposure of the experiment) as follows. Let ϵ denote the fractional change in energy (-0.28 in this case), so that the new (rescaled) energy E' is expressed in terms of old energy E as $E' = (1+\epsilon)E$. This means that the new (rescaled) flux J' can be expressed as $J'(E') = (1+\epsilon)^{-1} J(E)$, where an additional factor of $(1+\epsilon)^{-1}$ appears due to $J \propto \mathrm{d}N/\mathrm{d}E$ dependence. The re-scaling relation for the quantity $E^3 J$ then becomes:

$$E'^3 \, J'(E') = (1+\epsilon)^2 E^3 J(E) \,, \tag{7.1}$$

Figure 7.3b shows the comparison of the TA SD and the AGASA results after the AGASA points have been rescaled using Equation 7.1 with $\epsilon = -0.28$. If one were to match the spectrum regions only above the ankle, then the AGASA energy scale would need to be reduced only by $\sim 20\%$ (but this $\sim 8\%$ difference in re-scaling does not affects the conclusion stated below). From the results in Figure 7.3, it can be concluded that the TA SD does not confirm the continuation of the flux beyond $10^{19.7}$ eV, reported by the AGASA [16], and taking into account the energy scale difference between the two experiments (reducing the energy scale of the AGASA experiment) does not resolve this discrepancy.

7.1.3 Comparison with the Pierre Auger Observatory

The TA SD energy spectrum is also compared with the result of the Pierre Auger Observatory (PAO) [17]. The PAO is a new experiment in the southern hemisphere and like TA, it is a hybrid experiment that uses combined techniques of the FD and SD observations. The energy scale of this experiment is also calibrated using the fluorescence detector. Figure 7.4a shows the comparison of the results. According to [17], the PAO combines the energy spectrum measured by the surface detector (mostly at high energies) with that measured in hybrid mode (at lower energies). The PAO measurement also has been fitted into to the broken power law function (Equation 6.12), and the official results of this

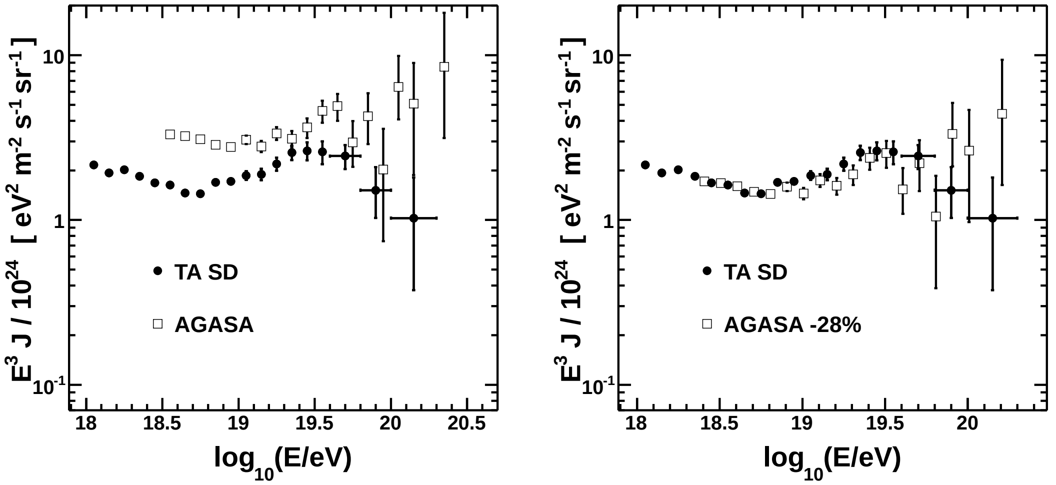

(a) (b)

Figure 7.3: Comparison of the TA SD (Chapter 6) and the AGASA [16] cosmic ray flux results. (a): TA SD superimposed on top of the official AGASA energy spectrum result. (b): Comparison of the TA SD and AGASA results after the AGASA energy scale has been reduced by 28%.

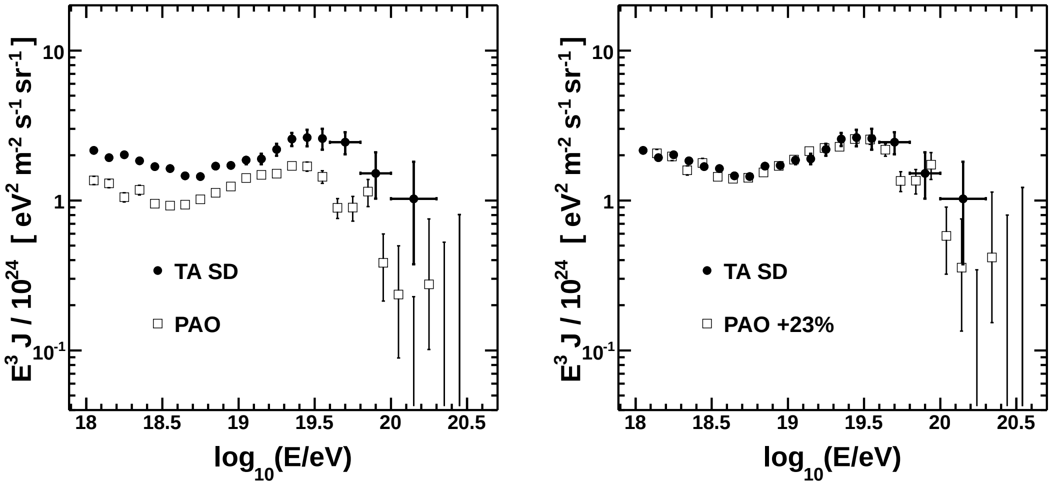

(a) (b)

Figure 7.4: Comparison of the TA SD (Chapter 6) and the Pierre Auger Observatory (PAO) [17] cosmic ray flux results. (a): TA SD superimposed on top of the official PAO energy spectrum result. This version of the PAO spectrum is a combination of the surface detector and hybrid (surface detector and SD) measurements. (b): Comparison of these results after the Pierre Auger energy scale has been increased by 23%.

fit [17] are included in Table 7.1 as well. From the results of the fit, it is clear that there is an energy scale difference between the TA and PAO experiments: the TA SD ankle is located at $E_1 = 10^{18.7 \pm 0.03}$ eV, while the PAO reports the position of the ankle at $E_1 = 10^{18.61 \pm 0.01}$ eV. Since both experiments calibrate their energies using the fluorescence detectors, the difference must be due to the systematic uncertainties in the energy determination by the FD measurements, which are 21% for TA (c.f. Chapter 6) and 22% for PAO [17]. If the energy scales of the experiment are matched according to the method of [13] (using the ankle as the calibration point), one finds that the PAO energies should be increased by $10^{18.7-18.61} - 1 \approx 23\%$ in order to match the TA SD. Figure 7.4b shows the comparison of the TA SD and PAO spectrum after the energy scale of the later has been increased by 23% (using Equation 7.1 with $\epsilon = 0.23$).

As seen in Figure 7.4b, the results line up well in the region near the ankle (and up to $E \sim 10^{19.5}$ eV) as anticipated: the spectral indices of the TA SD and PAO are within their uncertainties (Table 7.1) and the energy scale has been adjusted so that the position of the ankle $E_1 = 10^{18.7}$ eV is the same for both experiments. The energy of the second break, on the hand, appears to be different between the two experiments. However, a quantitative comparison shows that this difference is not statistically significant: the TA SD finds $E_2^{\mathrm{TASD}} = 10^{19.68 \pm 0.09}$, while the PAO now has (after increasing the PAO energies by 23%) $E_2^{\mathrm{PAO,RESCALED}} = 10^{19.55 \pm 0.03}$ eV, which is $\sim 26\%$ lower than that of the TA SD. If one combines the (statistical) uncertainties on E_2 of the two experiments in quadrature, one obtains $\sigma_{E_2}^{\mathrm{TA,PO}} = 1 - 10^{-\sqrt{0.09^2 + 0.03^2}} \approx 20\%$ (percent of the E_2 determined by the TA SD).

The overall agreement between the results reported by the TA SD and the Pierre Auger Observatory reaffirms the validity of the measurement. In particular, the occurrence of the second break E_2, first observed by the HiRes [11] fluorescence detectors operating in monocular mode, is now confirmed by the two hybrid experiments, which are viewing the sky separately in the North and South hemispheres of the Earth.

Parameter	TA SD	HiRes	PAO
$\log_{10}(E_1/\mathrm{eV})$	18.70 ± 0.03	18.65 ± 0.05	18.61 ± 0.01
$\log_{10}(E_2/\mathrm{eV})$	19.68 ± 0.09	19.75 ± 0.04	19.46 ± 0.03
k	-3.27 ± 0.03	-3.25 ± 0.01	-3.26 ± 0.04
l	-2.68 ± 0.04	-2.81 ± 0.03	-2.59 ± 0.02
m	-4.2 ± 0.7	-5.1 ± 0.7	-4.3 ± 0.2

Table 7.1: Comparison of the results of the fits to the broken power law function (Equation 6.12) among different cosmic ray experiments. Only the parameters describing the shape of the spectrum are quoted (most experiments do not officially quote the overall normalization constant K).

7.2 Astrophysical Interpretation

A description that currently fits the cosmic ray data (collected in the Northern hemisphere) best is that of the extra-galactic primary protons propagating on the cosmic microwave background (CMB) [13]. The results of HiRes experiment [2] indicate that the cosmic ray mass composition is predominantly light (protons) above $E > 10^{18}$ eV, with a slight mixture of iron in 10^{18} eV $< E < 10^{18.2}$ eV range. Furthermore, the preliminary results of the TA experiment [4] also confirm the proton mass composition above $10^{18.2}$ eV.

In [13], it is shown that a simple description using extra-galactic protons generated by the uniformly distributed sources simultaneously explains the observed spectrum shape features for $E > 10^{18}$ eV. In this model, the ankle near $10^{18.7}$ eV is caused by the pair production of the CMB photons in the vicinity of the energetic proton (energy loss due to this interaction becomes comparable to that due to the universe expansion), while the suppression at $10^{19.7}$ eV is explained by the photo-pion production via the Δ-resonance [30, 31], which is also called the Greisen-Zatsepin-Kuzmin (GZK) cutoff. The latter is a very efficient energy loss mechanism that produced a steep suppression in the measured cosmic ray spectrum.

7.2.1 $E_{1/2}$ Value Measured by the TA SD

To properly quantify the energy of the cutoff, it has been suggested in [13] to use the energy $E_{1/2}$, where the integral flux $J_>$ (Equation 6.2) falls to 1/2 of its value in the absence of the second break E_2 (Equation 6.12). In [13], it is argued that the value $E_{1/2}$ is less sensitive to the power law of the energy spectrum produced by the sources, a quantity which is a free parameter of the model. Using the results of the broken power law (BPL) fit in Chapter 6 (Equation 6.12), it is straightforward to calculated the $E_{1/2}$:

$$\log_{10}E_{1/2} = \log_{10}\left(E_2\right) + \frac{1}{l-m}\log_{10}\left(2\frac{l+1}{m+1}\right) \tag{7.2}$$

Figure 7.5 illustrates the calculation. Using Equation 7.2 and propagating the (statistical) uncertainties, the following answer is obtained from the measurement of the TA SD:

$$\log_{10}(E_{1/2}^{\mathrm{TA\,SD}}/\mathrm{eV}) = 19.69 \pm 0.10\,(\mathrm{stat}) \pm 0.083\,(\mathrm{sys})\,, \tag{7.3}$$

where the statistical and systematic uncertainties are quoted separately. According to [13], the extra-galactic proton model prediction of $E_{1/2}$ is $10^{19.72}$ eV. Clearly, the TA SD measurement is well within the experimental uncertainties of this value.

7.2.2 Significance of the Suppression Measured by the TA SD

Lastly, the statistical significance of the GZK suppression seen in the TA SD data is evaluated. Suppose that the observed flux continues with the power law

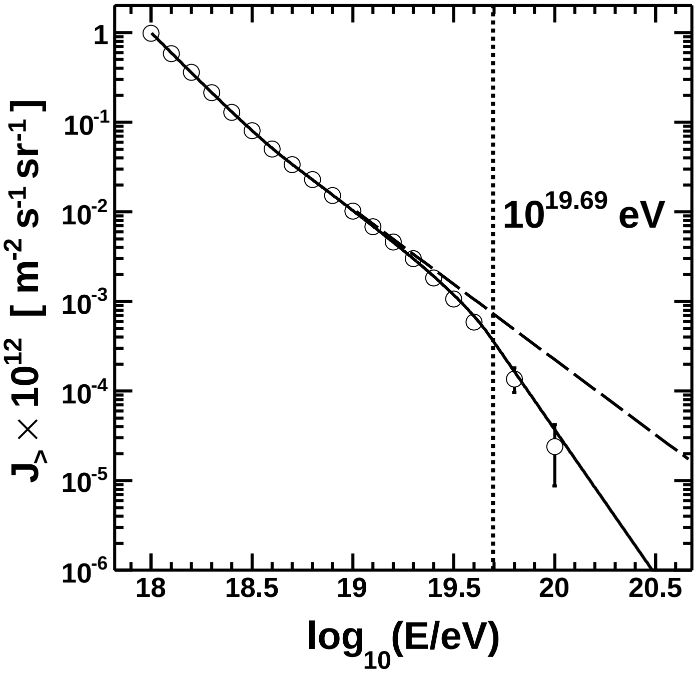

Figure 7.5: Determination of $E_{1/2}$ value from the TA SD flux measurement. Integral flux (Equation 6.2) is plotted as a function of energy. Points with error bars are the data, solid line is the result of the fit to the BPL function (Equation 6.12), the dashed line is the extension of the spectral index l beyond the second break E_2, and the dotted line shows the energy $E_{1/2} = 10^{19.69\pm0.10}$ eV, where the integral flux (solid line) becomes 1/2 of that in the absence of the cutoff (dashed line).

l (Equation 6.12) beyond the break E_2 and assume that the suppression seen in the data is a statistical fluctuation. Then the probability of the continued flux is determined as follows. The number of expected events N_{EXP} without the break at E_2 is estimated by extending the broken power law (BPL) fit beyond the second break. This means that the same values of the parameters K, E_1, l, k as those obtained by the BPL fit in Chapter 6 are used but now with $E_2 \to \infty$ limit. As Figure 7.6 shows, the number of events above $E_2 = 10^{19.7}$ eV obtained by this extension is $N_{\mathrm{EXP}} \simeq 54.9$, while the number of events observed by the TA SD is $N_{\mathrm{OBS}} = 28$. Therefore, the probability of the continued flux (or the *chance probability* of the suppression) is:

$$p_{\mathrm{CH}}^{\mathrm{SUPPRESSION}} = \sum_{i=0}^{i=28} P(54.9, i) \approx 4.75 \times 10^{-5}, \tag{7.4}$$

where $P(\mu, n) = \mu^n \, e^{-\mu} / n!$ is the (discrete) Poisson distribution. Using the standard notation of the particle physics [47], one finds that this chance probability amounts to approximately $3.9\,\sigma$.

To summarize, we have measured the flux of ultra-high energy cosmic rays using the surface detector of the Telescope Array experiment. This work effectively combined the experimental techniques developed by the HiRes and AGASA experiments. While using an AGASA-like array of scintillation counters and AGASA methods of reconstructing basic event information such as geometry and lateral distribution, at the same time, the energy scale was established using the fluorescence detectors. We have also introduced a new Monte-Carlo technique and evaluated the detector acceptance and resolution with an unprecedented accuracy. This enabled a HiRes-style data and Monte-Carlo analysis with an excellent control of the resolution and systematic errors. The occurrence of the GZK cutoff is now confirmed, for the first time, by an array of scintillation counters.

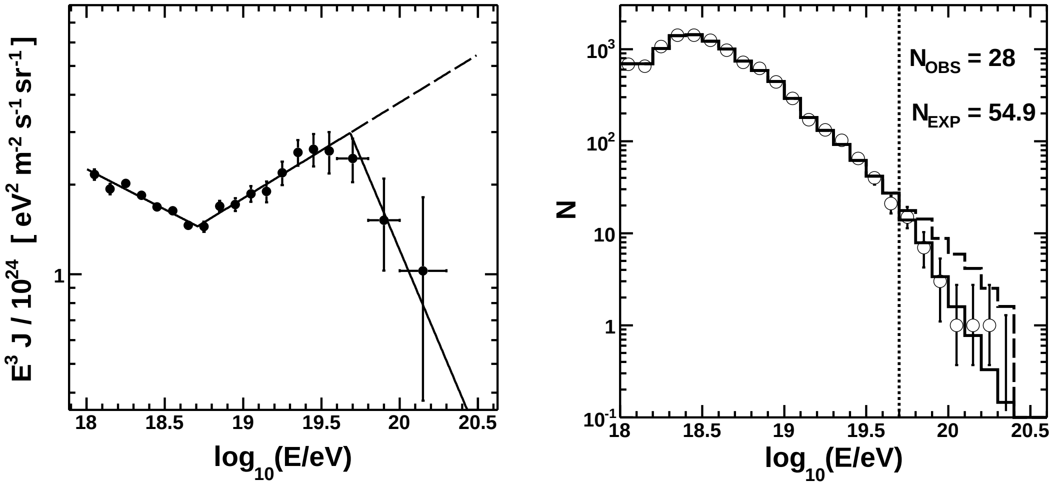

(a) (b)

Figure 7.6: TA SD spectrum fitted to the broken power law function (Equation 6.12). Solid lines in both figures show the actual result of the fit, while the dashed lines represent the extension of the power law l beyond the second break E_2, as if the suppression did not exist (dashed lines show the limit $E_2 \rightarrow \infty$). Points with error bars represent the data. (a): TA SD flux multiplied by E^3. (b): Energy histogram. If the suppression at E_2 (dotted line) did not exist and the flux continued with the power law $l = -2.68$, one would expect $N_{\mathrm{EXP}} \simeq 54.9$ events (Poisson average) above $E_2 = 10^{19.7}$ eV, while the number of observed events in the TA SD data between May 11, 2008 and April 25, 2011 is $N_{\mathrm{OBS}} = 28$.

Chapter 8

Appendix

8.1 Acronyms

ADC Analog-to-Digital Converter

AGASA Akeno Giant Air Shower Array (cosmic ray experiment)

AGN Active Galactic Nucleus

ASCII American Standard Code for Information Exchange

BPL Broken Power Law (function characterizing the CR flux above 1 EeV)

BR Black Rock Mesa (TA communication tower or a fluorescence detector)

CLF Central Laser Facility

CMB Cosmic Microwave Background

CR Cosmic Rays

CT Communication/Collecting Tower (used by the surface detector)

CPU Central Processing Unit

DAQ Data Acquisition

DST Data Storage Tape (data format)

EM Electromagnetic (component or process, etc)

FADC Flash Analog-to-Digital Converter

FD Fluorescence Detector

FPGA Field-Programmable Gate Array

GEANT Geometry And Tracking (HEP software)

GMF Galactic Magnetic Field (of the Milky Way galaxy)

GPS Global Positioning System

GRB Gamma Ray Burst

GZK Greisen-Zatsepin Kuz'min (limit)

HEP High Energy Physics

HiRes High Resolution Fly's Eye Experiment (cosmic ray experiment)

IEE Institute of Electrical and Electronics Engineering

LAN Local Area Network

LDF Lateral Distribution Function

LR Long Ridge (TA communication tower or a fluorescence detector)

MD Middle Drum (TA fluorescence detector)

MIP Minimum Ionizing Particle (energy deposition unit)

NKG Nishimura-Kamata-Greisen (electron lateral distribution function)

MPV Most Probable Value (of a distribution)

MST Mountain Standard Time

PMT Photomultiplier Tube

PPS Pulse Per Second (emitted by the GPS receiver)

RMS Root-Mean-Square (of a distribution)

SD Surface Detector

SK Smelter Knolls (TA communication tower)

SNR Supernova Remnant

TA Telescope Array (cosmic ray experiment)

TDC Time-to-Digital Converter

UHECR Ultra High Energy Cosmic Rays

UV Ultra-Violet (light)

UTC Universal Time Coordinated

VEM Vertical Equivalent Muon (energy deposition unit)

WLAN Wireless Local Area Network

WLS Wavelength Shifter (optical fiber)

Bibliography

[1] T. Abu-Zayyad et al. The surface detector array of the Telescope Array experiment. *Submitted to Nucl. Instrum. Meth.*, 2012.

[2] R. U. Abbasi et al. Indications of proton-dominated cosmic ray composition above 1.6 EeV. *Phys. Rev. Lett.*, 104:161101, 2010.

[3] J. Abraham et al. Measurement of the Depth of Maximum of Extensive Air Showers above 10^{18} eV. *Phys.Rev.Lett.*, 104:091101, 2010.

[4] Y. Tameda et al. Measurement of UHECR Mass Composition by TA FD Stereo. In *Proceedings of the 32*$^{\text{nd}}$ *ICRC*, Beijing, 2011.

[5] M. Kachelriess, Pasquale Dario Serpico, and M. Teshima. The Galactic magnetic field as spectrograph for ultrahigh energy cosmic rays. *Astropart.Phys.*, 26:378–386, 2006.

[6] P.G. Tinyakov and I.I. Tkachev. Correlation function of ultrahigh energy cosmic rays favors point sources. *JETP Lett.*, 74:1–5, 2001. Replaced with the version accepted for publication in JETP Lett.

[7] R. U. Abbasi et al. Analysis of Large-scale Anisotropy of Ultra-high Energy Cosmic Rays in HiRes Data. *ApJ*, 713(1):L64, 2010.

[8] M. Takeda, N. Hayashida, K. Honda, N. Inoue, K. Kadota, et al. Small-scale anisotropy of cosmic rays above 10^{19} eV observed with the akeno giant air shower array. *Astrophys.J.*, 522:225–237, 1999.

[9] Simona Mei, John Blakeslee, Patrick Cote, John Tonry, Michael J. West, et al. The ACS Virgo Cluster Survey. 13. SBF Distance Catalog and the Three-Dimensional Structure of the Virgo Cluster. *Astrophys.J.*, 655:144–162, 2007.

[10] M. Kachelriess. Lecture notes on high energy cosmic rays. 2008.

[11] R. U. Abbasi et al. First observation of the greisen-zatsepin-kuzmin suppression. *Phys. Rev. Lett.*, 100:101101, 2008.

[12] S. Yoshida et al. The cosmic ray energy spectrum above 3×10^{18} eV measured by the Akeno Giant Air Shower Array. *Astropart. Phys.*, 3:105–124, 1995.

[13] V. Berezinsky, A.Z. Gazizov, and S.I. Grigorieva. On astrophysical solution to ultrahigh-energy cosmic rays. *Phys.Rev.*, D74:043005, 2006.

[14] Todor Stanev, Ralph Engel, Anita Mucke, Raymond J. Protheroe, and Jorg P. Rachen. Propagation of ultrahigh-energy protons in the nearby universe. *Phys.Rev.*, D62:093005, 2000. 12 pages, 9 figures, ReVTeX. submitted to Physical Review D.

[15] B. T. Stokes, Ivanov D., et al. Dethinning extensive air shower simulations in CORSIKA. 2011. Submitted to Astroparticle Physics.

[16] K. Shinozaki and M. Teshima. AGASA results. *Nucl. Phys. Proc. Suppl.*, 136:18–27, 2004.

[17] F. Salamida et al. Update on the measurement of the CR energy spectrum above 10^{18} eV made using the Pierre Auger Observatory. In *Proceedings of the 32*$^{\text{nd}}$ *ICRC*, Beijing, 2011.

[18] V. F. Hess. Über Beobachtungen der durchdringenden Strahlung bei sieben Freiballonfahrten. *Z. Phys.*, 13:1084, 1912.

[19] W. F. G. Swann. The History of Cosmic Rays. *AM. J. Phys.*, 29:12:811, 1961.

[20] V. L. Ginzburg. Cosmic ray astrophysics (history and general review). *Physics-Uspekhi*, 39(2):155–168, 1996.

[21] J. Clay. Ultra radiation (penetrating radiation). III. Annual variation and variation with the geographical latitude. *Amsterdam Proc.*, 33:711, 1930.

[22] P. A. M. Dirac. The Quantum theory of electron. 2. *Proc. Roy. Soc. Lond.*, A118:351, 1928.

[23] C. D. Anderson. THE POSITIVE ELECTRON. *Phys. Rev.*, 43:491–494, 1933.

[24] S. H. Neddermeyer and C. D. Anderson. NOTE ON THE NATURE OF COSMIC RAY PARTICLES. *Phys. Rev.*, 51:884–886, 1937.

[25] Pierre Auger and Roland Maze. Extensive cosmic showers in the atmosphere. *Compt. Rend. Acad. Sci. (Ser. II)*, 207:228–229, 1938.

[26] Bruno Rossi and Kenneth Greisen. Cosmic-ray theory. *Rev. Mod. Phys.*, 13:240–309, 1941.

[27] John Linsley. Evidence for a primary cosmic-ray particle with energy 10**20-eV. *Phys. Rev. Lett.*, 10:146–148, 1963.

[28] TeVI Group. Design Report Tevatron 1 project. FERMILAB-DESIGN-1984-01.

[29] Lyndon R Evans. The large hadron collider project. oai:cds.cern.ch:313675. (LHC-Project-Report-53. CERN-LHC-Project-Report-53):10 p, Sep 1996.

[30] K. Greisen. End of the cosmic-ray spectrum? *Phys. Rev. Lett.*, 16:748, 1966.

[31] G. T. Zatsepin and V. A. Kuzmin. Upper limit of the spectrum of cosmic rays. *JETP Lett.*, 4:78–80, 1966.

[32] G. Gamow. The origin of elements and the separation of galaxies. *Phys. Rev.*, 74:505–506, Aug 1948.

[33] Ralph A. Alpher and Robert C. Herman. On the relative abundance of the elements. *Phys. Rev.*, 74:1737–1742, Dec 1948.

[34] Arno A. Penzias and Robert Woodrow Wilson. A Measurement of excess antenna temperature at 4080- Mc/s. *Astrophys. J.*, 142:419–421, 1965.

[35] P. Noterdaeme, P. Petitjean, R. Srianand, C. Ledoux, and S. Lopez. The evolution of the Cosmic Microwave Background Temperature: Measurements of TCMB at high redshift from carbon monoxide excitation. 2010.

[36] Luis Anchordoqui and Haim Goldberg. Footprints of super-GZK cosmic rays in the Pilliga State Forest. *Phys. Lett.*, B583:213–221, 2004.

[37] M. I. Pravdin et al. The cosmic rays energy spectrum of the Yakutsk EAS Array. In *Proceedings of the 31*$^{\mathrm{st}}$ *ICRC*, Łódź, 2009.

[38] Alan N. Bunner. COSMIC RAY DETECTION BY ATMOSPHERIC FLUORESCENCE. NYO-3038-5.

[39] D. J. Bird et al. Evidence for correlated changes in the spectrum and composition of cosmic rays at extremely high-energies. *Phys. Rev. Lett.*, 71:3401–3404, 1993.

[40] M. Takeda. Energy spectrum above 3 x 10**18-eV observed with AGASA. Prepared for 26th International Cosmic Ray Conference (ICRC 99), Salt Lake City, Utah, 17-25 Aug 1999.

[41] D. R. Bergman et al. Fits of the HiRes spectrum to astrophysical models. Prepared for 28th International Cosmic Ray Conferences (ICRC 2003), Tsukuba, Japan, 31 Jul - 7 Aug 2003.

[42] P. Sokolsky. *Introduction to Ultra High Energy Physics.* Addison-Wesley, 1989.

[43] T. Abu-Zayyad. *The Energy Spectrum of Ultra High Energy Cosmic Rays.* PhD dissertation, University of Utah, Dept. of Physics & Astronomy & High Energy Astrophysics Institute, Salt Lake City, UT, 2000.

[44] K. Kim. *Cosmic Neutrino Events in HiRes I Detector.* PhD dissertation, University of Utah, Dept. of Physics & Astronomy & High Energy Astrophysics Institute, Salt Lake City, UT, 2002.

[45] B. T. Stokes. *A Search for Anisotropy in the Arrival Directions of Ultra High Energy Cosmic Rays.* PhD dissertation, University of Utah, Dept. of Physics & Astronomy & High Energy Astrophysics Institute, Salt Lake City, UT, 2000.

[46] S. Ostapchenko. QGSJET-II: Towards reliable description of very high energy hadronic interactions. *Nucl. Phys. Proc. Suppl.*, 151:143–146, 2006.

[47] K. Nakamura et al. Review of particle physics. *J.Phys.G*, G37:075021, 2010.

[48] W. Ralph Nelson, H. Hirayama, and David W. O. Rogers. The EGS4 code system. Technical Report 0265, SLAC, 1985.

[49] C. Song et al. Energy estimation of UHE cosmic rays using the atmospheric fluorescence technique. *Astropart. Phys.*, 14:7–13, 2000.

[50] John Linsley. Spectra, anisotropies and composition of cosmic rays above 1000-GeV. Rapporteur's talk given at 18th Int. Cosmic Ray Conf., Bangalore, India, Aug 22 - Sep 3, 1983.

[51] Gaisser T. K. and A. M. Hillas. . In *Proceedings of the 15$^{\text{th}}$ ICRC*, volume 8, page 353, Plovdiv, Bulgaria, 1977.

[52] T. K. Gaisser. *Cosmic Rays and Particle Physics.* Cambridge University Press, 1990.

[53] F. Kakimoto, E.C. Loh, M. Nagano, H. Okuno, M. Teshima, et al. A Measurement of the air fluorescence yield. *Nucl.Instrum.Meth.*, A372:527–533, 1996.

[54] R. Abbasi, T. Abu-Zayyad, K. Belov, J. Belz, Z. Cao, et al. Air fluorescence measurements in the spectral range 300-420 nm using a 28.5-GeV electron beam. *Astropart.Phys.*, 29:77–86, 2008.

[55] Hernan Wahlberg. Mass composition studies using the surface detector of the Pierre Auger Observatory. *Nucl.Phys.Proc.Suppl.*, 196:195–198, 2009.

[56] D. Heck, G. Schatz, T. Thouw, J. Knapp, and J. N. Capdevielle. CORSIKA: A Monte Carlo code to simulate extensive air showers. Technical Report 6019, FZKA, 1998.

[57] Soonyoung Roh et al. Comparison of CORSIKA and COSMOS simulations. *AIP Conf. Proc.*, 1367:177–180, 2011.

[58] S. J. Sciutto. Air shower simulations with the AIRES system. 1999.

[59] A. Ferrari, P. R. Sala, A. Fasso, and J. Ranft. FLUKA: A multi-particle transport code (Program version 2005). Technical Report 2005-010, CERN, 2005.

[60] T. Abu-Zayyad et al. Search for Anisotropy of Ultra-high Energy Cosmic Rays with the Telescope Array Experiment. *To be submitted to Astrophys. J.*, 2012.

[61] M. Nagano et al. ENERGY SPECTRUM OF PRIMARY COSMIC RAYS BETWEEN 10**14.5-eV AND 10**18-eV. *J. Phys.*, G10:1295, 1984.

[62] M. Amenomori et al. The all-particle spectrum of primary cosmic rays in the wide energy range from 10^{14} eV to 10^{17} eV observed with the Tibet-III air-shower array. *Astrophys. J.*, 678:1165–1179, 2008.

[63] D. J. Bird et al. The Cosmic ray energy spectrum observed by the Fly's Eye. *Astrophys. J.*, 424:491–502, 1994.

[64] Elena Cantoni, W.D. Apel, J.C. Arteaga-Velazquez, K. Bekk, M. Bertaina, et al. The measurement of the cosmic ray primary energy spectrum at 10**16 to 10**18-eV with the KASCADE-Grande experiment. *Nucl.Phys.Proc.Suppl.*, 212-213:68–73, 2011.

[65] M. S. Longair. *High Energy Astrophysics.* Cambridge University Press, 2011.

[66] Alexander Kusenko. Ultrahigh-energy nuclei, photons, and magnetic fields. *Nucl.Phys.Proc.Suppl.*, 212-213:194–200, 2011.

[67] Yuichiro Tameda et al. Trigger electronics of the new fluorescence detectors of the Telescope Array experiment. *Nucl. Instrum. Meth.*, A609:227–234, 2009.

[68] D. Rodriguez. *The Telescope Array Middle Drum Monocular Energy Spectrum and A Search For Coincident Showers Using High Resolution Fly's Eye Hires-1 Monocular Data.* PhD dissertation, University of Utah, Dept. of Physics & Astronomy & High Energy Astrophysics Institute, Salt Lake City, UT, 2011.

[69] S. R. Stratton et al. Using the Monte Carlo Technique in the Observation of Fluorescence from UHECRs. In *Proceedings of the 32*$^{\text{nd}}$ *ICRC*, Beijing, 2011.

[70] Ogio S. et al. Performance of the Fluorescence Detector of the Telescope Array. In *Proceedings of the 32*$^{\text{nd}}$ *ICRC*, Beijing, 2011.

[71] H. Tokuno et al. New air fluorescence detectors employed in the Telescope Array experiment. 2012.

[72] P. Sokolsky, G. B. Thomson, and HiRes Collaboration. Final Results from the High Resolution Fly's Eye (HiRes) Experiment. *PoS*, ICHEP2010:444, 2010.

[73] S. Ozawa et al. Data acquisition system of surface detector array of the telescope array experiment. In *Proceedings of the 30*$^{\text{th}}$ *ICRC*, pages 1109–1112, Merida, 2007.

[74] S. Ozawa et al. The system of DAQ for TA surface array. In *Proceedings of the 29*$^{\text{th}}$ *ICRC*, pages 101–104, Pune, 2005.

[75] T. Nonaka et al. Wide area radio network for the telescope array experiment. In *Proceedings of the 31*$^{\text{st}}$ *ICRC*, Łódź, 2009.

[76] N. Sakurai et al. private communication.

[77] T. Nonaka et al. private communication.

[78] John Allison et al. Geant4 developments and applications. *IEEE Trans. Nucl. Sci.*, 53:270, 2006.

[79] L. Landau. On the energy loss of fast particles by ionization. *J. Phys. (USSR)*, 8:201–205, 1944.

[80] A. Taketa et al. private communication.

[81] A. Taketa et al. The trigger and DAQ system of the surface detector array of the telescope array experiment. In *Proceedings of the 31*$^{\text{st}}$ *ICRC*, Łódź, 2009.

[82] T. Nonaka et al. Performance of ta surface array. In *Proceedings of the 31*$^{\text{st}}$ *ICRC*, Łódź, 2009.

[83] A. Taketa et al. Measurement of the spectrum of ultra-high energy cosmic rays by the telescope array surface array. In *Proceedings of the 31*$^{\mathrm{st}}$ *ICRC*, Łódź, 2009.

[84] B. T. Stokes. private communication.

[85] S. Agostinelli et al. GEANT4: A simulation toolkit. *Nucl. Instrum. Meth.*, A506:250–303, 2003.

[86] D. J. Bird et al. The cosmic ray energy spectrum observed by the Fly's Eye. *Astrophys. J.*, 424:491–502, 1994.

[87] T. Abu-Zayyad et al. Measurement of the cosmic ray energy spectrum and composition from 10**17-eV to 10**18.3-eV using a hybrid fluorescence technique. *Astrophys. J.*, 557:686–699, 2001.

[88] R. U. Abbasi et al. Monocular Measurement of the Spectrum of UHE Cosmic Rays by the FADC Detector of the HiRes Experiment. *Astropart. Phys.*, 23:157–174, 2005.

[89] J. Abraham et al. Observation of the suppression of the flux of cosmic rays above 4×10^{19}eV. *Phys. Rev. Lett.*, 101:061101, 2008.

[90] M. Nagano, D. Heck, K. Shinozaki, N. Inoue, and J. Knapp. Comparison of AGASA data with CORSIKA simulation. *Astropart.Phys.*, 13:277–294, 2000.

[91] D. S. Gorbunov, G. I. Rubtsov, and Sergey V. Troitsky. Air-shower simulations with and without thinning: Artificial fluctuations and their suppression. *Phys. Rev.*, D76:043004, 2007.

[92] B. T. Stokes, D. Ivanov, et al. A simple parallelization scheme for extensive air shower simulations. 2011. Submitted to Astroparticle Physics.

[93] T. Abu-Zayyad et al. CORSIKA Simulation of the Telescope Array Surface Detector. *To be submitted to Astropart. Phys.*, 2012.

[94] A.M. Hillas. Shower simulation: Lessons from MOCCA. *Nucl.Phys.Proc.Suppl.*, 52B:29–42, 1997.

[95] M. Kobal. A thinning method using weight limitation for air-shower simulations. *Astropart.Phys.*, 15:259–273, 2001.

[96] R. U. Abbasi et al. Measurement of the flux of ultra high energy cosmic rays by the stereo technique. *Astropart. Phys.*, 32:53–60, 2009.

[97] C. C. Jui. private communication.

[98] Pierre Billoir. A sampling procedure to regenerate particles in a ground detector from a "thinned" air shower simulation output. *Astropart. Phys.*, 30:270–285, 2008.

[99] M. Teshima et al. PROPERTIES OF 10**9-GeV - 10**10-GeV EXTENSIVE AIR SHOWERS AT CORE DISTANCES BETWEEN 100-m and 3000-m. *J. Phys.*, G12:1097, 1986.

[100] John Linsley and Livio Scarsi. Arrival times of air shower particles at large distances from the axis. *Phys. Rev.*, 128:2384–2392, 1962.

[101] David Newton, J. Knapp, and A. A. Watson. The optimum distance at which to determine the size of a giant air shower. *Astropart. Phys.*, 26:414–419, 2007.

[102] F. James and M. Roos. Minuit: A System for Function Minimization and Analysis of the Parameter Errors and Correlations. *Comput. Phys. Commun.*, 10:343–367, 1975.

[103] Gordon B. Thomson. Results from the Telescope Array Experiment. In *Proceedings of Science (ICHEP 2010)*, page 448, 2010.

[104] T. Abu-Zayyad et al. The Cosmic Ray Spectrum Observed with the Surface Detector of the Telescope Array Experiment Using a New Technique. *To be submitted to Phys. Rev. Lett.*, 2012.

[105] G. Cowan. *Statistical Data Analysis.* Clarendon Press, Oxford, 1998.

[106] Gary J. Feldman and Robert D. Cousins. A Unified Approach to the Classical Statistical Analysis of Small Signals. *Phys. Rev.*, D57:3873–3889, 1998.

[107] D. Ikeda et al. private communication.

[108] T. Abu-Zayyad et al. Energy Spectrum of Ultra-High Energy Cosmic Rays Observed with the Telescope Array Using a Hybrid Technique. *To be submitted to Astropart. Phys.*, 2012.

[109] G. B. Thomson. private communication.

[110] T. Abu-Zayyad, R. Aida, M. Allen, R. Anderson, R. Azuma, et al. The Energy Spectrum of Telescope Array's Middle Drum Detector and the Direct Comparison to the High Resolution Fly's Eye Experiment. 2012.